

Copenhagen University  
Department of Computer Science  
eScience

Doctor of Philosophy Dissertation

# **Image Registration of Lung CT Scans for Monitoring Disease Progression**

by

**Vladlena Gorbunova**

Principal Supervisor: Marleen de Bruijne,  
Co-supervisor: Jon Sporring,  
Co-supervisor: Mads Nielsen.

Copenhagen, 2010

*To my parents Victor and Tatyana*

---

# Contents

---

<b>Contents</b>	<b>i</b>
<b>1 Introduction</b>	<b>3</b>
1.1 Chest Computed Tomography . . . . .	3
1.2 Anatomy of Lungs . . . . .	5
1.3 Chronic Obstructive Pulmonary Disease . . . . .	6
1.4 Monitoring Regional Disease Progression using Lung CT scans . .	7
1.5 Overview of Image Registration Methods . . . . .	10
1.6 Outline of the Thesis . . . . .	14
<b>2 Mass Preserving Image Registration for Lung CT</b>	<b>17</b>
2.1 Introduction . . . . .	17
2.2 Mass preserving image registration . . . . .	19
2.2.1 Image Registration Outline . . . . .	19
2.2.2 Preprocessing . . . . .	20
2.2.3 Transformation . . . . .	20
2.2.4 Mass Preserving Similarity Function . . . . .	20
2.2.5 Optimization . . . . .	21
2.3 Evaluation Strategy for Image Registration Accuracy . . . . .	22
2.4 Experiments and Results . . . . .	23
2.4.1 Parameter Settings . . . . .	23
2.4.2 Experiment 1: Relationship Between Mass, Volume and Density of Lungs . . . . .	24
2.4.3 Experiment 2: Synthetic Data . . . . .	24
2.4.4 Experiment 3: Registration of Lung CT scans . . . . .	26
2.5 Discussion . . . . .	29
2.5.1 Mass Preservation in Lung CT Scans . . . . .	29
2.5.2 Mass Preserving Registration of Lung CT Images . . . . .	30
2.5.3 Distance Between Vessel Centerlines as a Measure for Reg- istration Accuracy . . . . .	31

2.5.4	Comparison to Results in Literature . . . . .	32
2.6	Conclusion . . . . .	33
2.7	Appendix: Gradient of the mass preserving similarity function . . . . .	33
<b>3</b>	<b>Curve- and Surface-based Registration of Lung CT images via Currents</b>	<b>37</b>
3.1	Introduction . . . . .	37
3.2	Registration via Currents . . . . .	38
3.2.1	Representation of curves and surfaces . . . . .	39
3.2.2	Lung structures as currents . . . . .	39
3.2.3	Current-based Image Registration . . . . .	41
3.3	Experiments . . . . .	41
3.3.1	Parameter Settings . . . . .	42
3.3.2	Results . . . . .	42
3.4	Discussion . . . . .	43
3.5	Conclusion . . . . .	45
<b>4</b>	<b>Lung CT Registration Combining Intensity, Curves and Surfaces</b>	<b>47</b>
4.1	Introduction . . . . .	47
4.2	Background and Previous Work . . . . .	49
4.3	Method . . . . .	50
4.3.1	Current-based Registration . . . . .	50
4.3.2	Intensity-based Registration via B-Splines . . . . .	50
4.3.3	Constrained Registration . . . . .	51
4.3.4	Iterative Scheme . . . . .	52
4.4	Experiments . . . . .	53
4.4.1	Data . . . . .	53
4.4.2	Setup of the Current-based Registration . . . . .	54
4.4.3	Setup of the Intensity-based Registration . . . . .	55
4.4.4	Setup of the Combined Registration . . . . .	55
4.5	Results . . . . .	56
4.6	Discussion . . . . .	58
<b>5</b>	<b>Evaluation of Methods for Pulmonary Image Registration 2010: Challenge Results</b>	<b>63</b>
5.1	Introduction . . . . .	63
5.2	Evaluation . . . . .	64
5.2.1	Lungs Boundary Alignment Scores . . . . .	64
5.2.2	Major Fissures Alignment Scores . . . . .	64
5.2.3	Point Correspondence Scores . . . . .	65
5.2.4	Singularity of Deformation Field Scores . . . . .	65
5.3	Results . . . . .	65

5.4	Discussion . . . . .	68
<b>6</b>	<b>Mass Preserving Image Registration For Monitoring Emphysema Progression</b>	<b>73</b>
6.1	Introduction . . . . .	73
6.2	Method . . . . .	75
6.2.1	Mass Preserving Image Registration . . . . .	75
6.2.2	Measure of disease progression . . . . .	75
6.3	Experiments and results . . . . .	75
6.4	Discussion and Conclusions . . . . .	78
<b>7</b>	<b>Early Detection of Emphysema Progression</b>	<b>81</b>
7.1	Introduction . . . . .	81
7.2	Method . . . . .	82
7.2.1	Registration . . . . .	82
7.2.2	Local Image Features . . . . .	83
7.2.3	Dissimilarity Measures . . . . .	83
7.2.4	Disease Progression Measure . . . . .	84
7.3	Experiments . . . . .	84
7.3.1	Data . . . . .	84
7.3.2	Measuring Local Emphysema Progression . . . . .	85
7.4	Results . . . . .	85
7.5	Discussion . . . . .	87
7.6	Appendix . . . . .	89
<b>8</b>	<b>Summary and Discussion</b>	<b>95</b>
8.1	Discussion . . . . .	97
	<b>Bibliography</b>	<b>101</b>



---

# Acknowledgements

---

First of all, I would like to thank my scientific advisor Marleen de Bruijne for constant support, thorough supervision and encouragement along my way through the PhD. You were always sharp minded and kept track of my research and every meeting you brought new ideas and insight into the things I though I am stacked with. Although physically you were 834km away, you were just one message apart. Twice in my life I was very lucky, first when I met my math teacher and second, when you became my supervisor. Thank you for showing me the great example of a truly dedicated researcher!

I would like to thank Jon Sparring for our exciting discussions, you shared with me your deep knowledge and scientific vision on various problems. I am particularly grateful to you for being able to come to your office and discuss problems with you at any time!

My sincere gratitude goes to Mads Nielsen, who shared with me his broad vision on medical image analysis and opened future perspectives. I am particularly thankful to Xavier Pennec, for sharing with me his scientific approach and for his sharp and straightforward advices.

I shall specially thank my reviewers, Francois Lauze, Julia Schnabel and Gary Christensen. You raised important questions, that stimulate further reflection about the research and enables me to look at my work from a side. Your comments definitely make my manuscript scientifically more accurate and correct. And finally, I would like to thank Francois Lauze for his charming French humor.

I am very grateful to my colleagues Pechin Lo and Lauge Sørensen, with whom I shared the office, the COPD project and a great piece of my life. Pechin, you are my C++ hero, you were always ready to chase segmentation faults. I am very thankful to Lauge for showing me the beauty of machine learning techniques. It was a real luxury to work close together with you guys on the same project, thank you for all the fun discussions we had during the past three years. I also had a pleasure to work with Stanley Durrleman and I want to thank him for his kindness and openness. During our scientific discussions, you always shared your deep understanding of the topic with me.

Particularly, I would like to thank Johannes Serup and Sander Jacobs for their dedication to our common projects and the time we spend in discussions, thank you also for giving me an opportunity to be a teacher and a student at the same time.

I would like to thank DIKU professors, Kim Steenstrup, Kenny Erleben, Søren Olsen, and particularly Mads Nielsen, for making our Image Group such a unique, international community where everyone learns lessons far beyond the PhD school program. Special thank to Marco Loog for his optimistic and lively attitude. My thanks goes to the evil PhD office and my colleagues, Søren Hauberg, Aasa Fergasen, Morten Engell-Nørregard, Chen Chen, Konstantin Chernov, Aditya Tatu, Stefan Sommer, Melanie Ganz, Lene Lillemark Larsen, Kersten Petersen and to my former colleagues Alireza Bab-Hadiashar, Lars Schjøjh, David Gustavsson, Rabia Line Granlund, Eva Van Rikxoort and Eugenio Iglesias. You all, made the 3 years of my PhD School much more entertaining.

I am thankful to the whole Asclepios group, where I had the best spring ever. I am particularly thankful to Asclepios girls, Liliame Ramus, Florence Billet, Florence, Aurelie Canaille, with whom I had a great time at work and during the weekends!

Especially I am thankful to the PhD secretary Marianne Henriksen and our group secretaries Camilla Jorgensen and Dina Riis Hansen. You were helping me with the paper work and made my PhD study a bureaucracy-free journey. Finally, thank you for arranging all the summer and winter parties for the group.

My dear friends, Nerijs Rusteika, Vladimir Fedorov, Jana Baltser, Anastasya Gorodinskaya, I would like to thank you for sharing your optimism, for having all the fun together. Thanks for my best friend Irina Olyaeva, for keeping our friendship and for your constant support, wise advises and our exciting discussions. Finally, I am thankful to my boyfriend, Dmitry Khakhulin, for always staying positive, for supporting me in dark and bright times and for showing me my strong sides.

And at last, I am very grateful to my family, my sisters Elena Votintseva and Galina Kobelt for being a great example from my very first days and my parents for believing in me even more than I do myself.



# Chapter 1

---

## Introduction

---

*A journey of a thousand miles must begin with a single step*

— LAO-TZU

### 1.1 Chest Computed Tomography

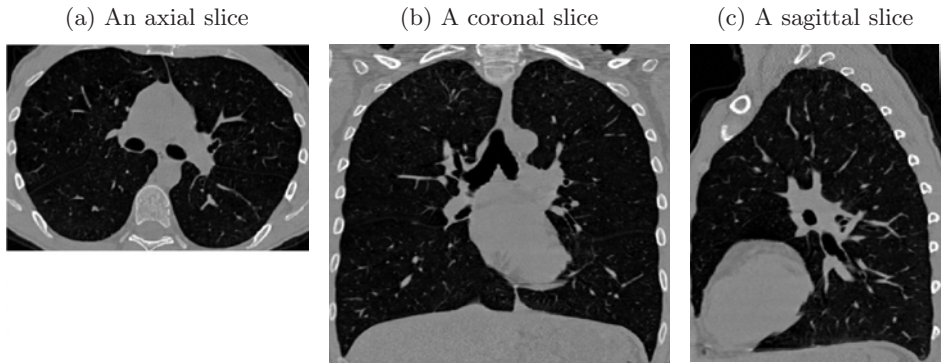
Figure 1.1: Picture of the first medical X-Ray image of a hand. *Reprint from [1].*



Modern computed tomography originated back in November 1895 in the experiments of Wilhelm Conrad Röntgen with an X-ray tube and a fluorescent screen. He discovered, that unknown invisible rays, X-rays, passed through paper and wood and cast a shadow on a fluorescent screen, while it could not travel through metal pieces. When he put his hand into the beam he was surprised to see bones in the casted shadow. Shortly after he photographed his wife, Anna Berthe Röntgen's, hand with the X-Ray beam Figure 1.1 and published a paper on his discovery [1]. The paper made a sensation and spread around the world within few weeks. Already in 1901 he received the Nobel Prize in Physics for his breakthrough discovery.

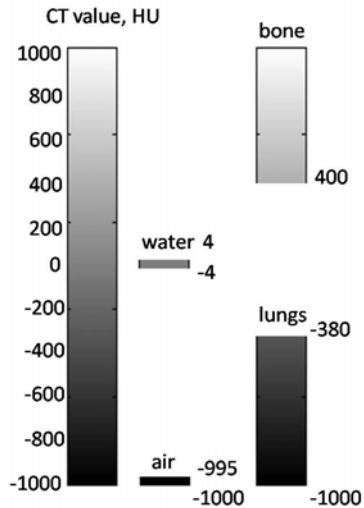
The impact of the discovery on medical science was colossal, it was the first time, when one could see inside the human

Figure 1.3: An example of a modern chest CT scan. The axial, coronal and sagittal slices are extracted from a three dimensional lung CT scan.



body without direct intervention. Shortly after in 1896, Francis Williams started X-Ray examinations of patients with tuberculosis [2]. Owing to the fact that he had access to the state-of-the-art equipment in the Massachusetts Institute of Technology, he was able to carry out thorough research of tuberculosis using the fluoroscopic examination.

Figure 1.2: Hounsfield scale of a CT scan



For a long period, projection radiography was one of the most popular techniques for medical imaging. The idea of imaging just a section of an object was pioneered by Allesandro Vallebona back in 1931 [3]. The term *tomogram* refers to the obtained image of a single section or a slice of an object and the method is called *tomography*. Almost half a century later in 1972 the revolution in medical imaging begun. Godfrey Hounsfield invented computed axial tomography (CAT or simply CT) [4] where a volumetric image of an object was reconstructed from a series of axial tomograms. Since then, computed tomography progressed rapidly from the first CT scanner developed by Godfrey Hounsfield and

applicable only for imaging of small objects to the full body scan in 1976 and the first spiral CT scanner in 1989. Modern CT scanners acquire chest CT scans with high spatial resolution up to 0.5 mm just within several seconds and with the radiation of dozens times smaller than the original CT scanner. An example of a modern chest CT scan is shown in Figure 1.3.

Attenuation coefficient characterizes the decrease of energy of an X-Ray beam

passing through matter. Chest CT scan is a volumetric image where intensity values corresponds to the attenuation coefficient of the matter. A unit of intensity is the Hounsfield Unit (HU). The Hounsfield unit scale is a linear scale of the original attenuation coefficients or the radiodensity. The attenuation coefficient of distilled water under a standard pressure and temperature (0°C, 1 atm) is set to  $\mu_{H_2O} = 0$  HU, and the attenuation coefficient of air is set to  $\mu_{air} = -1000$  HU. A general value  $\mu$  HU corresponds to a material with the attenuation coefficient  $\frac{\mu - \mu_{H_2O}}{\mu_{H_2O} - \mu_{air}} \times 1000$ . The range of Hounsfield Units for human tissues, such as bones, fat, water, blood and muscles is given in Figure 1.2. Typical range of HU for the anatomical structures observed in a lung CT scan is from  $-1000$  HU (corresponds to the attenuation of air) to the  $50$  HU (corresponds to the attenuation of blood). Air in the lung CT appears dark and blood vessels appear bright as one can see in Figure 1.3.

A modern volumetric lung CT scan is a three dimensional image with typically a sub-millimeter in-plane resolution and slice thickness of about 1 mm. However for several clinical applications such as radiation therapy planning a time series of lung CT scans is acquired during a breathing cycle. The obtained four dimensional image is called 4D-CT or dynamic CT lung scans, and along with the regular lung CT scans, images extracted at different phases of 4D-CT lung scans are used in this thesis.

## 1.2 Anatomy of Lungs

When an experienced radiologist looks at a lung CT scan in Figure 1.4, he or she immediately recognizes the anatomical structures presented in the image. As a computer scientist, it took me a while before the sagittal, coronal and axial slices formed into a meaningful three dimensional picture of human lungs. The following anatomical lung structures can be identified in chest CT scans:

- Alveolar lung tissue or parenchyma (typically appears as grey homogeneous matter),
- Pulmonary vasculature (appears as bright stripes or spots),
- Trachea and bronchial tree (appears as pipes with dark inside and bright borders),
- Fissures between the lung lobes (appears as hardly visible thin plate-like structures in light grey color).

Figure 1.4: An example of axial, sagittal and coronal views of a 3D chest CT scan.

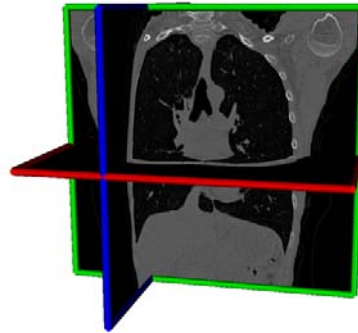


Figure 1.5: A sketch of lung anatomy presenting main anatomical structures within human lungs: lobes, bronchial tree and vessels. © 2006 Terese Winslow U.S. Govt. has certain rights.

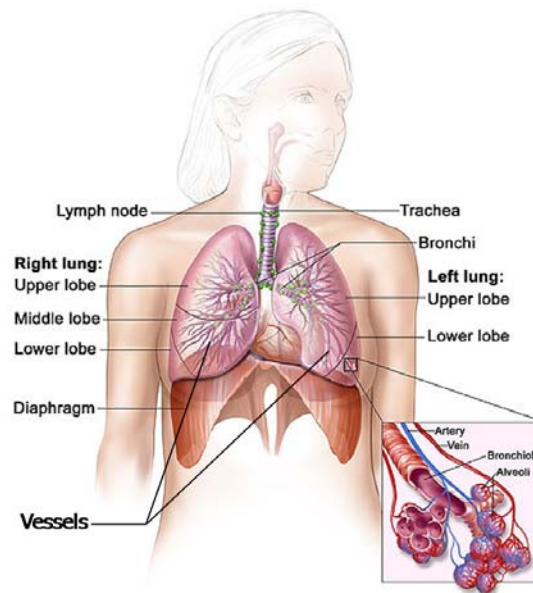


Figure 1.6: Lung anatomy in CT scan. Clearly visible vessels in red color, bronchial tree in blue color. Fissures between the three lobes in right lung are indicated by arrows. A magnified example of a sample within lung tissue is displayed in the bottom right corner.

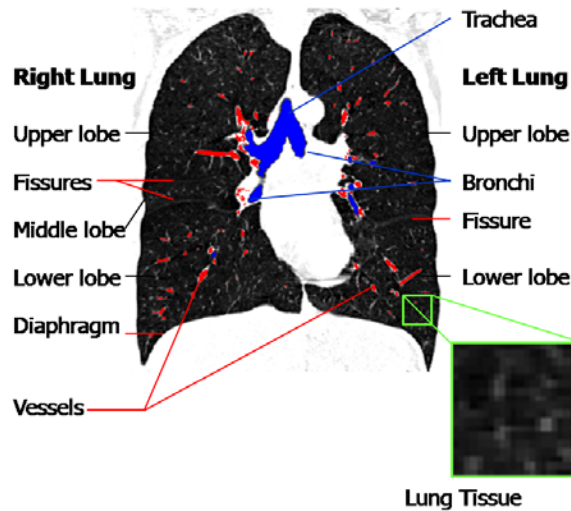


Figure 1.5 shows a drawing of human lung anatomy. The right lung consists of three lobes and the left lung consists of two lobes. Air enters the lungs first through the trachea and then spreads into the bronchial tree. Blood travels through the vessels and spreads in the lungs. Figure 1.6 shows how the corresponding anatomical lung structures appear in a CT scan, for visualization purposes only a coronal CT slice is shown.

### 1.3 Chronic Obstructive Pulmonary Disease

Chronic Obstructive Pulmonary Disease (COPD) encompasses both small airway disease and emphysema. The main topic of the thesis is emphysema, it is

characterized by irreversible destruction of lung parenchyma [5]. Due to the fact that both diseases usually coexist, the common term COPD is used for diagnostics. The most important risk factors of COPD are tobacco smoking and air pollution. COPD cause a shortness of breath, cronical cough, sputum production and may progressively lead to death.

COPD is presently estimated to be the fourth leading cause of death in the world [5]. Accordingly to the World Health Statistics report in 2008, COPD is predicted to be the third leading cause of death worldwide after ischaemic heart disease and cerebrovascular disease in 2030 [6].

Pulmonary function tests (PFT) or lung function tests (LFT) are the primary tools for diagnosis of COPD. Spirometry is the most common test in clinical practice, it measures vital lung characteristics, such as the maximum amount of air exhaled in the first second (FEV1, first expiratory volume in 1 second) and forced total amount of exhaled air (FVC, forced vital capacity). These methods are accepted worldwide for diagnosis of COPD, however there are several drawbacks to the lung function tests. The lung function tests are confirmed to lack sensitivity on the early stages of COPD; can not distinguish type of the abnormality (e.g. emphysema or airway disease) and spatial distribution of disease; and have poor reproducibility [7, 8, 9, 10].

Based on the LFTs, COPD is characterized into four stages; mild, moderate, severe and very severe COPD [5]. Based on the conventional diagnostic tools, disease progression could be determined only in the subjects, who change the COPD stage. A continuous measure of disease progression can be obtained from the lung function tests, but due to lack of sensitivity and reproducibility, the accurate monitoring of COPD is a difficult task in longitudinal studies. Computed Tomography offers a powerful alternative for examination of COPD. CT analysis allows both detailed visual assessment and the whole-lung quantification of emphysema extent via lung densitometry.

Emphysematous regions appear as areas with low-attenuation in CT scans of lungs, suggesting that CT image intensities can be used to quantify the severity of emphysema. Averaged lung density,  $n$ -th percentile density, and relative area with attenuation below, e.g. -910HU (emphysema index, RA-910HU) have all been successfully applied as emphysema measures. For detailed description of the computed tomography methods for lung disease quantification I refer reader to the book written by Webb R.W. et al. [11].

## 1.4 Monitoring Regional Disease Progression using Lung CT scans

In a longitudinal study, the lung densitometry from CT scans provides a continuous measurement of disease progression [12, 13, 14, 15, 16, 17, 18]. In a recent

study on monitoring emphysema progression in Alpha-1 Antitrypsin deficiency subjects [16], the CT densitometry is reported to be significantly more sensitive than the conventional lung function test, the FEV1.

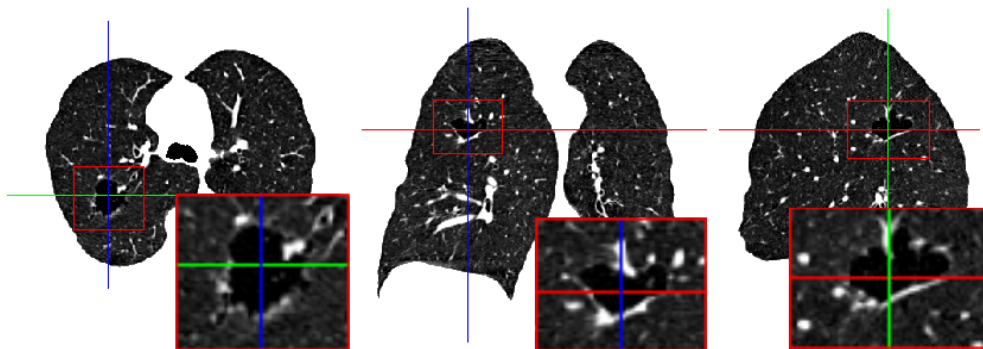
Although computed tomography offers a more promising alternative to spirometry, the CT scores of emphysema are global measures quantifying the disease in the complete lung. Lung partitioning is an approximate solution that allows quantification of emphysema and further monitoring of the disease progression in different regions of the lungs [12]. Another option of monitoring regional emphysema progression is enabled via segmentation methods. The state-of-the art segmentation methods provide anatomical partitioning of lungs into lobes [19, 20, 21], thereby allowing to monitor emphysema progression on a scale of a single lobe. Further segmentation of the lungs into pulmonary segments is extremely challenging task. There is no gold-standard method for segmentation of lung segments, since there are no clear boundaries between the segments, and even manual annotation of pulmonary segments is difficult. Several methods has been proposed for segmenting lung segments [22, 21], but it is still remains a difficult problem without a gold-standard. With use of segmentation methods alone, quantitative analysis of the emphysema will be always limited to the scale of reliably segmented structures. A CT lung scan provides detailed information of the lungs on a scale of 1 mm, thus potentially allowing to perform analysis of lung structures on a much smaller scale than the limiting scale of currently available segmentation methods.

For the detailed analysis of longitudinal changes in lungs, one needs an accurate spatial correspondence between the CT scans. Human observers possess a natural ability of determining corresponding structures in the two dimensional images. However, the task of determining corresponding structures in three dimensions is extremely difficult and time consuming for humans. Furthermore, the human vision system could easily recognize the same object but lacks the sensitivity to the spatial location, e.g., a small translation or distortion to the image may be left unnoticed. Therefore, for an accurate and efficient local analysis of longitudinal CT scans we need an automatic procedure, that will establish a point-to-point correspondence between the CT scans, the **image registration procedure**. Recent studies reported that an image registration procedure could provide comparable accuracy of the spatial correspondence with the human inter-observer variability [23, 24].

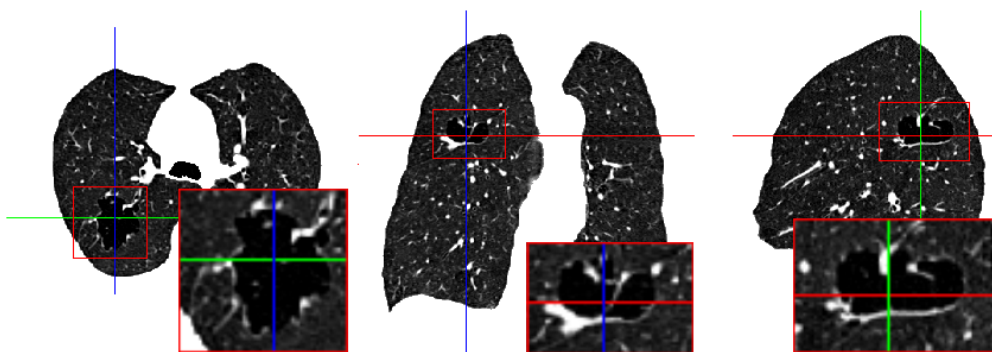
The following example in Figures 1.7-1.8 illustrates how an image registration facilitates monitoring of disease progression on an example of two CT lung scans of the same subject taken with a time interval of approximately two years. The axial, sagittal and coronal slices from the baseline CT scan are showed in the Figure 1.7a and the approximately the same slices from the follow up scan are displayed in Figure 1.7b. In both the baseline and the follow up images a bulla

Figure 1.7: An example of a subject with clearly visible pathology (bullae in the right lung indicated by red box) from the DLCST.

(a) Axial, sagittal and coronal slices from a baseline lung CT scan.



(b) Approximately the same axial, sagittal and coronal slices from the follow up scan.



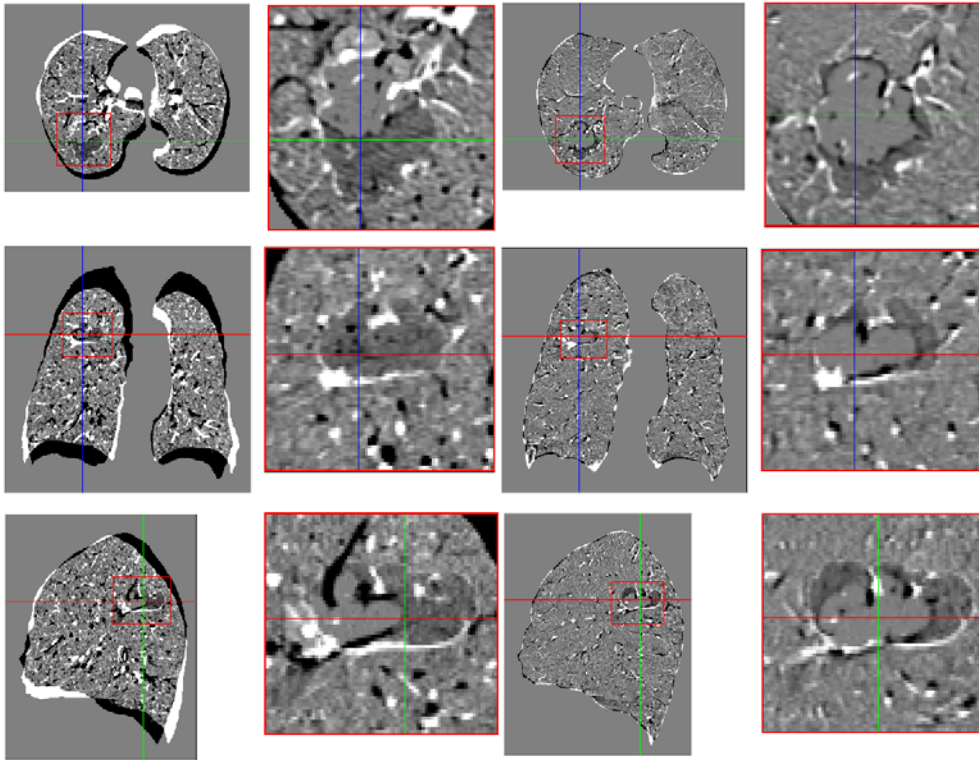
is presented in the right lung. Bulla, or air bubble, is a complication of the emphysema and may be treated by surgical removal or bullectomy.

Consider that subject location was identical in the baseline and the follow up scans, a simple subtraction of the two CT scans should reveal longitudinal changes of the bulla. However direct subtraction of the two images, Figure 1.8a, shows ambiguous and misleading information because of the two main reasons: subject location is not the same in the two CT images; breathing level at the two examinations vary significantly thus resulting in non homogeneous local deformations. After obtaining point-to-point correspondence between the images, the follow up image was deformed to the system of the coordinates of the baseline image and then subtracted from the baseline image. Figure 1.8b shows the final subtraction image and now, once the two images are properly aligned, the subtraction image reveal substantial increase of the bulla size.

Image registration of chest CT scans was successfully used for monitoring nodule growth [25, 26, 27]. Recently image registration has been used to estimate the progression of interstitial lung disease [28]. The benefits of image registration for

Figure 1.8: An example of how an image registration procedure is used for monitoring disease progression in a sequence of longitudinal CT scans.

(a) Direct subtraction of the follow up lung CTscan from the baseline CT scan after the image scan from the baseline CT scan. (b) Subtraction of the deformed follow up CT registration procedure is applied.



monitoring emphysema progression was investigated in this thesis in Chapters 6-7 [29, 30] as well as by other research groups [31].

## 1.5 Overview of Image Registration Methods

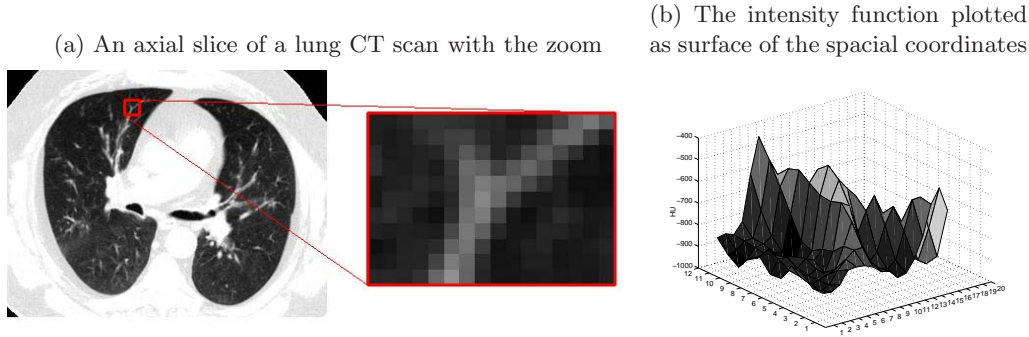
This section presents a brief overview of existing image registration methods, for the details I refer the reader to the concise but mathematical book by J. Modersitzki [32] or to the handbook on medical image analysis by M. Sonka and J.M. Fitzpatrick [33].

### Image Registration Formalism

The starting point of any registration algorithm is a pair of images  $I_f$  (fixed image) and  $I_m$  (moving image). Other definitions of the  $I_f$  and  $I_m$  exist in the literature: image registration methods for lung CT scans define the fixed image



Figure 1.9: Discrete image as a continuous function of space coordinates.



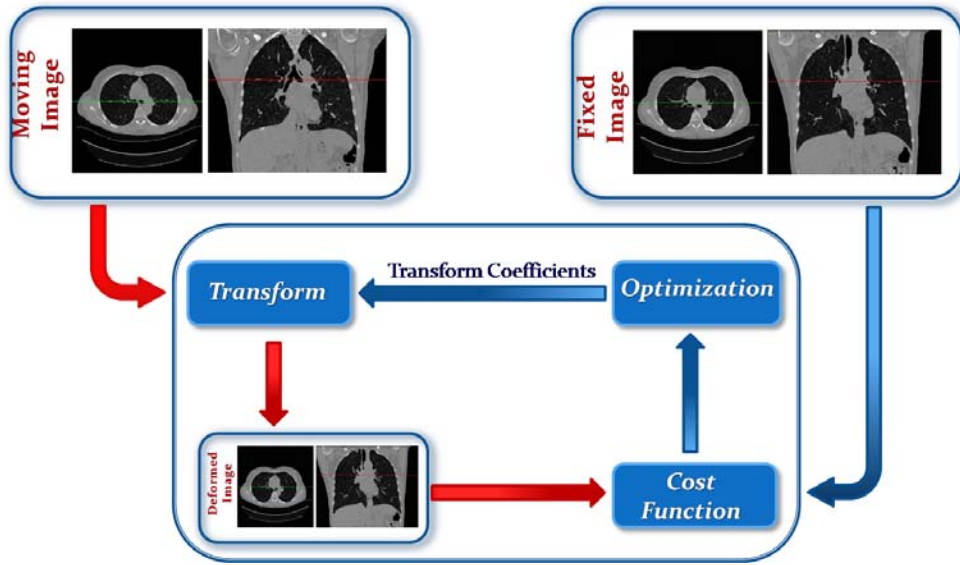
as *reference image* [32, 34, 35, 36, 37, 38]; or *target image* [39, 40, 37, 41, 42]. The moving image also appears as *template image* [32, 40]; *source image* [39, 42]; *floating image* [38]; or *test image* [36]. In this thesis I will use the terms fixed and moving images, because these names reflect the essential functions of the images: while the fixed image remains fixed during the registration procedure the moving image is being deformed.

The task of image registration is to establish point-to-point correspondence between the two images. In case of lung CT scans, images are three dimensional and have discrete nature, the intensities are defined in a finite set of voxels  $I_f(\mathbf{x}) = I_f(x_1^i, x_2^j, x_3^k)$ . Figure 1.9a shows an example of an axial slice of a CT lung scan and a magnified area within lungs region. The zoomed image illustrates discrete nature of the lung CT scan. By means of the interpolation function, images may be defined in a continuous space of the spatial coordinates  $I_f(\mathbf{x})$ . Figure 1.9b displays a surface - the continuous linear approximation of the image intensities. This is the first fundamental part of the registration the **interpolation function**.

The registration procedure establishes point-to-point correspondence between the fixed image region  $\Omega_f \subset \mathcal{R}^3$  and the moving image region  $\Omega_m \subset \mathcal{R}^3$ . The required point-to-point correspondence is defined in natural sense, e.g., an anatomical structure presented in the fixed image in a point  $\mathbf{x} \in \Omega_f$  corresponds to the same anatomical structure presented in the moving image in a corresponding point  $\mathbf{y} \in \Omega_m$ . The formal definition of the correspondence is given via the associated transform function  $T: \Omega_f \rightarrow \Omega_m$ , which takes a point  $\mathbf{x} \in \Omega_f$  and provides a corresponding point  $\mathbf{y} \in \Omega_m$ ,  $T(\mathbf{x}) = \mathbf{y}$ . This is the second important part of the registration - the **transform function**. For the obtained transform function we can compute the resulting deformation vectors of every voxel in the fixed image grid  $\vec{d}(\mathbf{x}) = \mathbf{y} - \mathbf{x}$ . The two terms deformation field and transform function are equally common and usually interchangeable in the image registration literature.

Given a transform function  $T$ , one can evaluate the quality of the obtained point-to-point correspondence by first deforming the moving image  $I_m \circ T =$

Figure 1.10: Diagram displaying the image registration procedure and illustrating the interactions between the image registration components.



$I_m(T(\mathbf{x}))$  and comparing the deformed image with the fixed image  $I_f$  using a (dis)similarity function  $C(I_f(\mathbf{x}), I_m(T(\mathbf{x})))$ . This is the third component of the registration - the **(dis)similarity function**. The (dis)similarity function could be applied directly to the images or to features extracted from the original images. For particular medical applications, an additional constraint on the transform function is needed, the **regularizer**. The (dis)similarity and the regularizer are both combined into a **cost function**, which balances between the (dis)similarity of the images and the regularity of the transform.

Finally, in the task of finding the best possible transform that defines point-to-point correspondence between the two images the minimum of the cost function should be obtained, therefore the following optimization problem should be solved:

$$\operatorname{argmin}_T(C(I_f, I_m \circ T)). \quad (1.1)$$

The final part of the registration procedure is the **optimization method** used to solve problem (1.1). The complete diagram displaying the workflow of image registration is given in Figure 1.10.

### Evaluation of an Image Registration Method

It is always helpful to first check image registration results visually by comparing the fixed image with the deformed moving image. The deformed moving image could be assessed by displaying it side-by-side with the fixed image, or by displaying a checkerboard between the two images, or displaying the difference

between the two images. The disadvantage of the first two methods is that with the side-by-side comparison the human eye could leave a small translation unnoticed and the checkerboard image limits the comparison to the size of the blocks, while in the difference image the mis-registrations are immediately visible.

Generally two classes of quantitative evaluation methods for assessing the quality of registration methods exist: explicit methods that assess the spatial accuracy of alignment in physical units usually millimeters; and implicit methods. The latter methods measure quality of the registration by first deforming the moving image and then comparing it with the fixed image using various (dis)similarity functions, e.g., cross-correlation coefficient, mutual information or sum of squared differences of the two images.

The explicit methods assess the spatial accuracy of the registration by means of, e.g., manually annotated corresponding points, landmarks, in the fixed and the moving images. The Euclidean distance between the landmarks of the moving image and deformed landmarks of the fixed image, the target registration error (TRE), is the quantitative measure of registration accuracy.

Manual annotation of landmarks is both time consuming and difficult for a pair of three dimensional images, therefore automatic or semi-automatic alternatives were developed for detecting corresponding points in the image pairs. The semi-automatic methods ease the procedures of manually landmarking by suggesting possible corresponding points [39, 23]. Betke et al. [25] proposed a fully-automatic system for detecting corresponding landmarks such as trachea, sternum and spine in chest CT scans.

Another fully-automatic alternative to landmarking is assessment of spatial accuracy via presegmented anatomical lung structures. The distance between the corresponding anatomical structures in the fixed and moving images, e.g., lung surfaces, lobe fissures, airway trees or vessel trees, estimates the spatial accuracy of the registration. The Euclidean distance could be computed by first deforming the anatomical structure segmented from the fixed image and then computing the distance to the same structure in the moving image. However, manually annotated landmarks remain the gold standard for the evaluation of image registration accuracy.

### **Examples of Image Registration Methods for Lung CT scans**

The aim of this section is to give a brief overview of modern image registration methods used for lung CT images including the work presented in this thesis as well as work by other authors. Complete overview of general image registration methods could be found in [43].

Depend on the type of information that is being used in the registration algorithm, two classes of image registration methods could be defined: feature-based and intensity-based registration methods. The first class refers to the registration

algorithms, where features are first extracted from the original intensity images and then the point correspondence is established using the obtained features. An examples of a feature-based method is landmark-based registration where the manually annotated landmarks used to align the images [44]. Another example is registration of segmented anatomical lung structures such as vessel trees and lung surfaces [37, 45], Chapter 3[46].

The intensity-based methods directly use the original intensities of the images. These methods are generally more widely used for lung CT images [47, 48, 38, 49, 50, 23, 51, 52, 53, 54, 55, 45, 56], Chapter 2[29]. Also joint registration algorithms where intensity is combined with the features were developed for lung CT scans [57, 58, 59], Chapter 4[60].

Depend on the type of the underlying deformation model, registration methods can be further classified into parametric and non-parametric registration. In parametric methods the transform is parameterized by a number of control parameters. The example of the parametric transform is a B-Spline transform, where the deformation is parameterized by a deformation vectors defined in grid points. Image registration with B-Spline transform was pioneered by D. Rueckert [61] and was first applied to the lung CT scans by D. Mattes [36]. The following registration methods of lung CT scans use the B-Spline transform [47, 48, 38, 49, 50, 23, 29, 51]. In contrast to the parametric methods, in non-parametric methods the deformations are assumed to fulfill a certain physical model, e.g., deformations of fluid [52, 53], proposed by Christensen G. et al. [62] and further developed by M. Bro-Nielsen [63]; elastic material [55, 45], first proposed by Briot C. et al. [64] and further developed by Bajcsy R. et al. [65]; or the optical flow methods [56], first proposed by Horn B.K.P. and Schunk B.G. [66]. While in the first group of methods, the deformation field is free-form and in any point it is interpolated from the deformations defined at the grid positions, in the latter methods the deformation field is obtained from the solution of the associated system of partial differential equations. Overview and implementation details of the latter methods could be found in PhD Thesis by M. Bro-Nielsen [63].

## 1.6 Outline of the Thesis

This thesis contains 8 chapters, including the general introduction in Chapter 1 and general discussion and conclusion in the final Chapter 8. The results of the novel scientific investigations are described in the Chapters 2, 3-7. A brief outline for each of the chapters is given below.

**Chapter 2** describes a novel intensity-based image registration method developed specifically for registering intra-subject lung CT scans. The registration method is based on the widely used free form image registration via B-Splines [61]. The novelty of the developed method is in the proposed model of lung tissue ap-

pearance in CT scans during inspiratory cycle. The lung appearance in CT depends significantly on the amount of air inhaled. First because the lungs are larger in size at the inspiration level and second because the lung tissue saturates additional air and appear darker in CT scans which should not be confused with the emphysema progression and lung tissue destruction. We investigated the validity of the assumption that mass of lungs is preserved during the breathing cycle. The mass preserving assumption was incorporated into the image registration procedure and verified on a large set of lung CT scans with varying quality, ranging from small to large differences in inspiratory level.

**Chapter 3** presents a new feature-based image registration where lung anatomical structures are used to establish a point-to-point correspondence. Three types of registration methods are evaluated: a curve-based registration method where the lung vessel centerlines are used to establish correspondence between the scans, the surface-based registration method where the lung surfaces are used for registration, and the combined method where both curves and surfaces are incorporated into a feature-based registration. The potential advantage of a feature-based registration method over intensity-based method is for diseased subjects, where intensity may change significantly because of the development of the disease. The proposed feature-based registration method does not require any point correspondence, thus it may be applied even using an incomplete and inconsistent segmentations.

**Chapter 4** presents a combination of the intensity- and feature-based registration methods of Chapters 2 and 3. The deformations in the intensity-based method are constrained locally with the deformations obtained from the feature-based method. The weak point of intensity-based registration method is its dependence on the image gradient, thus favoring the good registration of the structures with high gradients, while disregarding misalignment of small unclear structures like the peripheral vessels. On the other hand the feature-based registration assigns the centerlines of small vessels and of large vessels the same value, therefore leading to equally accurate alignment of small and large vessels. The potential benefit of the combined approach is that final alignment is more accurate and realistic.

**Chapter 5** presents results of the challenge "Evaluation of Methods for Pulmonary Image Registration 2010" (EMPIRE10) conducted in conjunction with the Grand Challenges in Medical Image Analysis Workshop in 2010. The mass preserving registration method from Chapter 2 was registered for the competition and final results are included into the thesis.

**Chapter 6** presents an application of the intensity-based image registration method, described in the Chapter 2, for monitoring regional disease progression in longitudinal image studies. Areas with lower intensity in the follow up scan compared with intensities in the deformed baseline image indicate local loss of

lung tissue that is associated with progression of emphysema. To account for differences in lung intensity owing to differences in the inspiration level in the two scans rather than disease progression, we propose to adjust the density of lung tissue with respect to local expansion or compression such that the total weight of the lungs is preserved during deformation. Our method provides a good intensity-based estimation of regional destruction of lung tissue for subjects with a significant difference in inspiration level between CT scans and may result in a more sensitive measure of disease progression than standard quantitative CT measures.

**Chapter 7** presents new methodology and experimental results on monitoring local emphysema progression. We extended the framework from the Chapter 6. Follow up images were first registered to the baseline image and then local image dissimilarities were computed in the corresponding anatomical locations indicating the amount of local changes between the images. Experiments were conducted on patients from the longitudinal study of Alpha-1 Antitrypsin deficiency subjects scanned five times during a period of three years.

The final **Chapter 8** presents general discussion and gives a brief overview of future perspectives.

In this thesis, I used four different lung CT datasets: the pairs of CT scans taken at full inspiration breathhold from the Danish Lung Cancer Screening Study [67] in Chapters 2 and 6; pairs of lung CT scans taken at maximum and minimum breathhold from the study of children with cystic fibrosis (CF) at Sophia Children’s Hospital [68] in Chapter 2; the pairs of end inspiratory and end expiratory phases of 4D-CT lung scans from the publicly available dataset [39] in Chapters 3 and 4; the pairs of CT scans taken at full inspiration breathhold from the EXAcerbations and Computed Tomography scan as Lung End-points (EXACTLE) Trial Study [16] in Chapter 7.

The following open source software packages were used to develop the described methods: ITK [69], CImg [70], elastix [71, 72], iso2mesh [73], exoShape\*.

---

\*To be released at <http://www-sop.inria.fr/asclepios/software.php>

## Chapter 2

---

# Mass Preserving Image Registration for Lung CT

---

*In theory there is no difference between practice and theory, in practice there is.*

— JAN L. A. VAN DE SNEPSCHEUT.

This chapter is partially based on the publications "Weight Preserving Image Registration For Monitoring Emphysema Progression", Gorbunova V., Lo P., Ashraf H., Dirksen A., Nielsen M., de Bruijne M., in proceedings of Medical Image Computing and Computer Assisted Intervention Conference in 2008 and "Mass Preserving Registration for Lung CT", Gorbunova V., Lo P., M. Loeve, H. Tiddens, Nielsen M., J.Sporring, de Bruijne M., in proceedings of Medical Imaging SPIE Conference in 2009.

---

### 2.1 Introduction

Registration of lung CT images is increasingly used in various clinical applications. Three main applications may be distinguished as follows [74] : atlas registration based segmentation of the lungs and structures within the lungs; registration of longitudinal CT image series to monitor disease progression; registration of successive frames in dynamic CT sequences to estimate local ventilation and perfusion.

Examples of the first application can be found in [75, 20]. Sluimer et al. [75] proposed to segment lungs containing dense pathologies by non rigidly registering a set of segmented example images to the image to segment and propagating their labels, while Zhang et al. [20] used atlas registration to initialize fissure detection for lung lobe segmentation. Registration of scans of the same patient taken at different points in time is applied for instance in the monitoring of lung nodules, both to robustly match nodules in sequential CT scans [26, 27] and to visualize nodule changes over time [50]. Recently, registration was also applied to estimate local emphysema progression from longitudinal image data [29, 31]. Registration of successive time frames of 4D-CT lung images is used for motion estimation in lung cancer radiotherapy planning [49, 55, 76] and for estimation of regional lung ventilation [52, 45, 77, 42, 35]. The end expiratory lung CT scans was registered to the end inspiratory scans to facilitate classification of pulmonary diseases [78].

A crucial factor in image registration is the choice of a similarity measure describing the (dis)similarity between the fixed and the deformed images. Commonly used image similarity functions are the sum of squared differences (SSD), mutual information (MI) and normalized cross correlation (NCC) [79].

For intra-subject registration of lung CT images, which is the case we consider in this chapter, SSD is probably the most commonly used similarity measure [48, 27, 52, 53, 80, 81]. Sum of squared differences is optimal when corresponding anatomical points are represented by the same intensity in the images, with additional Gaussian noise. This is a valid assumption because Hounsfield unit (HU) in CT scan represents the density of tissue. Densities of the same tissue is often expected to remain constant in different scans. Previous studies on lung CT scans showed that density of lung tissue depends on regional ventilation and changes during breathing [82, 81]. The basic assumption of SSD similarity function does not hold for lung tissue and as a possible solution we propose to model appearance of lung tissue in CT scan with respect to the regional ventilation using a simple law of mass preservation.

In the mass preserving model, density of the lung tissue is inverse proportional to the local volume. Therefore change in local volume could be computed from the change in the density. First, Simon et al. [83] proposed this model and applied it to estimate regional ventilation from image intensity in 4D-CT lung scans. Vice versa, the change in density of the lung tissue could be computed from the change in the local volume. Under applied local deformations the density of the lung tissue is directly proportional to the determinant of the Jacobian of the transform function, associated with the deformations. Recently, Reinhardt et al. [52] showed strong correlation between regional ventilation obtained from the Xe-CT image and the ventilation computed from the image registration procedure. In the latter case, regional ventilation was computed from the determinant of Jacobian of the obtained transformation between the two images.



Several recent studies have incorporated mass preserving assumption in registration process. Sarrut et al. [81] proposed to modify lung density in a 4D-CT image prior to registration. Tannenbaum et al. [84] proposed a completely new registration method which establishes the optimal mass transportation between the images while the image intensities remain constant. Castillo et al. [56] proposed to incorporate the mass preserving intensity modification model into the optical-flow registration and applied it to the 4D-CT images.

We developed our registration method based on the results from [52] and modeled the lung tissue density using the determinant of the Jacobian of the transform function. We modified the sum of squared differences similarity function to enable mass preservation and continuously simulated the appearance of the lung tissue under the given deformations.

Early versions of this work appeared in [29]. Since then a similar idea has been used by Yin et al. [85, 38], where the mass preserving image registration was applied to breath-hold lung CT images acquired at the maximum inspiration and maximum expiration in the same scanning session. We previously applied mass preserving algorithm to the pairs of maximum inspiration and maximum expiration CT scans taken on the same day [86].

In this chapter, we present the registration framework in more detail, investigate the assumption of mass preservation, and present a quantitative evaluation of registration accuracy of the proposed mass preserving image registration method compared to a standard image registration method on a large number of CT scans of varying quality, ranging from small to large differences in inspiration level.

## 2.2 Mass preserving image registration

This section briefly presents a general deformable image registration framework based on B-Splines which is used in many medical imaging tasks [61, 36], and explains how the proposed mass preserving methodology can be incorporated in this framework.

### 2.2.1 Image Registration Outline

Consider a pair of images  $I_f$  and  $I_m$ , referred to as fixed image and moving image respectively. The task of registration is to find for every point in the fixed image domain  $\Omega_f$  the corresponding point in the moving image domain  $\Omega_m$ . The obtained point correspondences defines a general transform function  $T : \Omega_f \rightarrow \Omega_m$ . Validity of the transform can be assessed by comparing the deformed moving image and the fixed image using a dissimilarity function  $C(I_f, I_m \circ T)$ . An optimal transform should minimize the dissimilarity between the deformed and fixed image, therefore the registration process can be formulated as a minimization

problem, as follows,

$$\operatorname{argmin}_T(C(I_f, I_m \circ T)).$$

### 2.2.2 Preprocessing

To improve registration performance, segmentations of the lung fields are obtained using region growing and morphological smoothing [87]. Previously, several papers showed better performance of registration if the rib cage was erased from the images [23, 48]. To remove the influence of the rib cage, we extract the lung area from the images and set the background to 0HU. Finally, the image intensities are shifted with a value 1000HU so that the new intensities approximate the real densities of the tissues.

### 2.2.3 Transformation

We follow a common approach and use a multi-resolution image registration strategy. First, the images are registered affinely. To provide an accurate initialization of the affine transform, the trachea and main bronchi are first extracted using a modified fast marching algorithm [87]. The center of the affine transform is then set at the carina point in the fixed image and the initial translation is set to the difference between the carina points in moving and fixed images. Secondly, a series of B-Spline transforms, with corresponding Gaussian smoothing at the coarser levels, is applied to the pre-aligned images. The final transform is thus a composition of a global affine transform  $T_A$  and  $N$  levels of B-Spline transforms  $T_{\text{B-Spline}}^i$  with decreasing grid size:

$$T_{\text{final}}(\mathbf{x}) = T_{\text{B-Spline}}^N \circ \dots \circ T_{\text{B-Spline}}^1 \circ T_A(\mathbf{x}), \quad (2.1)$$

where  $\mathbf{x} = (x_1, x_2, x_3)$  is a point in the fixed image domain  $\Omega_f$ .

In this work, we have used small step size along the gradient and multi-level B-Spline grid to ensure that the transform is invertible [88].

### 2.2.4 Mass Preserving Similarity Function

We use the sum of squared differences similarity function as the basis for the mass preserving similarity measure,

$$C(I_f, I_m \circ T) = \frac{1}{|\Omega_f|} \|I_f(\mathbf{x}) - I_m(T(\mathbf{x}))\|_{L_2}^2, \quad (2.2)$$

where  $\mathbf{x}$  is a point in the region  $\Omega_f$  occupied by the fixed image  $I_f$ ,  $\mathbf{y} = T(\mathbf{x})$  is the corresponding point in the region  $\Omega_m$  occupied by the moving image  $I_m$ .

The sum of squared differences is an optimal similarity measure if image intensities are identical or differ with Gaussian noise. This assumption does not

hold in case of lung CT images, where both blood and air enter the lungs during inhalation. We used a hypothesis that majority of incoming blood stays in the larger vessels, and only air is inhaled into the alveoli. Therefore we can presume that mass of parenchyma remains constant and the density of lung tissue is inverse proportional to the amount of air. Under the applied local deformations, the induced change in local volume is defined by the determinant of Jacobian of the associated transform function.

Using the mass preserving assumption, the intensity of the moving image  $I_m$  in a point  $\mathbf{y} \in \Omega_M$  is inverse proportional to the change in local volume  $\frac{1}{\det(J_{T^{-1}})}$  in the point  $\mathbf{y}$ . The modeled intensity can be written  $\hat{I}_m(\mathbf{y}) = [\det(J_{T^{-1}}(\mathbf{y}))]^{-1} I_m(\mathbf{y})$ . Assuming that the transform function  $T$  is invertible, the determinant of Jacobian  $J_{T^{-1}}(\mathbf{y})$  is the inverse of the determinant of Jacobian  $J_T(\mathbf{x})$  and the modeled intensity of the moving image can be written  $\hat{I}_m(\mathbf{y}) = \det(J_T(\mathbf{x})) \cdot I_m(T(\mathbf{x}))$ .

Finally, the mass preserving intensity model can be naturally incorporated in the standard sum of square differences similarity function:

$$C(I_f, I_m \circ T) = \frac{1}{|\Omega_f|} \int_{\Omega_f} [I_f(\mathbf{x}) - \det(J_T(\mathbf{x})) \cdot I_m(T(\mathbf{x}))]^2 d\mathbf{x}. \quad (2.3)$$

### 2.2.5 Optimization

In this chapter we use a stochastic gradient descent method [51] to optimize the similarity function. The closed form expression for the gradient of the proposed mass preserving similarity function of (2.3) is,

$$\begin{aligned} \mathcal{D}_{\mathbf{a}} C = & -\frac{2}{|\Omega_f|} \int_{\Omega_f} [I_f(\mathbf{x}) - \det(J_T(\mathbf{x})) \cdot I_m(T(\mathbf{x}))] \cdot \det(J_T(\mathbf{x})) \cdot \\ & \cdot [\text{vec}(J^{-T}(\mathbf{x}))^T \cdot \mathcal{D}_{\mathbf{a}} \text{vec}(J(\mathbf{x})) \cdot I_m(T(\mathbf{x})) - \mathcal{D}_{\mathbf{y}} I_m(T(\mathbf{x})) \cdot \mathcal{D}_{\mathbf{a}} T(\mathbf{x})] d\mathbf{x}, \end{aligned} \quad (2.4)$$

where  $\mathcal{D}_{\mathbf{a}}$  represents a gradient row vector operator with respect to the transform parameters  $\mathbf{a}$ ,  $\mathcal{D}_{\mathbf{y}}$  represents a spatial gradient vector operator, and  $\text{vec}(\cdot)$  is the vector constructed by concatenating all columns of a matrix. The derivation of (2.4) is given in the Section 2.7.

In case of SSD similarity function, only voxels with non-zero image gradient contribute to the gradient thus resulting in a higher uncertainty of registration in homogeneous regions [47]. On the contrary, for the proposed mass preserving similarity function of (2.4), voxels where the image gradient  $\mathcal{D}_{\mathbf{y}} I_m(\mathbf{y})$  is close to zero also contribute to gradient thus providing additional information in homogeneous regions.

## 2.3 Evaluation Strategy for Image Registration Accuracy

This section describes how the performance of image registration with the regular sum of squared differences similarity function (2.2) is compared to image registration with the proposed mass preserving similarity function (2.3). Evaluation of the registration procedure is done based on the vessel tree centerlines. Additionally, the registration accuracy on a subset of images is assessed using manually annotated landmarks.

The vessels are segmented using the algorithm described in [87]. First, the image is thresholded with fixed intensity  $t_v = -380\text{HU}$ , followed by multi-scale local analysis of the Hessian matrix to remove non-tube like structures. Large vessels in the hylum area are discarded. Finally, centerlines are extracted from the segmented vessel tree using a 3D thinning algorithm [89]. Figure 2.1 shows an example of a segmented vessel tree and the centerlines extracted from it.

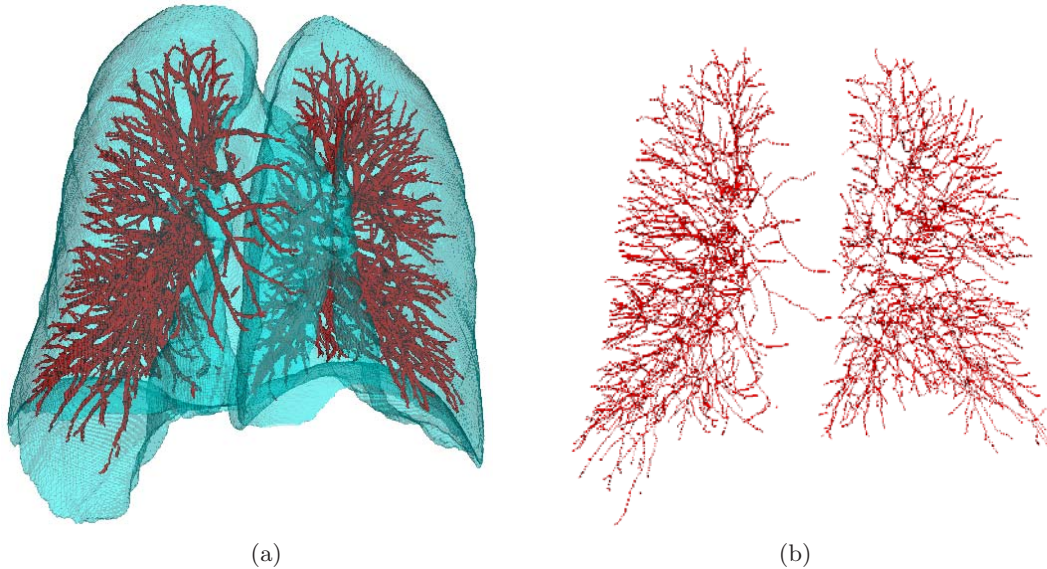


Figure 2.1: Surface rendering of segmented lung fields and vessels (a) and corresponding vessel centerlines (b).

We measure image registration accuracy using the Euclidean distance between vessel tree centerlines. First, we extract vessels from both moving and fixed images. Next, the moving image vessel tree is deformed according to the final transform coefficients. The vessel centerlines are extracted from the segmented vessel trees in fixed and deformed images. Then the Euclidean distance map is computed for the centerlines of the fixed image. Finally, the image registration error is computed as the Euclidean distance map value averaged over all centerline voxels in the deformed moving vessel tree.

## 2.4 Experiments and Results

Section 2.4.1 describes the parameter settings for the two registration methods used in all the conducted experiments. We performed three different experiments to study the proposed mass preserving assumption. First experiment, described in Section 2.4.2, was designed to evaluate the assumption of mass preservation and to investigate the relationship between the volume of lungs and appearance of lung tissue. Section 2.4.3 illustrates the behaviour of the two registration methods, the proposed registration with mass preserving similarity function (MP) and the registration with sum of squared differences similarity function (SSD), on a synthetic example. Finally, the third experiment in Section 2.4.4 was designed to investigate how the difference in lung volume effects the two registration methods.

### 2.4.1 Parameter Settings

We applied three levels of B-Spline transforms,  $N = 3$ , with decreasing grid size. The first two levels were applied to the deformed moving image blurred Gaussian  $\sigma_{1,2} = 1$  voxel and sampled by a factor of two in each direction. The third level was applied to the full resolution image without smoothing. The number of grid cells in each B-Spline level was  $3 \times 3 \times 3$ ,  $6 \times 6 \times 6$  and  $12 \times 12 \times 12$  respectively. Optimal parameters were obtained by minimizing the cost function between the fixed and corresponding moving images.

After each level of transform we computed the current deformation field as the sum of the deformation fields from the previous transforms. The deformation field of the following transform was obtained at the deformed point from the previous transform. The original moving image was then deformed with the obtained deformation field and image intensities were adjusted with respect to the mass preserving model. The Jacobian of the transform was computed using a first order difference scheme with the step equal to the image spacing.

Each of the four transforms in (2.1) was optimized separately using the stochastic gradient descent [51]. The number of voxel samples was chosen proportional to the number of parameters to optimize but not smaller than  $10^4$ , and was set to  $5 \cdot 10^4$  for the finest B-Spline transform and to  $10^4$  for the intermediate B-Spline and Affine transforms. Maximum number of iterations was 1000 for all the transforms. The maximum step length along the normalized gradient direction was set to 0.5 mm.

Vessel trees were segmented using the algorithm as in [87]. The intensity threshold was set to -400HU for the scans in the groups A-C, and -600 for the scans in the group D, and the ratio of Hessian eigenvalues was set to  $m_1 = 0.5, m_2 = 0.5$  for the groups A-C and  $m_1 = 0.75, m_2 = 0.5$ , for the group D. For more details on the parameters of the segmentation algorithm we refer reader to [87].

### 2.4.2 Experiment 1: Relationship Between Mass, Volume and Density of Lungs

We selected 797 subjects which were scanned annually during 3 year period. All subjects did not suffer from Chronic Obstructive Pulmonary Disease (COPD) at the baseline and at the follow up visits according to the GOLD guidelines [5]. We generated all possible pairs of scans of the same subject and randomly selected 1430 image pairs. We computed total lung mass, total lung volume and average lung density for each pair of CT scans. Figure 2.2a shows the scatter plot between relative change in total lung volume and change in total lung mass for the image pairs. Figure 2.2b shows the scatter plot between relative change in total lung volume and change in average density. Spearman correlation between difference in mass and difference in volume was  $r = 0.14$  ( $p < 0.001$ ), and correlation between difference in average density and difference in volume was  $r = -0.91$  ( $p < 0.001$ ).

We investigated the relationship between total lung volume and the shape of histogram of a CT lung scan. We applied a simplified mass preserving model, where the lungs were assumed to expand or contract uniformly and the intensities were globally adjusted as

$$\hat{I}_1(\mathbf{x}) = \frac{V_1}{V_2}(1000 + I_1(\mathbf{x})) - 1000, \quad (2.5)$$

where the  $I_1$  is the first image in a pair, the  $V_1$  and  $V_2$  is the total lung volume of the first and the second images in the pair. The proposed adjusting model may result in missing intensity values, e.g., if the ratio of volumes is equal to  $V_1/V_2 = 2$  the adjusted intensities will be only even numbers. In order to eliminate this artifact, the histograms were smoothed with Gaussian  $\sigma = 5$  HU. Finally, the histograms were normalized to represent probability distribution of the intensities. The difference between the probability distributions of intensity values of lung parenchyma before and after adjustment was assessed using the Kullback-Leibler divergence.

The 1430 pairs of CT scans were split into 15 groups with the relative volume difference varying from  $-37.5\%$  to  $37.5\%$  of the mean lung volume of the two scans. For each group, the average and the standard deviation of the Kullback-Leibler divergence is reported in the Figure 2.2c.

### 2.4.3 Experiment 2: Synthetic Data

The two image registration methods were evaluated on a synthetic image pair constructed to mimic lung tissue expansion under the mass preservation law. Both moving and fixed images represented uniform spheres placed in the center of the images with the background density 0 [g/L] (or intensity  $-1000$ HU). The moving sphere  $S_1$  had radius  $r_1 = 16$  mm and density  $\rho_1 = 200$  [g/L] (or intensity value  $I_1 = -800$ HU) and the fixed sphere  $S_2$  had radius  $r_2 = 20$  mm and density

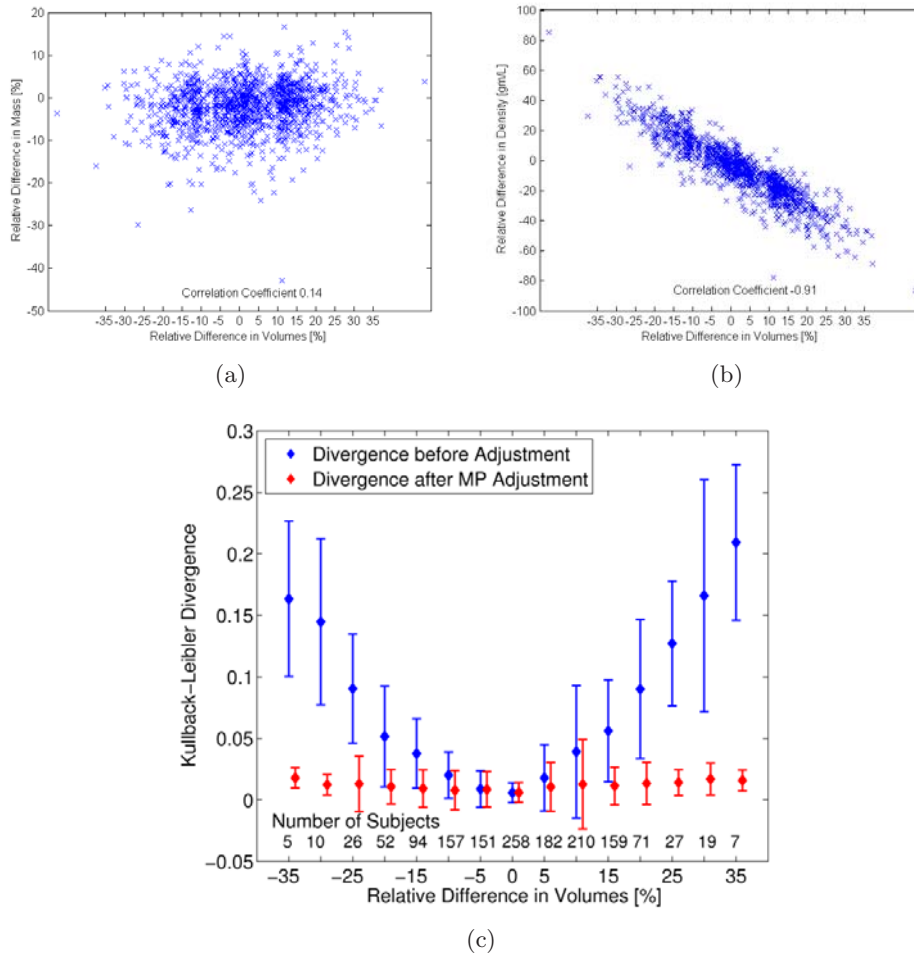


Figure 2.2: Scatter plot (a) displays the correlation between relative change in total lung volume and change in total lung mass. Scatter plot (b) displays the correlation between relative change in total lung volume and change in average lung density. Average Kullback-Leibler divergence between histograms of two CT scans of the same subject before and after the global intensity adjustment is presented in plot (c).

$\rho_2 = 100$  [g/L] (or intensity value  $I_2 = -900$ HU). The mass of the two spheres was approximately equal, 1.93 g and 1.89 g respectively.

The initial affine transform was excluded from the image registration framework described in Section 2.2.3 and only the multi-level B-Spline transforms were used. Optimization parameters were identical for both image registration methods.

Figure 2.3 shows the original fixed (a) and the moving (b) spheres and the resulting difference between the registered and fixed images for the standard registration method (c) and the mass preserving method (d).

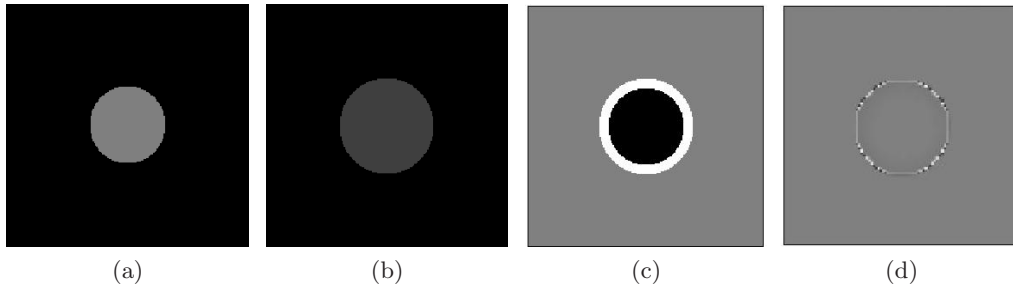


Figure 2.3: The two image registration methods were applied to a synthetic example. The moving image (a) and fixed image (b) consist of spheres with equal mass, but different density. Results (difference image) of the standard image registration method (c) and the proposed mass preserving image registration method (d).

#### 2.4.4 Experiment 3: Registration of Lung CT scans

The third experiment was conducted on a large number of lung CT scans of varying quality, ranging from small to large differences in inspiration level.

- Group A: 44 image pairs of the same subject with the relative difference between total lung volumes for baseline and follow up images  $\Delta TV < 2.5\%$ ;
- Group B: 44 image pairs of the same subject with the relative difference between total lung volumes for baseline and follow up images  $\Delta TV > 9\%$ ;
- Group C: 16 image pairs of inspiratory and expiratory CT scans;
- Group D: 5 image pairs extracted at the end exhale and end inhale phases of the 4D-CT scans from publicly available database [39].

For all four groups, we measured performance of the registration algorithms using the proposed evaluation technique Section 2.3. For the last group, 300 manually selected landmarks for each image pair were available. In this group we additionally compared the two registration methods with the target registration error.

##### Longitudinal Study: Groups A and B

Two groups of low dose CT image pairs were selected from the Danish Lung Cancer Trial Study (DLCST) database [67]. Before the acquisition, subjects were instructed to hold their breath at maximum inspiration. Image pairs have a time interval between baseline and follow up of approximately one year. The in-plane resolution was  $0.78 \times 0.78$  mm and the slice thickness was 1 mm. In group A the average relative difference between the baseline and follow up lung volumes was  $1.23 \pm 0.77\%$  and in group B the average difference was  $14.96 \pm 5.84\%$ .



Evaluation results for the two image registration methods are presented in the Table 2.1. For each patient, we computed the average distance between center-lines registered with the standard method and with the proposed mass preserving method. The overall improvement for each data set is presented in Figure 2.4 with box plots showing median, lower and upper quartile, and skewness of the distribution within each group. The correlation between the relative difference in total lung volume and decrease in error of the mass preserving method in the two selected groups was  $r = 0.44$  ( $p < 0.001$ ).

### **Expiratory and Inspiratory CT Images: Group C**

The group C in our experiment consists of sixteen children with cystic fibrosis (CF) monitored at Sophia Children’s Hospital [68]. All children underwent biannual CT scanning during annual checkup during a clinically stable period. Each CT study consisted of a low-dose CT scan taken at maximum inspiration and an ultra low-dose scan taken at maximum expiration. Before the acquisition, subjects were instructed to exhale or inhale completely and to hold their breath. The in-plane resolution was on average  $0.54 \times 0.54$  mm, the slice thickness is 2.5 mm with a slice overlap of 1.3 mm. The difference in inspiration level between the two images was large and many of the expiration scans show regions of trapped air, indicating local inhomogeneity of deformation. On average, the difference between inspiratory and expiratory volumes was  $48.27 \pm 19.69\%$ . The inspiratory image was set as the fixed image.

Evaluation results are presented in the Table 2.1 and the overall improvement in the group C is presented in the box-plot Figure 2.4. Correlation between the relative difference in total lung volume and improvement of the mass preserving method in the selected group was  $r = 0.77$  ( $p < 0.001$ ). Figure 2.5 shows an example result of the two image registration techniques. The expiratory image was deformed according to the final transformation and subtracted from the inspiratory image. The two images show corresponding slices in the difference images for the mass preserving image registration technique 2.5a-2.5d and for the standard registration 2.5e-2.5h.

### **End Exhale and End Inhale CT Images: Group D**

The last group D consists of 5 pairs of images from a publicly available dataset [39], where each pair consists of images extracted at the end exhale and the end inhale phases of 4D CT images. In-plane resolution of the images varied from  $0.97 \times 0.97$  mm to  $1.16 \times 1.16$  mm and slice thickness was 2.5 mm. The study [39] also provides 300 manually placed landmarks at the end exhale and end inhale phases of the 4D CT images. End exhale image was set as the fixed image.

We validated accuracy of the two image registration algorithms using two independent validation methods. First, we validated using target registration

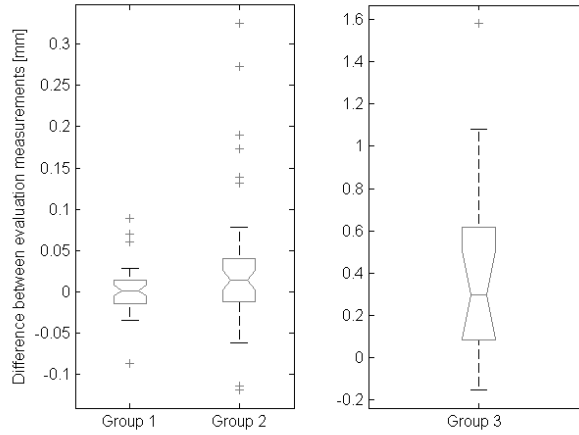


Figure 2.4: Box plots showing the improvement in registration accuracy obtained by the mass preserving image registration method for each of the groups A-C. Each plot shows the median (central mark), lower and upper quartile (edges of the box), skewness of the distribution (notches) and outliers (crosses). From left to right: group A (44 subjects with average  $\Delta TV = 1.23\%$ ), group B (44 subjects with average  $\Delta TV = 14.96\%$ ), group C (16 subjects with  $\Delta TV = 48.27\%$ ).

Table 2.1: Average registration accuracy in each group, assessed using the vessel centerline distance, for the registration with the mass preserving (MP) and the sum of squared differences similarity function (SSD). Number in brackets indicates the number of subjects in the group.

Group	$\Delta TV$ [%]	$\Delta TV$ [L]	Vessel Centerline Distance [mm]		
			SSD	MP	T-test
A (44)	$1.23 \pm 0.77$	$0.07 \pm 0.04$	$1.541 \pm 0.258$	$1.539 \pm 0.251$	$p = 0.604$
B (44)	$14.96 \pm 5.84$	$0.83 \pm 0.29$	$2.017 \pm 0.634$	$1.987 \pm 0.619$	$p = 0.028$
C (16)	$48.27 \pm 19.69$	$1.53 \pm 0.94$	$3.959 \pm 1.370$	$3.535 \pm 1.046$	$p = 0.003$
D (5)	$11.15 \pm 2.86$	$0.37 \pm 0.10$	$2.070 \pm 0.519$	$2.038 \pm 0.522$	$p = 0.160$

error (TRE) between the landmarks. The mean and the standard deviation of TRE for each case is reported in the Table 2.3. The significance of the difference between the two registration methods is assessed using the Student t-test. Second, we evaluated the performance of the registration using the proposed evaluation method from Section 2.3. The mean and the standard deviation of the vessel centerline distance for each case is reported in the Table 2.3.

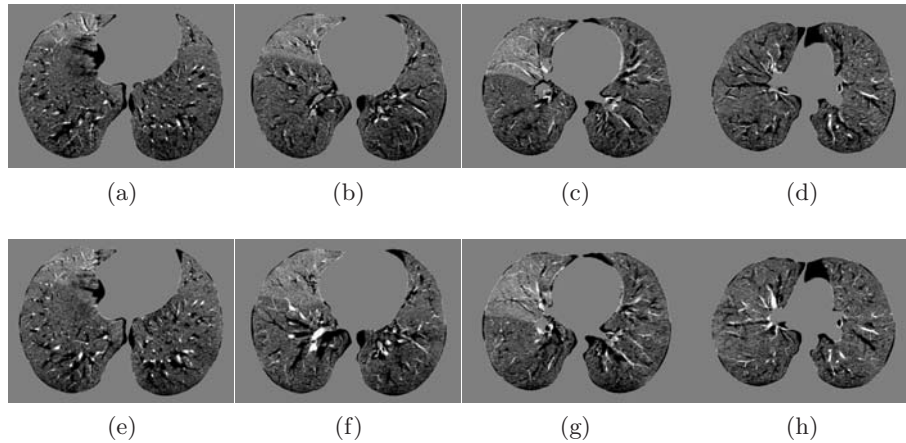


Figure 2.5: An example illustrating the registration performance of mass preserving image registration (a)-(d) and standard registration (e)-(h) for the same randomly selected subject from the group C. The difference images were constructed by first deforming the expiratory image and then subtracting it from the inspiratory image. Every 20th slice, selected in the range of 40 – 100 from the corresponding volumetric difference image is displayed from left to right.

Table 2.2: The two registration methods compared based on the proposed evaluation measure and the target registration error. Results of the validation based on the landmarks are reported before the registration (Initial), after the registration was applied with the mass preserving similarity function (MP), and with the sum of squared differences similarity function (SSD). The statistical comparison of the target registration errors is performed using Student’s test and the p-value is reported in the last column.

N	$\Delta TV\%$	Target Registration Error, [mm]			
		Initial	MP	SSD	p-value
1	9.2	$3.99 \pm 2.75$	$1.15 \pm 0.55$	$1.18 \pm 0.56$	$p = 0.05$
2	8.9	$4.34 \pm 3.90$	$1.26 \pm 0.70$	$1.27 \pm 0.68$	$p = 0.53$
3	11.5	$6.93 \pm 4.09$	$1.79 \pm 1.08$	$1.88 \pm 1.12$	$p < 0.001$
4	15.9	$9.83 \pm 4.86$	$2.01 \pm 1.41$	$2.16 \pm 1.54$	$p < 0.001$
5	10.2	$7.51 \pm 5.53$	$2.31 \pm 1.89$	$2.29 \pm 1.82$	$p = 0.32$
All	11.14	$6.52 \pm 4.83$	$1.70 \pm 1.30$	$1.76 \pm 1.32$	$p < 0.001$

## 2.5 Discussion

### 2.5.1 Mass Preservation in Lung CT Scans

The experiment in Section 2.4.2 showed that the correlation between the change in average lung density and the change in total lung volume was much stronger

Table 2.3: The two registration methods compared based on the proposed evaluation measure and the target registration error. results of the evaluation based on vessel-centerline distance before the registration (Initial), after the registration was applied with the mass preserving similarity function (MP), and with the sum of squared differences similarity function (SSD).

N	Vessel Centerline Distance, [mm]		
	Initial	MP	SSD
1	$3.16 \pm 2.17$	$1.38 \pm 1.61$	$1.43 \pm 1.61$
2	$4.64 \pm 3.67$	$1.82 \pm 2.35$	$1.80 \pm 2.34$
3	$5.15 \pm 3.80$	$2.16 \pm 2.78$	$2.25 \pm 2.79$
4	$4.86 \pm 3.80$	$2.02 \pm 2.26$	$2.05 \pm 2.25$
5	$6.35 \pm 6.42$	$2.81 \pm 3.68$	$2.82 \pm 3.65$
All	$4.83 \pm 1.14$	$2.04 \pm 0.52$	$2.07 \pm 0.52$

( $r = -0.91$ ,  $p < 0.001$ ) than the correlation between the change in lung mass and the change in total lung volume ( $r = 0.14$ ,  $p < 0.001$ ). This indicates a strong dependency of lung tissue appearance in CT image on the level of inspiration. The correlation between the change in mass of the lungs and the change in total lung volume was weak but significant. This may be due to the incomplete vessel extraction, since inspiration leads to increase in perfusion and therefore to increase in partial volume effect near the vessels.

A simplified intensity correction model based on the idea of mass preservation was investigated in the Section 2.4.2. Analysis of image histograms of healthy subjects from Figure 2.2c confirms the fact that the probability density function of image intensities significantly depends on the level of inspiration. Furthermore, the simplified global mass preserving intensity correction significantly reduced the divergence between the histograms as shown in Figure 2.2c.

## 2.5.2 Mass Preserving Registration of Lung CT Images

The experiment in Section 2.4.3, conducted on synthetic data, illustrated the principle advantage of the proposed mass preserving registration, where mass preserving image registration leads to the expected alignment of the two spheres equal in mass and different in volume. The SSD similarity function aligns equal intensities and in the presented synthetic data, intensities of the two spheres were different therefore the geometrically correct solution results in a larger value of the SSD similarity function than the initial positioning of the spheres. The mass preserving similarity function allows to align initially different intensities since the intensity can be changed during the registration procedure thus resulting in the expected alignment of the spheres.

Optimization for the sum of squared differences similarity function as well as the proposed mass preserving similarity function is mainly driven by high gradient structures in the moving image. In areas where the image gradient is close to zero, the optimization of the mass preserving similarity function additionally incorporate the original image intensities. If the difference in intensities is induced by local difference in regional ventilation the optimization of mass preserving similarity function will follow the mass preserving model and align intensities correctly with respect to the measured local volume change.

The advantage of mass preserving image registration is further confirmed in the third experiment, especially in cases where the difference in lung volume is large, which implies differences in regional ventilation and density. The group A of subjects in our experiments had negligible difference in lung tissue appearance between the two CT scans, therefore the difference between the two methods was not significant ( $p=0.6$ ). In the group B, mass preserving image registration resulted in a relatively small, but statistically significant, improvement in registration accuracy compared to the standard image registration method (0.03 mm,  $p=0.03$ ). In group C, the most challenging group, a considerable and significant improvement was measured (0.43 mm,  $p=0.003$ ). The improvement in registration accuracy in groups A-C was strongly correlated with the relative difference in lung volume ( $r = 0.78, p < 0.001$ ). In the last group D, the improvement of mass preserving registration assessed via manually selected landmarks was 0.06 mm, and was statistically significant ( $p \leq 0.001$ ).

A mass preserving model predicts lung tissue appearance in CT scan during respiration based on a simple assumption: preservation of blood in lungs. The density of lung tissue is corrected locally, within the typical size of the B-Spline kernel, according to the change in regional ventilation as measured by the Jacobian of the deformation field. We previously applied this model for monitoring local emphysema progression in patients with COPD [29]. Recently, a similar study was done to monitor emphysema progression in patients with Alpha-1 antitrypsin deficiency patients [31], where a mass preserving intensity correction was applied after normal image registration to compensate for differences in inspiration level between scans. Results suggested more accurate estimates of the disease progression in both these studies.

### 2.5.3 Distance Between Vessel Centerlines as a Measure for Registration Accuracy

Manual extraction of landmarks is both time consuming and prone to inter-expert variability. In this work, instead of relying on manual landmarking we used an automated evaluation method based on vessel tree centerlines to assess the registration accuracy, resulting in a large number of approximately corresponding landmarks throughout the lungs. The drawback of the proposed evaluation

is that vessels that are segmented in only one of the scans may lead to inflation of errors, whereas the absence of point correspondence may lead to underestimation of errors especially in regions where vessel density is high. This could be improved for instance by determining corresponding vessel bifurcation points and parameterizing vessel segments in a consistent manner. However, the effects of over- and under-estimations should be similar for the two different registration methods of the same scan pair provided that both registration methods are reasonably good, and the vessel tree distance is therefore well suited to compare registration accuracy of different methods on the same images.

Comparison with landmark registration error (TRE) showed that the vessel distance measure underestimated the errors before the registration (the average vessel distance measure was 4.83 mm while the average TRE was 6.52 mm) and resulted in overall overestimation of errors after the registration (2.40 mm versus 1.70 mm respectively).

#### 2.5.4 Comparison to Results in Literature

In the conducted experiments, the proposed mass preserving image registration was better than the registration with the sum of squared differences similarity function. The results of the registration with SSD similarity function was comparable with those reported in the literature. Most registration methods were evaluated on 4D-CT scans [39, 38, 48, 37, 80, 56].

Wu et al. [48] used manually extracted landmarks from four end exhale and end inhale image pairs from dynamic CT sequences to evaluate a B-Spline image registration algorithm and reported an average distance between landmarks of 2.78 mm. Pevsner et al. [80] analyzed 6 pairs of end-exhale and end-inhale CT lung scans registered using a fluid registration method with 41 landmarks and reported a discrepancy between registered and observer-determined landmarks of 2.9 mm on average. Vik et al. [37] evaluated a B-Spline image registration algorithm on a set of 10 pairs of end exhale and end inhale phases of 4D-CT lung scans with user-determined landmarks. The average distance between landmarks was  $2.85 \pm 3.06$  mm. Castillo et al. [39] compared optical flow and landmark-based image registration algorithms on 5 pairs of end inhale and end exhale 4D-CT images as in our experiments. The average accuracy was  $6.9 \pm 0.1$  mm for the optical flow image registration and  $2.5 \pm 0.02$  mm for landmark-based registration. Another study by Castillo et al. [56] reported the average TRE of 1.59 mm obtained on the first 3 pairs of the end exhale and end inhale phases of 4D-CT scans. The target registration error of the proposed mass preserving registration method applied on the same 5 pairs end inhale and end exhale phases of 4D-CT scans was 1.70 mm on average.

In our experiments on group C, the pairs of maximum expiration and maximum inspiration CT lung scans, the average vessel distance after the mass pre-

serving registration was relatively large 3.53 mm. This group was the most challenging because of large difference in volume and large amount of pathology such as air-trapping and fibrotic tissue. In this group, the mass preserving registration showed clear improvement compare to the registration method with the SSD similarity function.

Registration of pairs of inspiratory lung CT scans generally produces more accurate results than can be obtained for expiration/inspiration scan pairs or end-exhale/end-inhale images from 4D-CT. Our experiments on longitudinal inspiratory CT lung scans showed comparable accuracy of mass preserving registration 1.76 mm to the results on similar studies reported in the literature [25, 23]. Betke et al. [25] evaluated an image registration algorithm on 10 pairs of repeated inspiratory CT scans using RMS between corresponding surface points and measured error of 3.7 mm. Murphy et al. [23] reported an average error of only 0.7 mm evaluated on a set of semi-automatically extracted landmarks. In the study, selection of landmarks was supported by a thin-plate spline landmark registration algorithm, potentially favoring smooth deformation fields.

## 2.6 Conclusion

In this chapter we investigated the assumption of mass preservation during breathing cycle on the large number of CT scans of varying quality, ranging from small to large difference in inspiration level. We incorporated the mass preserving model into a standard image registration method and evaluated it synthetic data and intra-subject lung CT scans. The results showed that the mass preserving model is a plausible model which describes the change in density in lung CT scans during breathing cycle. Furthermore, the performance of the image registration method with the mass preservation is superior for image pairs with a considerable difference inspiratory level than the image registration method without mass preservation assumption.

## 2.7 Appendix: Gradient of the mass preserving similarity function

In this section we derive the analytical expression for the gradient of the proposed mass preserving similarity function as given in (2.4). Consider the similarity function (as in (2.3)):

$$C(I_f, I_m \circ T) = \frac{1}{|\Omega_f|} \int_{\Omega_f} [I_f(\mathbf{x}) - \det(J_T(\mathbf{x})) \cdot I_m(\mathbf{y})]^2 d\mathbf{x}, \quad (2.6)$$

where  $\int \circ d\mathbf{x}$  is a shortened notation of the volume integral  $\int \int \int \circ dx_1 dx_2 dx_3$ . The transform  $\mathbf{y} = T(\mathbf{x})$  depends on the set of parameters  $\mathbf{a}$ ,  $T(\mathbf{a}, \mathbf{x})$ . For simplicity,

we shorten the notation of the Jacobian determinant  $|J| = \det(J_T(\mathbf{x}))$ , the fixed image value in a point  $\mathbf{x}$  as  $I_f = I_f(\mathbf{x})$ , the transformed point  $\mathbf{y} = T(\mathbf{x}, \mathbf{a})$ , the moving image value in the transform point  $I_m = I_m(\mathbf{y})$  and label the observed difference in intensities at a point  $\mathbf{x}$  with respect to the transform parameters  $\mathbf{a}$  as a function  $G(\mathbf{a}, \mathbf{x})$ :

$$\begin{aligned} C(I_f, I_m \circ T(\mathbf{a})) &= \int_{\Omega_f} G(\mathbf{a}, \mathbf{x})^2 d\mathbf{x}, \\ G(\mathbf{a}, \mathbf{x}) &= I_f(\mathbf{x}) - \det(J_T(\mathbf{x})) \cdot I_m(\mathbf{y}(\mathbf{a}, \mathbf{x})) = I_f - |J|I_m. \end{aligned}$$

Using differential algebra we write the full differential of the similarity function,

$$\begin{aligned} dC(\mathbf{a}) &= \int_{\Omega_f} 2GdG d\mathbf{x}, \\ dG(\mathbf{a}, \mathbf{x}) &= \mathcal{D}_{\mathbf{x}}I_f d\mathbf{x} - |J|\text{tr}(J^{-1}dJ)I_m - |J|\mathcal{D}_{\mathbf{y}}I_m d\mathbf{y} \\ &= \mathcal{D}_{\mathbf{x}}I_f d\mathbf{x} - |J| \left( \underbrace{\text{tr}(J^{-1}dJ)}_{(*)} I_m + \mathcal{D}_{\mathbf{y}}I_m d\mathbf{y} \right), \end{aligned} \quad (2.7)$$

where the notation  $dC$  stands for the full differential of the function  $C$ . Using the definition of the vec operator, we can simplify the term (\*):

$$\text{tr}(J^{-1}dJ) = \text{vec}(J^{-T})^T \text{vec}(dJ). \quad (2.8)$$

Further the term  $\text{vec}(dJ)$  can be expanded,

$$\text{vec}(dJ) = d(\text{vec}(J)) = \mathcal{D}_{\mathbf{a}}\text{vec}(J) d\mathbf{a} + \mathcal{D}_{\mathbf{x}}\text{vec}(J) d\mathbf{x}, \quad (2.9)$$

and by substituting (2.9) into (2.8) we get

$$\text{tr}(J^{-1}dJ) = \text{vec}(J^{-T})^T \cdot \mathcal{D}_{\mathbf{a}}\text{vec}(J) d\mathbf{a} + \text{vec}(J^{-T})^T \cdot \mathcal{D}_{\mathbf{x}}\text{vec}(J) d\mathbf{x}, \quad (2.10)$$

where  $\mathcal{D}_{\mathbf{a}}$  is the gradient in the direction of the transform parameters  $\mathbf{a}$  and  $\mathcal{D}_{\mathbf{x}}$  is a spatial gradient. The differential  $d\mathbf{y}$  is defined as

$$d\mathbf{y} = \mathcal{D}_{\mathbf{a}}\mathbf{y} d\mathbf{a} + \mathcal{D}_{\mathbf{x}}\mathbf{y} d\mathbf{x} = \mathcal{D}_{\mathbf{a}}\mathbf{y} d\mathbf{a} + J d\mathbf{x}. \quad (2.11)$$

By substituting (2.10) and (2.11) into (2.7) we get the full differential of  $C(I_f, I_m \circ T)$ :

$$\begin{aligned} dG(\mathbf{a}, \mathbf{x}) &= \mathcal{D}_{\mathbf{x}}I_f d\mathbf{x} - |J| \cdot \mathcal{D}_{\mathbf{y}}I_m \cdot J d\mathbf{x} - |J| \cdot I_m \cdot \text{vec}(J^{-T})^T \cdot \mathcal{D}_{\mathbf{x}}\text{vec}(J) d\mathbf{x} \\ &\quad - |J| \cdot \text{vec}(J^{-T})^T \cdot \mathcal{D}_{\mathbf{a}}\text{vec}(J) d\mathbf{a} \cdot I_m - |J| \cdot \mathcal{D}_{\mathbf{y}}I_m \cdot \mathcal{D}_{\mathbf{a}}\mathbf{y} d\mathbf{a}. \end{aligned}$$

Finally, since  $\mathbf{x}$  is fixed, we find that the partial derivative of  $C(I_f, I_m \circ T)$  w.r.t. the transform parameters  $\mathbf{a}$  is

$$\mathcal{D}_{\mathbf{a}}C = -\frac{1}{\Omega_f} \int_{\Omega_f} 2(I_f - |J| \cdot I_m)|J| (\text{vec}(J^{-T})^T \cdot \mathcal{D}_{\mathbf{a}}\text{vec}(J) \cdot I_m - \mathcal{D}_{\mathbf{y}}I_m \cdot \mathcal{D}_{\mathbf{a}}\mathbf{y}) d\mathbf{x},$$



where  $\mathcal{D}_{\mathbf{y}}I_m = (\partial_{y_1}I_m; \partial_{y_2}I_m; \partial_{y_3}I_m)$  is the spatial row-vector gradient and  $\mathcal{D}_{\mathbf{a}}$  is the row-vector gradients the transform  $T(\mathbf{x}) = \mathbf{y} = (y_1; y_2; y_3)$  in the direction of the transform parameters  $\mathbf{a}$ ,

$$\mathcal{D}_{\mathbf{a}}\mathbf{y} = \begin{pmatrix} \partial_{a_1}y_1 & \dots & \partial_{a_n}y_1 \\ \partial_{a_1}y_2 & \dots & \partial_{a_n}y_2 \\ \partial_{a_1}y_3 & \dots & \partial_{a_n}y_3 \end{pmatrix}. \quad (2.12)$$



## Chapter 3

---

# Curve- and Surface-based Registration of Lung CT images via Currents

---

This chapter is based on the publication "Curve- and Surface-based Registration of Lung CT images via Currents", Gorbunova V., Durrleman S., Pechin L., Pennec X., de Bruijne M., in proceedings of The Second International Workshop on Pulmonary Image Analysis in conjunction with the Medical Image Computing and Computer Assisted Intervention Conference 2009.

---

### 3.1 Introduction

Registration of chest CT scans is an important topic within pulmonary image analysis. The general task of registration is to establish a point-to-point correspondence between two images. Registration of lung CT images can be used in various clinical applications, such as lung cancer radiotherapy planning and quantitative analysis of disease progression.

Image registration methods can be separated into two general groups: intensity-based and feature-based methods. Intensity-based methods integrate spatial information over the entire image domain, whereas feature-based methods require a representation of the image data in terms of distinctive geometrical structures. Feature-based methods offer more robust registration when image intensity is changed, for instance owing to pathology, image artifacts or differences in scan protocol. Generally, segmentation of geometrical structures in lungs is less sensi-

tive to intensity changes, since a segmentation method incorporates geometrical regularity constraints or prior anatomical knowledge. Moreover, segmentation of distinctive lung structures may be either corrected manually or delineated by a professional.

The most distinctive anatomical structures in lung CT images are vessels, airways, lobe fissures and lung surfaces. Deformation of lungs surfaces and lobe fissures provide an insight into the global motion of the lungs, while deformations of vessels and airway tree characterize small-scale deformations inside the lungs.

A feature-based registration relies on various geometrical structures, e.g., points, curves or surfaces. Thin-plate spline image registration [44, 90, 91] is the standard method for matching points under the assumption that deformations are small. For large deformations, a diffeomorphic point matching approach was developed by Joshi and Miller [92] and was later adapted for surface matching [93]. Current-based diffeomorphic method for surface matching under the large deformations, pioneered by Glaunès et. al. [93], was further developed and adapted for curve matching problem [94, 95]. Within a framework of currents, no point correspondence between structures is required.

Several surface-based registration methods were previously developed for lung CT images [37, 76, 25]. The outer surface of the lungs together with the outer surface of vessels were used in an algorithm similar to iterative closest point methods in [37]. Lung surfaces were used to register CT lung images [25] and to constrain intensity-based registration with a deformation field obtained from surface matching procedure [76]. The two main advantages of the feature-based registration of lung CT images via currents are: no point correspondence is required and unified representation of curves and surfaces. The low dimensional geometrical features, such as curves and surfaces contain much fewer points compared to dense intensity images, thus feature-based registration can be more efficient. Moreover, in the framework of currents, dimensionality of image features may be reduced even more without decreasing registration accuracy [96].

In this chapter we apply the current-based registration method, pioneered by Glaunès et. al. [93] and further propagated by Durrleman [95, 97], to three feature sets: vessel centerlines, lung surface and combined set of centerlines and surface. We evaluated the registration methods on a set of 5 pairs of end exhalation and end inhalation phases of 4D-CT images with manually annotated landmarks.

## 3.2 Registration via Currents

This section describes how lung CT scans can be registered using the framework of currents, developed in [93, 98]. Firstly, Section 3.2.1 explains how curves and surfaces are represented via currents. Secondly, Section 3.2.2 describes how

anatomical lung structures, e.g., vessel tree and lung surfaces, were adapted to the framework of currents. Finally, Section 3.2.3 provides details of current-based registration of curves and surfaces.

### 3.2.1 Representation of curves and surfaces

In the framework of currents [93, 94, 97], geometrical shapes such as curves and surfaces are represented with a set of vectors. A current is encoded with a finite set of vectors attached to the specified positions. A curve  $C(x)$  can be defined with its tangent vector  $\tau(x)$  at each position  $x$ . In a discrete setting, curve is considered as a set of piece-wise linear segments, where each segment is represented by its center point, tangential direction, and segment length. Similarly, a surface  $S(x)$ , with a constructed mesh, is defined with the normal direction  $n(x)$ , face center  $x$  and area. Both surfaces and curves are thus encoded into currents as a set of vectors. Geometrical shape in the framework of currents is defined in a weak form, as the action of the shape on a test vector field  $w$  from a space of possible vector fields  $W$ . The current of a curve  $C(\omega)$  is defined by the path integral along the curve through the test vector field  $w$ ,

$$C(\omega) = \int_C w(x)\tau(x)dx. \quad (3.1)$$

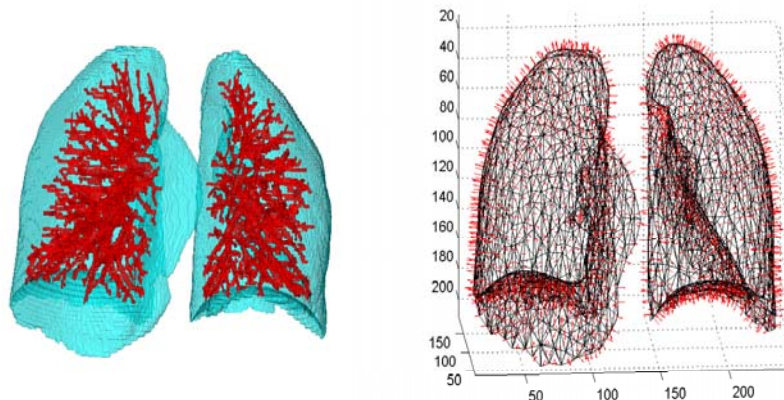
And the current of a surface  $S(\omega)$  is defined by the flux of the vector field  $w$  through the surface,

$$S(\omega) = \int_S w(x)n(x)dx. \quad (3.2)$$

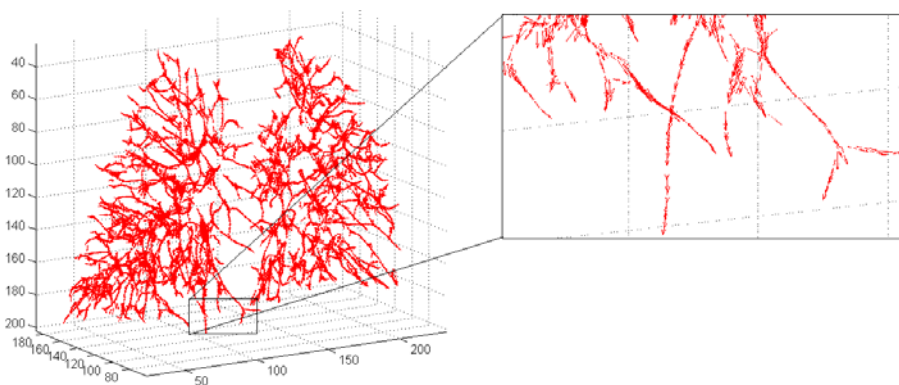
The space  $W$  of test vector fields is a space of square integrable vector fields convolved with a Gaussian kernel with standard deviation  $\lambda_W$  [97, 94]. The norm of the current,  $\mu(C)$ , is defined in the dual space  $W^*$ , as the maximum action of the current among all possible test vector fields  $\|\mu(C)\|_{W^*} = \sup_{\|w\|_W \leq 1} C(w)$ . The scale  $\lambda_W$  controls matching accuracy, for example, curves or structures located within the scale size are considered similar, and their shapes should be matched with accuracy proportional to the scale size.

### 3.2.2 Lung structures as currents

In this chapter we used distinctive anatomical lung structures such as vessels and lung surfaces as features for registration. Figure 3.1a shows an example of segmented lung structures. The lung fields and vessels are segmented with the algorithm described in [87]. A sparse triangulation of the lung surfaces was computed via the marching cube algorithm [73]. For each face, the corresponding normals were computed and oriented to point outwards of the surface. Figure 3.1b shows an example of the constructed current for a lung surface.



(a) Example of segmented lung surface and lung vessel tree (b) Current corresponding to a lung surface.



(c) Current corresponding to a vessel tree centerlines.

Figure 3.1: Example of segmented lungs surface and vessel tree (a); triangulation of the lungs surface (black mesh) with the corresponding current (red vectors) (b); current corresponding to the vessel tree centerlines (red vectors) with a zoom-in (c).

Vessel tree was segmented as follows: a lung image was thresholded with a fixed intensity value  $t_v = -600HU$ , then a local analysis of Hessian matrix was performed in order to remove non-tube like structures. Large vessels segmented near the hilum area were omitted from the vessel tree segmentation. For more details on vessels segmentation algorithm we refer the reader to [87]. Centerlines were extracted from the segmented vessel tree using a 3D thinning algorithm [89].

The tangential direction of a centerline was computed via local principal component analysis. For each centerline point we extracted neighboring centerline points, applied PCA to the point cloud, and assigned the first principal component to the tangential direction at the centerline. For centerlines sufficiently far

from vessel bifurcation and neighboring vessel, the principal direction points to a tangential direction of the centerline. For centerlines close to the bifurcation the principal direction points between the two splitting vessel centerlines. This is consistent with the framework of currents, where the action of each vessel direction results in a joint action at the bifurcation point. The orientation for the positive direction was set to point outwards from the center of the image. Figure 3.1c shows an example of the constructed current for a segmented vessel tree and a zoom-in into a bottom part of the image.

### 3.2.3 Current-based Image Registration

In this chapter, we combine the previous work on matching curves [94] and surfaces [93] via currents. The similarity measure between two curves  $C_f$ ,  $C_m$  or two surfaces  $S_f$ ,  $S_m$  is defined as the squared norm of the difference in  $\mu$  for corresponding currents with respect to the test vector field  $w \in W$ :

$$E(C_f; C_m) = \|\mu(C_f) - \mu(\phi \cdot C_m)\|_{W^*}^2, \quad (3.3)$$

for fixed and moving curves  $C_f$  and  $C_m$  respectively. And

$$E(S_f; S_m) = \|\mu(S_f) - \mu(\phi \cdot S_m)\|_{W^*}^2, \quad (3.4)$$

for fixed and moving surfaces  $S_f$  and  $S_m$  respectively, where  $\phi$  is a diffeomorphic transform function. Combining two similarity terms for curves (3.3), surfaces (3.4) and a regularisation term with trade-off coefficients  $\gamma_C, \gamma_S, \gamma_\phi$  in a final cost function gives:

$$\begin{aligned} E(C_f, S_f; C_m, S_m) &= \gamma_C \|\mu(C_f) - \mu(\phi \cdot C_m)\|_{W^*}^2 + \gamma_S \|\mu(S_f) - \mu(\phi \cdot S_m)\|_{W^*}^2 \\ &+ \gamma_\phi \text{Reg}(\phi). \end{aligned} \quad (3.5)$$

Diffeomorphic transformation  $\phi$  of curves and surfaces was modeled in the framework of large deformation diffeomorphic matching [92, 94], where deformation of each feature is defined by a velocity vector field  $v_t = \phi'_t$ . The smooth velocity field  $v_t$  is described via Gaussian kernel with standard deviation  $\lambda_V$ , where  $\lambda_V$  determines the typical scale of the deformations [97, 94]. To guarantee smoothness of the final diffeomorphism, we defined the regularisation term as in [97],

$$\text{Reg}(\phi) = \int_0^1 \|v_t\|_V^2 dt. \quad (3.6)$$

## 3.3 Experiments

In order to quantify the accuracy of the proposed registration method with a ground truth, we used images from a publicly available dataset [39]. For each

image pair, 300 manually placed corresponding landmarks were provided [39]. Five pairs of images, where each pair consists of images extracted at end exhale and end inhale phases of 4D CT image, were used in our experiments. In-plane resolution of the images varied from  $0.97 \times 0.97$  mm to  $1.16 \times 1.16$  mm and slice thickness was 2.5 mm.

### 3.3.1 Parameter Settings

Vessel tree were segmented using the algorithm as in [87] with the intensity threshold  $-600$  HU, ratio of Hessian eigenvalues was set to  $m_1 = 0.75$ ,  $m_2 = 0.5$ . For every centerline point we extracted a neighboring centerline points from the cube neighborhood of  $7 \times 7 \times 7$  voxels size and computed the principal direction of the centerlines. All the direction vectors were normalized to 1. Figure 3.1c shows an example of the extracted currents for vessel centerlines with a zoom-in to a lower part of the lungs. A regular surface triangulation was constructed with a marching cube algorithm with further simplification of the mesh [73]. Normal directions to each of the face were normalized to 1.

In our experiments, end inhale phase of 4D-CT image was registered to end exhale phase. The following internal parameters of image registration were selected manually. The accuracy of feature alignment  $\lambda_W$  was set to 5 mm for curves and 10 mm for surface features. The parameter  $\lambda_V$  for spatial variability of deformation velocity field was set to 25 mm for both types of features. The weight coefficients in the cost function (3.5) were set to  $\gamma_C = 1$  for the curve matching term,  $\gamma_S = 0.01$  for the surface matching term and  $\gamma_\phi = 10^{-4}$  for the regularizer. The cost function was minimized with a standard gradient descent approach.

### 3.3.2 Results

We evaluated four registration methods, as follows: combined curve- and surface-based registration with cost function (3.5); curve-based registration with cost function (3.3); surface-based registration with cost function (3.4); and a free-form B-Spline intensity-based method as in [29]. We compared registration accuracy of the four methods based on the alignment of 300 landmarks distributed uniformly in lung area, Figure ?? shows an example of the spatial distribution of landmarks within the lungs.

The overall accuracy of the image registration methods was defined as the mean Euclidean distance between landmarks, target registration error (TRE), in millimeters. The mean and the standard deviation of TRE for the four methods is reported in Table ?. We performed Wilcoxon rank-sum test on TRE distribution to compare the combined curve- and surface-based registration with the curve-based and surface-based methods individually. Results are reported in the



Table 3.1: Registration error at the landmark positions in [mm] for the four registration methods. The mean (m) and the standard deviation (sd) are reported. Statistical comparison of combined curve- and surface-based registration method was performed against the surface-based and curve-based methods. The notations of statistical significance level are as follows: \* corresponds to  $p \leq 0.05$  and  $^{ns}$  to  $p > 0.05$ . The most right column indicates percentage of landmarks, where the combined curve- and surface-based registration outperforms the intensity-based registration.

Image Registration Accuracy in mm [m $\pm$ sd]						
N	Before	Combined	Surface	Curve	Intensity	%
1	3.89 $\pm$ 2.78	1.47 $\pm$ 0.72	2.45 $\pm$ 1.56*	2.24 $\pm$ 1.41*	1.23 $\pm$ 0.61	37.7
2	4.34 $\pm$ 3.90	2.19 $\pm$ 1.98	3.63 $\pm$ 2.94*	2.32 $\pm$ 2.06 <sup>ns</sup>	1.26 $\pm$ 0.67	39.0
3	6.94 $\pm$ 4.05	3.30 $\pm$ 3.05	5.31 $\pm$ 3.26*	3.03 $\pm$ 2.79*	1.86 $\pm$ 1.11	25.0
4	9.83 $\pm$ 4.86	3.34 $\pm$ 2.67	5.98 $\pm$ 3.74*	5.28 $\pm$ 4.52*	2.15 $\pm$ 1.48	36.0
5	7.48 $\pm$ 5.51	3.83 $\pm$ 3.54	5.80 $\pm$ 4.37*	4.40 $\pm$ 4.42*	2.32 $\pm$ 1.82	40.0
All 5 cases						
	6.50 $\pm$ 4.83	2.83 $\pm$ 2.72	4.63 $\pm$ 3.58*	3.45 $\pm$ 3.48*	1.76 $\pm$ 1.31	35.5
Mdn	5.13	1.85	3.53	2.37	1.44	

Table ???. Box-plots in Figure ?? show the overall accuracy of the four image registration methods on a complete set of landmarks over all five cases.

Correlation between TRE for the intensity-based and combined curve- and surface-based registration was  $\rho = 0.5$ , varying from 0.17 – 0.59 for the five cases. Overall, for 35.5% cases of landmarks the combined curve- and surface-based registration method performed better than intensity-based method.

Figure 3.2: Target registration errors (TRE) is shown in (a), as follows, before registration was applied (Initial), after surface-based (Surface), after curve-based (Curve), after combined curve- and surface-based (Combined) and after intensity-based registration (Intensity). Example (b) shows the spatial distribution of landmarks in the lungs. The landmarks, better aligned with the combined feature-based method are shown in red and with the intensity-based method in blue.

### 3.4 Discussion

Figure ?? shows that the curve-based method alone provides good registration accuracy for the majority of landmarks. However, there are many outliers present

with errors of up to 2.5 cm. Within the framework of currents, points located further than the typical scale of deformations  $\lambda_V$  are not affected by deformations of the features, which might cause landmarks distant to the vessel centerlines to be misaligned. Surface-based registration result in a slight overall improvement in TRE compare to the initial configuration. In contrast, incorporating both surfaces and curves into feature-based registration results in more accurate registration (1.85 mm) compared to both curve-based (2.37 mm) and surface-based (3.53 mm) methods.

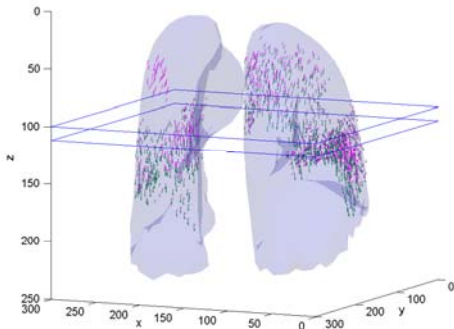
The median of TRE for the combined curve- and surface-based registration was 1.85 mm compared to 1.44 mm for the intensity-based method. Several reasons may lead to larger TRE for the combined curve- and surface-based method, such as inconsistency in segmentations of vessels in the two images. Ambiguous segmentation of lung surface near the hilum may leads to large misregistration errors in this area. Figure 3.3b shows a difficult case in the data with irregular centerlines in the back of the lungs. Registration of lung images based on such geometrical structures as vessels centerlines and lung surfaces can be naturally improved by including airways and lung fissures into the presented framework.

In order to understand where are the main differences between the feature-based and intensity-based method, we visualized discrepancy between the two deformation fields in Figure 3.3a. For illustration purpose, we sparsely selected points, where the orientation between deformation vectors were above  $60^\circ$  and with the magnitude of discrepancy vectors more than 3 mm and plotted inside the lung area. Interestingly, the discrepancy between the feature- and intensity-based methods were localized.

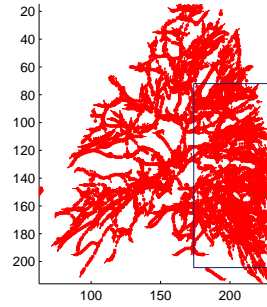
We further investigate image slices located at the areas, where the discrepancy between the two methods was the largest (blue cut planes in Figure 3.3a). Figure 3.4 shows the difference image with the moving image subtracted from the fixed image for both registration methods. Overall, lung surfaces and small vessels were aligned more accurately with the feature-based registration method.

Another important component of currents is the length or the weight of the direction vector. For the task of registration of repeated lung CT images, the current for a small vessel could be given more weight than for a large vessel, leading to more accurate registration of small vessels. This is an important advantage of current-based registration over intensity-based method, where small vessels with low contrast to surrounding lung tissue have negligible impact on the overall cost function. In this chapter we used equal weights for all currents and normalized the length to 1.

On average, 35.5% of landmarks were aligned better with the curve- and surface-based registration. The low correlation coefficient (0.5) suggests that the two registration methods align landmarks differently and may be combined into a more robust registration method.



(a) Deformation vectors for the combined curve- and surface-based (magenta) and intensity-based (green) methods



(b) Example of irregular current

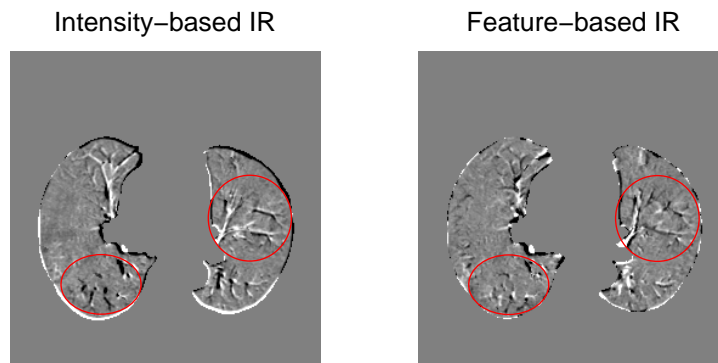
Figure 3.3: (a) An example of discrepancy in deformation fields between the feature-based and intensity-based registration methods. (b) An example of an ambiguous current for the back of the lung.

### 3.5 Conclusion

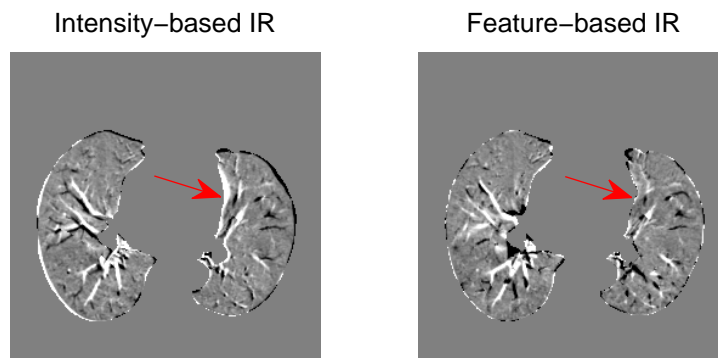
In this chapter, a curve- and surface-based registration method is presented, where lung surfaces and vessel tree centerlines are built-in into the framework of current-based registration. Incorporating both centerlines and surfaces results in more accurate registration than curve- or surface-based registration method alone. The proposed combined curve- and surface-based registration method achieves slightly lower accuracy than intensity-based registration but for 35.5% of landmarks outperformed the intensity-based method. A natural extension of the presented work will be incorporating more anatomical lung structures, such as airways and fissures, to improve the feature-based method.

Results show that the proposed feature-based registration method is robust to inconsistent segmentation and outliers in segmented features and capable of handling imperfect segmentations. In applications where importance of different features varies, the prior weight of a feature may be encoded into the presented registration framework. Results suggest that a natural improvement of registration would be obtained by combining the feature- and intensity-based methods.

I would like to thank Juan Eugenio Iglesias, Medical Imaging Informatics UCLA, for useful suggestion.



(a)



(b)

Figure 3.4: Visual comparison of the combined feature-based and intensity-based registration methods. Slice cuts (a), (b) from the difference image between fixed and deformed image for the intensity- and combined feature-based registration methods were extracted on the same level as the plane cuts in Figure 3.3a. In general, the currents-based registration aligns the vessels and lung surface better, as can be seen in the areas indicated with the red circles and arrows.

## Chapter 4

---

# Lung CT Registration Combining Intensity, Curves and Surfaces

---

*Take a chance and you may lose. Take not a chance and you have lost already.*

— SØREN KIERKEGAARD.

This chapter is based on the publication "Lung CT Registration Combining Intensity, Curves and Surfaces", Gorbunova V., Durrleman S., Lo P., Pennec X., de Bruijne M., in proceedings of IEEE International Symposium on Biomedical Imaging 2010.

---

### 4.1 Introduction

The ultimate goal of an image registration algorithm is to establish dense point-to-point correspondence between two images. Generally, registration of lung CT images is a difficult problem due to the possible large variation between the scans. Scans of the same patient taken at maximum inspiration, can have more than a liter difference in lung volume. The registration of end exhale and end inhale phases of 4D-CT lung images is an even more difficult problem due to the large and non-uniform deformations during the breathing cycle [53].

Image registration methods can be divided into two groups of methods: intensity-based and feature-based. Feature-based methods establish deformations based

on low-dimensional features derived from the original images, e.g. points, curves or surfaces, while intensity-based methods consider intensity information over complete image. Several feature-based registration methods were developed for lung CT scans [37, 76, 25, 99]. However intensity-based registration methods are prevalent for the general purpose registration of lung CT scans [36, 48, 53, 52, 81, 29, 28, 39].

Intensity-based registration methods generally produce more accurate results [37, 24, 46]. Major drawback of the feature-based registration methods is the necessity to extract reliable features, e.g., landmark-based registration methods [39, 99, 25] require manually selected landmarks, and methods similar to the iterative closest point algorithm [37] require a good parameterization of the segmented structures. Recently, a current-based registration method was proposed for registration of surfaces [93] and curves [97, 94], where no point correspondence is required. We previously adapted the current-based registration for lung CT scans and showed that the accuracy of the current-based registration was slightly worse than the accuracy of the intensity-based registration [46], although in 35 % of the landmarks, the current-based registration resulted in smaller target registration error.

While feature-based method can more accurately estimate deformation fields of the features, the intensity-based method can benefit from its results and improve the overall accuracy of alignment further away from the features. The direct combination of two different registration methods is usually not possible, particularly if the underlying deformation models are different. For example, in parametric non-rigid registration, deformation fields are commonly modeled with spline functions [36, 61, 44], while in non-parametric methods deformation fields are usually modeled using partial differential equations [62].

We propose a combined registration method, where the deformation field of an intensity-based registration is constrained with the results from a feature-based method. This constrained registration method is alternated with the feature-based registration method in an iterating scheme. A similar solution was previously proposed by Hellier et al. [100] where the deformation field between the corresponding sulcus lines was incorporated into the optic-flow based registration of the brain MRI scans. In the work [100], sulci in the two images were parameterized and deformations were obtained from corresponding points in the two curves. In contrast, in our feature-based registration curves and surfaces are represented without direct point correspondence, therefore consistent segmentation of the curves or surfaces in the two images is not required for the combined registration.

Our previous work [60] presented a combined registration method, where the intensity information was combined with the anatomical lung structures, e.g., vessel centerlines and lung surfaces. In this chapter we give a detailed description

of the proposed combined registration algorithm and evaluate performance on a publicly available set of 10 lung CT image pairs [39] with manually annotated landmarks.

## 4.2 Background and Previous Work

Generally, simple geometrical structures, e.g., points, curves and surfaces, which corresponds to distinct anatomical structures, are used as features in the feature-based registration. However more advanced features such as attribute vector [101] or filter response [102, 103] are also used in feature-based registration. Growing number of papers propose to combined geometrical features with intensities in registration framework [90, 104, 105, 106, 58, 100, 100, 76, 59, 103].

K. Rohr et al. [104] and H.J. Johnson et al. [90] proposed to combine landmarks with intensity based registration via an alternating approach. Minimization of the target registration error was alternated with the minimization of dissimilarity measure between images, thus achieving an optimal transformation.

Methods that combine curves and surfaces with intensities for registration purposes are common in magnetic resonance imaging field for analysis of brain MRI scans. Sulci and cortical surfaces were successfully combined with the intensity information [105, 58, 100, 106]. P. Cachier et al. [105] and P. Hellier [100] presented similar methods, where sulci were represented with a set of points and deformations between the corresponding sulci and intensity-based similarity measure were both incorporated into a cost function. D.L. Collins et al. [106] investigated different approach, where chamfer distance between the corresponding sulci was introduced into the registration framework. T. Liu et al. [58] proposed a multi-step registration algorithm where volumetric mapping was further improved by sequential surface alignment.

On contrary, combined feature-based and intensity-based registration of lung CT scans is not well investigated topic [76, 59, 103, 60, 107]. Recently, Li et al. [76] developed an image registration algorithm for lung CT images, where the intensity-based registration was improved with the subsequent bio-mechanical simulation of lung inflation obtained from lung surface deformations. The study [59] presents another hybrid method, where the registration algorithm integrates intensity-based and feature-based methods. The cost function incorporates difference in intensities and difference in the distances to the annotated surfaces. Similar approach was proposed in [107], where cost function incorporates dissimilarity between the original images and between the vessel probability images. A hybrid approach where features of lung CT scans were determined from an eigenvalue analysis and further considered along with the intensities in the registration procedure [103]. In all the above studies, results showed improvement of the combined registration methods compare to the registration methods based

on the intensity alone.

### 4.3 Method

Section 4.3.1 briefly repeats the feature-based registration method from the Chapter 3. The non-rigid intensity-based registration method from the Chapter 2 is described in the Section 4.3.2. Detailed description of the proposed registration, where the intensity is constrained with the deformations of anatomical lung structures, is given in the Section 4.3.3. Finally, the details of an iterating scheme, where the combined registration is alternated with the feature-based registration is described in the Section 4.3.4.

#### 4.3.1 Current-based Registration

In our previous work, we developed a feature-based registration, where vessel centerlines and lung surfaces, were used to establish spatial correspondence between lung CT scans [46]. Both vessel centerlines and lung surfaces were represented in a framework of currents and aligned using the metric on currents. The current  $\mu$  for a vessel centerline  $C$  is represented by tangential vectors attached to the centerline points, and for a triangulated surface  $S$  it is represented by normal directions attached to the centers of each face. Figure 4.1a show an example of the currents for the vessel centerlines, and the lung surfaces is shown in Figure 4.1b.

Norms of a currents for curves and surfaces,  $\mu(C)$  and  $\mu(S)$ , are defined via a path integral along the curve or a flux integral through the surface [94]. The cost function between anatomical lung structures in a fixed image  $C_f$  and  $S_f$  and a moving image  $C_m$  and  $S_m$  is defined as a weighted sum of the similarity measures between currents for the vessel centerlines  $C_f$  and  $C_m$ , the similarity between currents for surfaces the  $S_f$  and  $S_m$ , and a regularization term:

$$E(C_f, S_f; C_m, S_m) = \gamma_C \|\mu(C_f) - \mu(\phi \cdot C_m)\|_{W^*}^2 + \gamma_S \|\mu(S_f) - \mu(\phi \cdot S_m)\|_{W^*}^2 + \gamma_\phi \int_0^1 \|v_t\|_V^2 dt. \quad (4.1)$$

Diffeomorphic transformation  $\phi$  of curves and surfaces was modeled in the framework of large deformation diffeomorphic matching [94], where deformation of each feature point is defined by a velocity vector field  $v_t = \phi'_t$ . The smooth velocity field  $v_t$  is described via a Gaussian kernel with standard deviation  $\lambda_V$ , where  $\lambda_V$  determines the typical scale of the deformations [97]. The smoothness of the currents is determined by the parameter  $\lambda_W$  [97].

#### 4.3.2 Intensity-based Registration via B-Splines

In this chapter we used a multi-resolution B-Spline image registration framework [61] for the intensity-based registration. First, lung regions were extracted



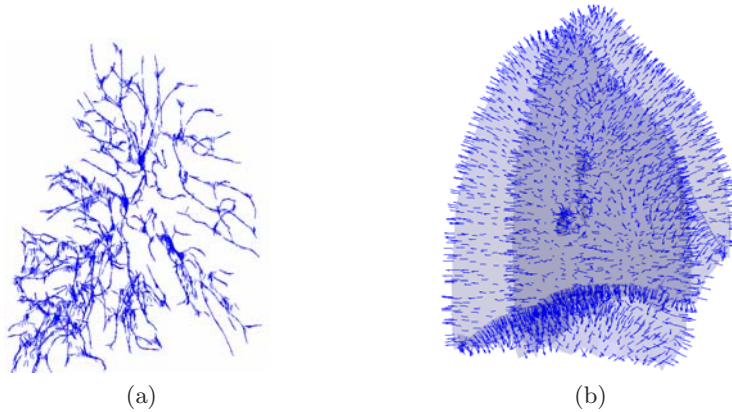


Figure 4.1: Example of currents constructed for the segmented vessel centerlines (a) and the lung surfaces (b), both seen from the side.

from the CT images and the background value was set to 0 HU. Images were aligned with affine transform  $T_A$ . Subsequently, a series of  $N$  B-Spline transforms  $T_{\text{B-Spline}}^{i=1..N}$  with decreasing grid size was applied to the affinely registered images. Thus, the final deformation is a composition of the affine transform and  $N$  levels of the B-Spline transforms:

$$T_{\text{final}}(\mathbf{x}) = T_{\text{B-Spline}}^N \circ \dots \circ T_{\text{B-Spline}}^1 \circ T_A(\mathbf{x}), \quad (4.2)$$

where  $\mathbf{x}$  is a point in the fixed image domain  $\Omega_f$ . We use the sum of squared intensity differences as the similarity measure between the images,

$$E_{\text{int}}(I_f, I_m; T) = \frac{1}{|\Omega_f|} \int_{\Omega} [I_f(\mathbf{x}) - I_m(T(\mathbf{x}))]^2 d\mathbf{x}, \quad (4.3)$$

where  $I_f(\mathbf{x})$  is the fixed image, defined in the fixed image domain  $\Omega_f$ ,  $I_m(\mathbf{y})$  is the moving image, defined in the moving image domain  $\Omega_m$ . After each level of transform the moving image  $I_m(\mathbf{y})$ , where  $\mathbf{y} = T(\mathbf{x})$ , is deformed, interpolated using linear interpolation and provided for the next level of transform.

### 4.3.3 Constrained Registration

We propose to constrain the intensity-based registration of Section 4.3.2 with the deformation field obtained from the current-based registration of Section 4.3.1. We constrain B-Spline deformation field  $\vec{D}_{\text{B-Spline}}(\mathbf{x})$  to match the given deformation field  $\vec{D}_{\text{curr}}(\mathbf{x})$  by minimizing the  $\mathcal{L}_2$  distance between the deformations. Since the current-based registration uses anatomical lung features to establish the correspondence, the deformation field in locations close to the extracted features is expected to be more reliable than further away from the features. Thus, we propose to incorporate a spatially varying weight  $w(\mathbf{x}) \in [0; 1]$ ,  $\mathbf{x} \in \Omega_f$  into the constraint between the deformation fields, which defines the trade off between

matching intensity and deformations for every voxel  $\mathbf{x}$ . The combined cost function then consists of the sum of squared intensity differences similarity function and constraint on the deformation field:

$$\begin{aligned} E(I_f, I_m; T) &= E_{int} + \lambda E_{def} = \\ &= \frac{1}{|\Omega|} \int_{\Omega} (1 - w(\mathbf{x})) [I_f(\mathbf{x}) - I_m(T(\mathbf{x}))]^2 d\mathbf{x} \\ &+ \frac{\lambda}{|\Omega|} \int_{\Omega} w(\mathbf{x}) \|\vec{D}_{\text{B-Spline}}(\mathbf{x}) - \vec{D}_{\text{constr}}(\mathbf{x})\|^2 d\mathbf{x}, \end{aligned} \quad (4.4)$$

where the constraining deformation field is  $\vec{D}_{\text{constr}}(\mathbf{x}) = \vec{D}_{\text{curr}}(\mathbf{x})$  and the coefficient  $\lambda$  compensates for the difference in units of the two terms. The deformation field  $\vec{D}_{\text{B-Spline}}(\mathbf{x})$  is a vector field defined as  $\vec{D}_{\text{B-Spline}}(\mathbf{x}) = T(\mathbf{x}) - \mathbf{x}$ . Using vector notation, the gradient of the cost function (4.4) can be computed explicitly:

$$\begin{aligned} \mathcal{D}_{\mathbf{a}} E(I_f, I_m; T) &= - \frac{2}{|\Omega|} \int_{\Omega} (1 - w(\mathbf{x})) [I_f(\mathbf{x}) - I_m(T(\mathbf{x}))] \cdot [\mathcal{D}_{\mathbf{x}} I_m \mathcal{D}_{\mathbf{a}} T] d\mathbf{x} \\ &- \frac{2\lambda}{|\Omega|} \int_{\Omega} w(\mathbf{x}) (\vec{D}_{\text{B-Spline}}(\mathbf{x}) - \vec{D}_{\text{curr}}(\mathbf{x}))^T \mathcal{D}_{\mathbf{a}} T d\mathbf{x}. \end{aligned} \quad (4.5)$$

Where the symbol  $\mathcal{D}_{\mathbf{x}}$  denotes the spatial gradient vector operator  $\mathcal{D}_{\mathbf{x}}(\cdot) = (\frac{\partial}{\partial x_1}(\cdot); \frac{\partial}{\partial x_2}(\cdot); \frac{\partial}{\partial x_3}(\cdot))$ , and the symbol  $\mathcal{D}_{\mathbf{a}}$  denotes the gradient vector operator with respect to the transform coefficients  $\mathcal{D}_{\mathbf{a}}(\cdot) = (\frac{\partial}{\partial a_1}(\cdot); \dots; \frac{\partial}{\partial a_N}(\cdot))$ .

In the multi-level framework of the intensity-based image registration described in Section 4.3.2, each level of the transform is constrained separately. The initial affine transform is not constrained, and for the subsequent  $N$  levels of the B-Spline transform the deformation field at a given point is constrained with the remaining deformation field, as follows:

$$\begin{aligned} \vec{D}_{\text{constr}}^{\text{level}}(\mathbf{x}) &= \vec{D}_{\text{curr}}(\mathbf{x}) - \vec{D}_{\text{aff}}(\mathbf{x}) - \vec{D}_{\text{B-Spline}}^1(T_{\text{aff}}(\mathbf{x})) - \dots - \\ &- \vec{D}_{\text{B-Spline}}^3(T_{\text{B-Spline}}^2 \circ T_{\text{B-Spline}}^1 \circ T_{\text{aff}}(\mathbf{x})). \end{aligned} \quad (4.6)$$

#### 4.3.4 Iterative Scheme

The described combined registration method is naturally extended to an iterative approach where registration alternates between the combined method from the Section 4.3.3 and the current-based registration from Section 4.3.1. The interaction of the two registration algorithm presented in the Figure 4.2. After an iteration  $i$  of the combined registration, the vessel centerlines currents  $\mu(C_f)$  and lung surfaces currents  $\mu(S_f)$  extracted from the fixed image are deformed with the obtained complete transform  $T^i$  and a new iteration of the current-based registration of Equation (4.1) restarted on the deformed currents, defined as:

$$\mu^{i+1}(C_f) = \mu(C_f \circ T^i) \quad (4.7)$$

$$\mu^{i+1}(S_f) = \mu(S_f \circ T^i) \quad (4.8)$$

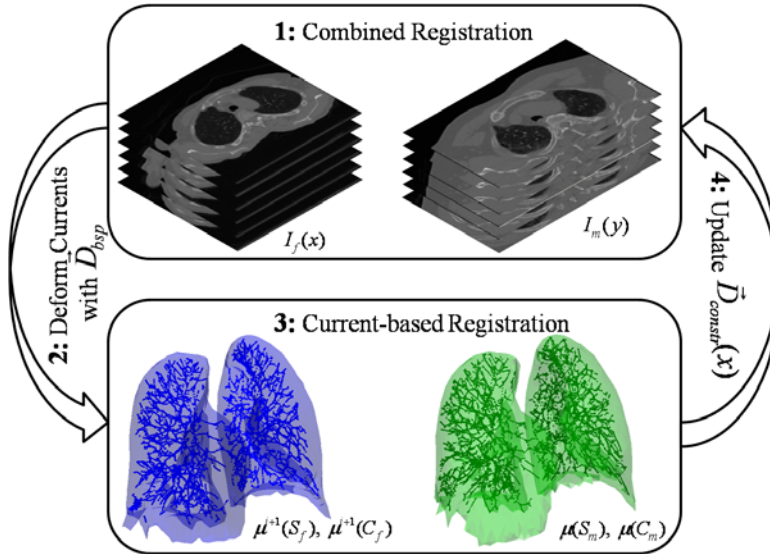


Figure 4.2: The workflow of the iterative image registration. The combined registration from Section 4.3.3 is applied between the original fixed image  $I_f(\mathbf{x})$  and the original moving image  $I_m(\mathbf{y})$  with the constrain on the deformation field  $\vec{D}_{constr}(\mathbf{x})$ . The subsequent current-based registration from Section 4.3.1 is applied between the deformed currents of the fixed image  $\mu(C_f)$ ,  $\mu(S_f)$  and the currents of the moving image  $\mu(C_m)$ ,  $\mu(S_m)$ . Detailed description of the algorithm is given in Algorithm 4.1.

Since the current is a set of vector points, the deformed current is obtained from the deformation of the start and the end points of each vector. Details on the initialisation and step-by-step description of the iterative process is summarised in Algorithm(4.1). Using the described scheme we can iterate the current-based and the combined registration gradually improving the result.

## 4.4 Experiments

### 4.4.1 Data

We conducted experiments on ten publicly available image pairs extracted at the end exhale and end inhale phases of 4D-CT scans [39]. The study also provides 300 manually placed landmarks for each image pair. The landmarks were uniformly distributed over the lungs. In-plane resolution of the images varied from  $0.97 \times 0.97$  mm to  $1.16 \times 1.16$  mm and slice thickness was 2.5 mm. For each pair, the image extracted at end inhale phase of 4D CT image was registered to the image extracted at end exhale phase.

Algorithm 4.1: Algorithm describes the iterating scheme illustrated in Figure 4.2.

---



---

**Problem Statement:** For every point  $\mathbf{x} \in \Omega_f$  find the corresponding point  $\mathbf{y} = \mathbf{x} + \vec{D}(\mathbf{x})$  in the moving image domain  $\Omega_m$ .

---



---

**Initialization:** Initial constraining deformation field  $\vec{D}_{\text{constr}}^0 = 0$ , the weight image  $w(\mathbf{x}) = 0$ , transform parameters  $\mathbf{c}^0 = 0$  and the fixed image currents  $\mu^0(C_f) = \mu(C_f)$ ,  $\mu^0(S_f) = \mu(S_f)$ .

**for**  $i = 0 \dots N$  **do**

- 1: Run combined image registration with the constraining deformation field  $\vec{D}_{\text{constr}}^i$  and initial guess on transform coefficients  $\mathbf{c}_{ini}^i$ ,
- 2: Compute the deformation field  $\vec{D}_{\text{B-Spline}}^{i+1}$  of the complete transform  $T^i$  and deform the fixed image currents  $\mu^{i+1}(C_f, S_f) = \mu(C_f \circ T^i; S_f \circ T^i)$ ,
- 3: Run current-based image registration between  $\mu(C_m, S_m)$  and  $\mu^{i+1}(C_f, S_f)$
- 4: Update the deformation field  $\vec{D}_{\text{constr}}^{i+1} = \vec{D}_{\text{constr}}^i + \vec{D}_{\text{B-Spline}}^{i+1}$  and the transform coefficients  $\mathbf{c}_{ini}^{i+1} = \mathbf{c}_{converged}^i$ .

**end for**

---



---

#### 4.4.2 Setup of the Current-based Registration

Lung fields and main bronchi were segmented as described in [108]. From the segmented lung regions, the lung surfaces triangulation were constructed using the marching cube algorithm and further simplified in order to decrease the number of faces [73]. The normal directions were attached to the center of each facet, the length was normalized to 1 mm and the orientation was set to point outwards from the lung surface. Figure 4.1b shows an example of the constructed current for the lung surfaces.

Vessel tree was segmented using the algorithm as in [87] with the intensity threshold  $-600$  HU. The internal parameters of the segmentation algorithm such as ratios of the Hessian eigenvalues were set to  $m_1 = 0.75$  and  $m_2 = 0.5$ . Vessel centerlines were extracted using a 3D thinning algorithm [89]. Finally, tangential directions of the vessel centerlines were computed via local principal component analysis in a  $7 \times 7 \times 7$  voxel size cube. The orientation and the length of the tangential direction is important in the current-based registration, therefore we normalized the length of the first principal vector to 1 mm and the orientation was set to point outwards from the image center. Figure 4.1a shows an example of the constructed currents for the vessel tree segmented from the right lung.

We applied the current-based registration from Section 4.3.1 to register vessel trees and lung surfaces. The internal parameters of the current-based registration were set to  $\lambda_W = 5$  mm for the vessel currents,  $\lambda_W = 10$  mm for the surface currents,  $\lambda_V = 25$  mm,  $\gamma_C = 1$ ,  $\gamma_S = 0.01$  and the regularization parameter

$$\gamma_\phi = 10^{-4}.$$

### 4.4.3 Setup of the Intensity-based Registration

For the intensity-based registration Section 4.3.2, three levels of B-Spline transform  $N = 3$  were applied in the multi-resolution strategy. The size of the B-Spline grid at each level was set to  $3 \times 3 \times 3$  (approx.  $94 \times 73 \times 87$  mm),  $6 \times 6 \times 6$  (approx.  $47 \times 36 \times 43$  mm), and  $12 \times 12 \times 12$  (approx.  $23 \times 18 \times 22$  mm), respectively. After each level of the transform, the moving image was deformed with respect to the sum of the deformation fields from the previous levels. We used linear interpolation method to reconstruct intensity values in non-grid point voxels.

Each level of the transformation was optimized separately using a stochastic gradient descent algorithm [51]. The numbers of the voxel samples  $N_s$  in the optimisation process were chosen proportional to the number of optimized parameters at each level and at least  $10^4$ . For the Affine transform the  $N_s = 10^4$  and for the three sequential levels of the B-Spline transform  $N_s = (10^4, 10^4, 5 \cdot 10^4)$  voxel samples respectively. The maximum number of iterations was set to  $N_i = 1000$  for every level of the transform.

### 4.4.4 Setup of the Combined Registration

The proposed iterative registration method from the Section 4.3.4 was iterated for the total number of iterations  $N = 10$ . The internal parameters of the intensity-based module were fixed as described in the Section 4.4.3, whereas the parameters of the current-based module were set differently from registration method in Section 4.3.1. The current-based module was applied after the intensity-based registration, therefore the major deformations were captured by the intensity-based registration thus the remaining deformations were expected to be smaller than the full deformations. Therefore, we decreased the internal parameters of the subsequent current-based registration module to  $\lambda_W = 2.5$  mm for both vessel and surface currents,  $\lambda_V = 25$  mm and  $\gamma_\phi = 10$  for all the subsequent iterations. The coefficient  $\lambda$  from (4.3) was set to  $5 \times 10^3$  for all the iterations.

The weight image  $w(\mathbf{x})$  was constructed as follows, first the lung surfaces were extracted from the segmented lung regions. Reliable segmentation of vessels and lung surfaces near the hilum area is a difficult task, therefore we erased the lung surfaces and vessel centerlines near the hilum area by first dilating the left and right main bronchus with a disk element of radius 20 voxels in axial plane and then deleting the constructed dilation from the lung surfaces and vessel centerlines. We computed the distance map to the lung surfaces and vessel centerlines and evaluated the Gaussian kernel with the size  $\kappa_w = 5.0$  mm on the distance image. Figure 4.3 shows an axial, a coronal and a sagittal slice of a weight image.

Figure 4.3: An example showing from left to right axial, sagittal and coronal slices of a spatially varying weight image  $w(\mathbf{x})$ .

## 4.5 Results

The overall accuracy of a registration method was defined as the average Euclidean distance between the landmarks, target registration error (TRE), in millimeters. For each image pair 300 manually placed landmarks were available in the study [39].

Table 4.2: The target registration error (TRE) in [mm] is reported.

It	TRE [mm]
1	$2.39 \pm 2.16$
2	$1.91 \pm 1.79$
3	$1.79 \pm 1.56$
4	$1.79 \pm 1.46$
5	$1.74 \pm 1.36$
6	$1.73 \pm 1.29$
7	$1.72 \pm 1.27$
8	$1.72 \pm 1.25$
9	$1.71 \pm 1.24$
10	$1.71 \pm 1.23$

The average and the standard deviation of the TRE was obtained from the complete set of 3000 landmarks. Evaluation of the combined image registration approach at each iteration averaged over the complete set of images is reported in the Table 4.2. Figure 4.5a shows the evolution of the mean TRE for each case individually and Figure 4.5b shows box-plots of the TRE for each iteration of the proposed combined registration algorithm.

The TRE of the three registration methods with only the intensity term, described in the Section 4.3.2, the current-based registration, described in the Section 4.3.1, and the proposed iterative combined registration, described in Section 4.3.3 are compared in the Table 4.3. The overall mean and standard deviation before the registration was  $8.69 \pm 5.99$  mm. The TRE after the image registration procedure was reduced to  $1.71 \pm 1.23$  mm,  $2.39 \pm 2.16$  mm and  $3.45 \pm 3.91$  mm for the proposed combined registration, the intensity-based and the current-based registration respectively. The decrease of the average target registration error with the proposed combined registration ranged from  $-17.8\%$  to  $55.4\%$  or  $-0.21$  mm to  $2.78$  mm compared to the average TRE of the intensity-based registration. The average improvement of the proposed registration method over the intensity-based registration method was  $28.5\%$  or  $0.68$  mm.

Figure 4.4 illustrates how the vessel centerlines were deformed during the iterations of the proposed combined registration method. Vessels in the upper part of the lungs were correctly matched already after the first iteration of the algorithm however alignment of the vessels in the lower part was inaccurate. The proposed combined registration gradually improved alignment of the vessels in the lower part of the lungs.

Visual comparison of the intensity-based registration with the proposed combined registration is presented in the Figures 4.6-4.7. Images were first masked

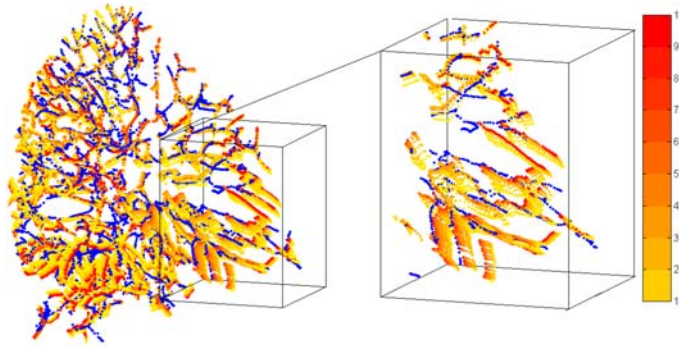


Figure 4.4: Vessel centerlines of the moving image (blue curves) are overlaid with the deformed vessels centerlines of the fixed image (yellow to red curves). Deformed vessel centerlines are displayed in colors ranging from yellow to red with respect to the iteration number of the iterative registration algorithm.

Table 4.3: The mean and standard deviation of target registration error at the landmark positions in [mm] before the registration (Original); after the current-based registration (Curr); after the proposed combined registration (Comb It#); and after the intensity-based registration (Intensity).

N	Original	Combined at It#10	Intensity-based	Current-based
1	$3.89 \pm 2.78$	$1.39 \pm 0.96$	$1.18 \pm 0.57$	$1.47 \pm 0.72$
2	$4.34 \pm 3.90$	$1.17 \pm 0.56$	$1.26 \pm 0.68$	$2.19 \pm 1.98$
3	$6.94 \pm 4.05$	$1.39 \pm 0.75$	$1.91 \pm 1.15$	$3.30 \pm 3.05$
4	$9.83 \pm 4.86$	$1.70 \pm 1.03$	$2.12 \pm 1.52$	$3.34 \pm 2.67$
5	$7.48 \pm 5.51$	$1.87 \pm 1.45$	$2.23 \pm 1.79$	$3.83 \pm 3.54$
6	$10.89 \pm 6.97$	$1.98 \pm 1.07$	$1.98 \pm 1.11$	$2.85 \pm 1.67$
7	$11.03 \pm 7.43$	$1.85 \pm 1.11$	$2.99 \pm 2.09$	$3.61 \pm 4.05$
8	$14.44 \pm 7.16$	$2.24 \pm 2.18$	$5.02 \pm 3.96$	$5.59 \pm 7.01$
9	$9.24 \pm 3.54$	$1.85 \pm 1.06$	$2.05 \pm 1.06$	$2.89 \pm 2.07$
10	$7.63 \pm 6.04$	$1.72 \pm 1.12$	$2.50 \pm 2.11$	$5.47 \pm 5.66$
All	$8.69 \pm 5.99$	$1.71 \pm 1.23$	$2.39 \pm 2.16$	$3.45 \pm 3.91$

using the segmented lung regions and background value was set to 0HU. Then the moving image was deformed with respect to the obtained deformation field, interpolated using linear interpolation and subtracted from the fixed image. Figure 4.6 shows the only example where the proposed registration algorithm resulted in the larger TRE  $1.39 \pm 0.96$  mm than the intensity-based registration algorithm  $1.18 \pm 0.57$  mm. Figure 4.7 shows another extreme case, where the proposed registration algorithm resulted in the largest decrease of the TRE  $2.24 \pm 2.18$  mm compared to the  $5.02 \pm 3.96$  mm.

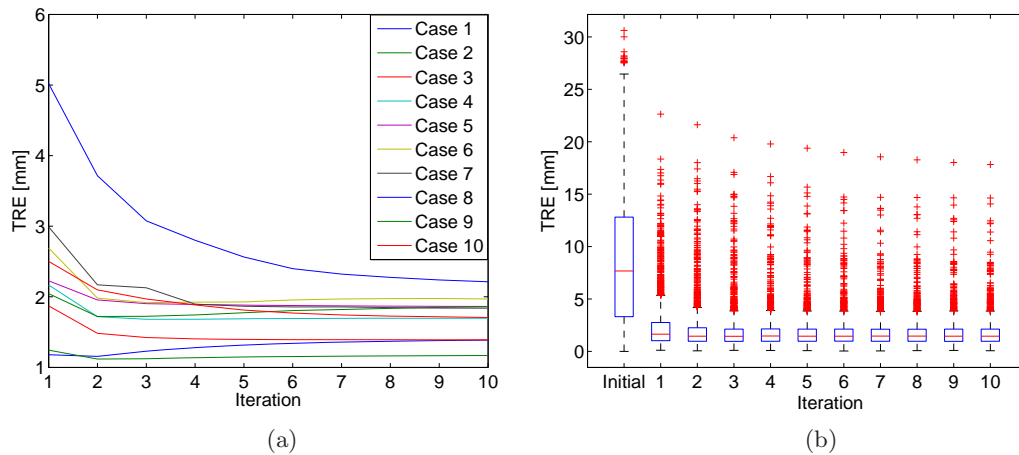


Figure 4.5: Average target registration error [mm] evolution during the iterations of the combined registration method for every image pair in the study, plot (a). Overall distribution of the TRE [mm] showed in the box-plot (b).

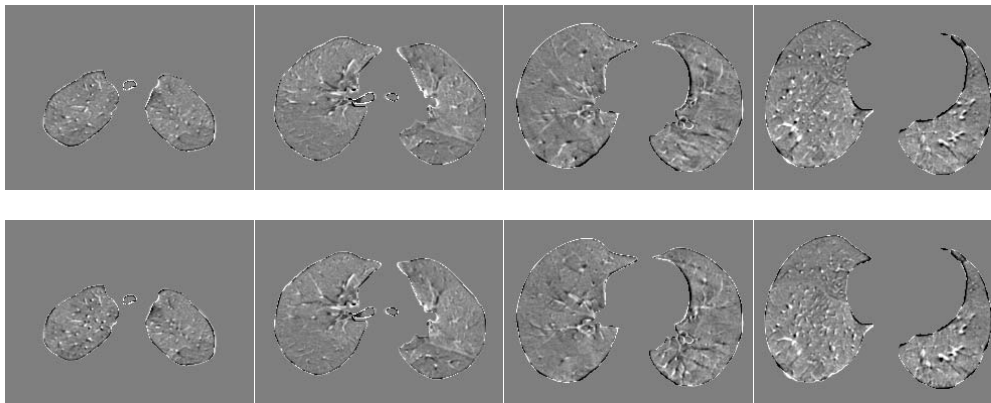


Figure 4.6: The difference images of the intensity-based registration (first row) and the corresponding difference images of the combined registration (second row) for the case #1. The TRE of the intensity based registration was  $1.18 \pm 0.57$  mm and  $1.39 \pm 0.96$  mm for the two registration methods respectively. The difference images are displayed in the intensity range  $[-300; 300]$ HU.

## 4.6 Discussion

Recently, Hub et al. [47] showed that an intensity-based registration of lung CT scans is more reliable in areas with clearly defined vessels, while areas without distinctive features were registered generally less accurate. Since an optimization process of sum of square difference similarity function is driven by gradient of the moving image, intensity-based registration method will result in less certain align-



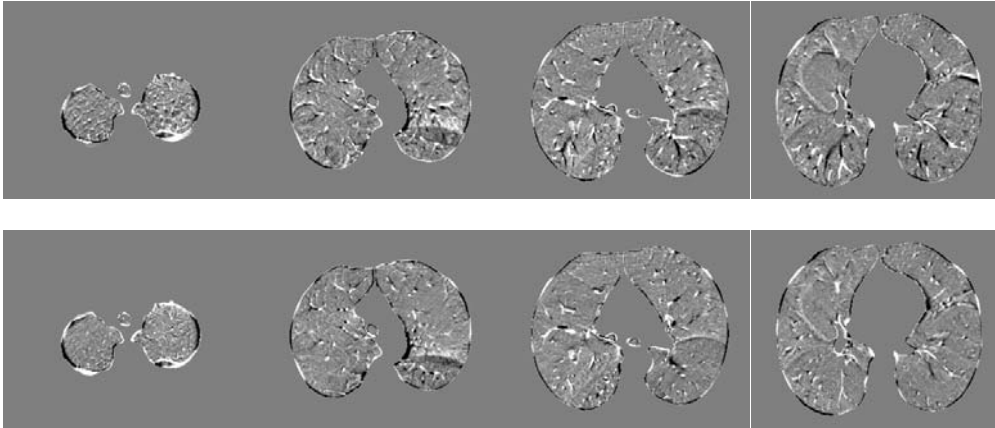


Figure 4.7: The difference images of the intensity-based registration (first row) and the corresponding difference images of the combined registration (second row) for the case #8. The TRE of the intensity based registration was  $5.02 \pm 3.96$  mm and  $2.24 \pm 2.18$  mm for the two registration methods respectively. The difference images are displayed in the intensity range  $[-300; 300]$ HU.

ment of small, peripheral vessels. Conversely feature-based registration methods rely less on the original intensities and generally include additional information such as connectivity, filter responses, or shape models. In the current-based registration method, described in Section 4.3.1, the segmented vessel tree and lung surfaces are represented with the set of unit vectors regardless of the original image intensities. Thus large and small vessels are assigned the same weight in the feature-based registration and are equally important in the registration.

Assuming that the feature-based registration aligns unclear structures like peripheral vessels better than the intensity-based registration we incorporated the deformations of the segmented features into the intensity-based registration via a spatially varying weight. The maximum weight of 1 is at the lung borders and the vessel centerlines and decays elsewhere, thus implies the perfect fit of the deformation fields at the location of the segmented structures. However, the actual effect of the constraint propagates within the support of the closest B-spline basis functions. Thus final solution brings minimum both to the sum of squared intensity differences far from an anatomical structure and the differences in the deformation fields close to it.

The proposed combined approach resulted in more accurate registration assessed via the set of manually selected landmarks. The average target registration error was  $1.71 \pm 1.23$  mm for the proposed combined method compared to the intensity-based registration alone  $2.39 \pm 2.16$  mm and the current-based registration of features  $3.45 \pm 3.91$  mm. The registration errors were comparable with the results reported in another study [56], where the registration procedure was

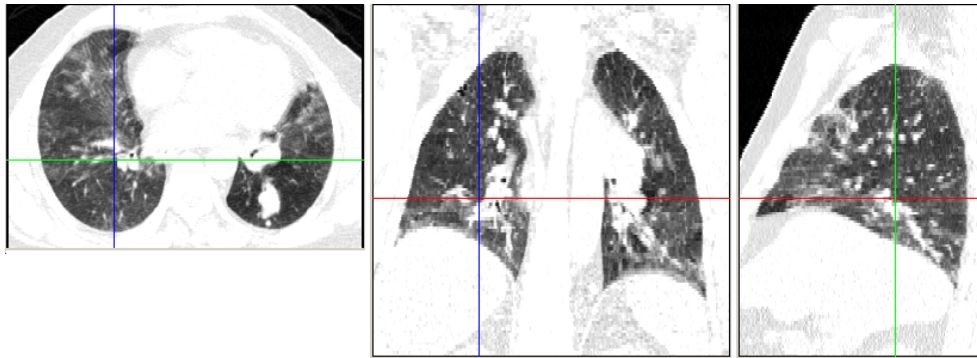
applied to only the first three cases and the final accuracy was computed on an extended set of landmarks. The reported average target registration error was 1.59 mm.

In nine out of ten cases, the proposed combined method outperformed the intensity-based registration. The case where the average target registration error increased after the combined registration is displayed in Figure 4.6. Although the increase in TRE was statistically significant, there were no major mis-registrations in the final difference images. While in the another extreme case in Figure 4.7, where the combined registration significantly decrease TRE compared to the intensity-based method, alignment of the vessels was visibly better.

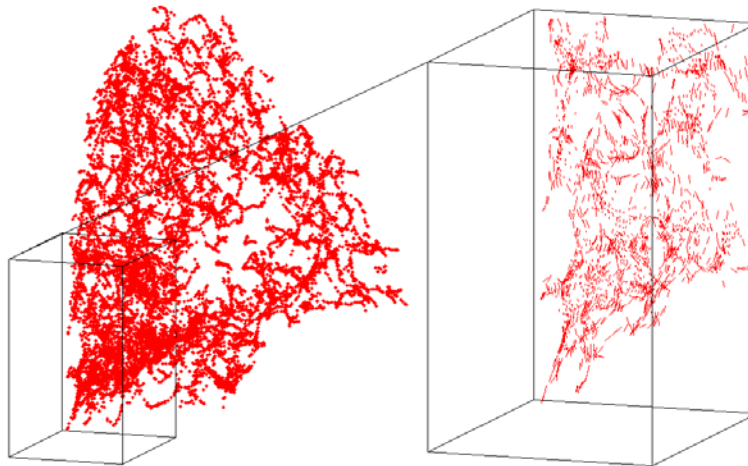
Several reasons may lead to a significantly higher TRE for the current-based registration alone. First, appearance of the vessels in the end inhale and the end exhale phases of the 4D-CT scans varies significantly therefore reliable segmentation with a fully-automatic method is difficult to obtain. Furthermore, centerline extraction is difficult to reproduce with the voxel size accuracy. Figure 4.8 shows an example where the segmented vessel centerlines did not resemble vessels because of the apparent motion artifacts and abnormalities presented in the image. Second, current-based registration alone was performed on twice larger scale than the current-based registration in the combined approach. A more consistent comparison should be performed where a current-based registration is applied in multi-resolution strategy.

The registration task of lung CT scans, where intensity abnormalities presented only in one of the images could be one of the potential applications of the proposed combined registration. Another application could be registration of lung vasculature with attached nodules, where accurate registration of vessels is a key issue in nodule growth analysis.

To conclude, in this chapter we presented a general framework for combining feature-based and intensity-based registration methods via incorporating a constraint on deformation field. We combined the previously developed current-based registration of anatomical lung structures with an intensity-based registration method and applied it to ten image pairs of end inhale and end exhale phases extracted from 4D-CT images. The proposed registration method performs better than the feature-based method and the intensity-based method alone. The improvement assessed using a set of manually selected landmarks was on average 28.5% or 0.68 mm compare to the intensity-based method and 50.4% or 1.74 mm compare to the current-based registration methods.



(a)



(b)

Figure 4.8: An example of a difficult case (#6), where the vessel centerlines were unreliable. Plot (a) shows an axial, a sagittal and a coronal slices of the original image, plot (b) shows the corresponding vessel centerlines of the right lung and zoom with the constructed currents.



## Chapter 5

---

# Evaluation of Methods for Pulmonary Image Registration 2010: Challenge Results

---

This chapter is based on the publication "Mass Preserving Image Registration: Results of Evaluation of Methods for Pulmonary Image Registration 2010 Challenge", Gorbunova V., Sporning J., Lo P., Dirksen A., de Bruijne M., to appear in proceedings of Grand Challenges in Medical Image Analysis Workshop in conjunction with Medical Image Analysis and Computer Assisted Intervention Conference 2010.

---

### 5.1 Introduction

The EMPIRE challenge was organized in conjunction with the Grand Challenges in Medical Image Analysis Workshop at Medical Image Analysis and Computer Assisted Intervention Conference (<http://empire10.isi.uu.nl/>). The goal of the challenge was two-fold, first to compare existing registration methods from different research groups on exactly the same dataset; and second to investigate common problems of the existing registration methods.

We applied the mass preserving registration algorithm, described in Chapter 2 for the challenge. Since the challenge was conducted during the last month of my PhD study, further improvements of the mass preserving method are not in the scope of the thesis and should be considered as recommendations to those researchers who decided to work with the similar registration method.

## 5.2 Evaluation

The goal of this section is to describe evaluation methodology which has been used in the EMPIRE challenge. The methodology was developed by challenge organizers and analysis was performed also by challenge organizers. Here I provide brief overview of the evaluation methodology in order to facilitate understanding of the final results. For details please check the web-page <http://empire10.isi.uu.nl>.

Evaluation procedure consisted of four main components: alignment of lung boundaries; alignment of major fissures; target registration error between manually annotated point pairs; and analysis of singularities in the deformation field.

### 5.2.1 Lungs Boundary Alignment Scores

Lung fields were segmented using an automatic hybrid method based on the conventional regional growing technique with an additional error detection step, where an advanced multi-atlas segmentation algorithm was applied for final corrections [109]. Once the lung fields were segmented and lung borders were obtained, two regions in the images were defined. The first region  $\Omega^{out}$  was the outer region outside the lung fields but within 2 to 20 mm distance from the lung borders; the second inner region  $\Omega^{in}$  was inside the lung fields also within 2 to 20 mm distance from the lung borders. This procedure was applied for both the fixed and the moving images, thus resulting in total of four regions  $\Omega_f^{in}$ ,  $\Omega_f^{out}$  and  $\Omega_m^{in}$ ,  $\Omega_m^{out}$ . Given the deformation field  $\vec{D}$  from a registration procedure, all voxels within the two regions in the fixed image were deformed with respect to the deformation field. Voxels which were placed in the opposite region in the moving region were considered as the *wrongly matched voxels*. An example of a wrongly matched voxel is a voxel in the inner region  $\mathbf{v} = (x, y, z) \in \Omega_f^{in}$ , which was positioned in the outer region in the moving image  $(\mathbf{v} + \vec{d}(x, y, z)) \in \Omega_m^{out}$  after applying the deformation  $\vec{d}(x, y, z)$ . Final error score was the percentage of the *wrongly matched voxels* that belongs to one region in the fixed image but positioned into the opposite region in the moving image.

### 5.2.2 Major Fissures Alignment Scores

Fissures are important anatomical lung structures which separate lungs into lobes. Human right lung contains three lobes including the upper, middle and lower lobes, while left lung contains only two lobes upper and lower lobes. Both lungs have the major (or oblique) fissures, which separate the upper lobe from the lower lobe in the left lung and upper and middle lobe from the lower lobe in the right lung. Lung lobes can slide along the fissures and result in discontinuous deformations at the lung fissures. Furthermore, fissures are very thin structures and it is particularly difficult to match the fissures accurately. Fissures were seg-

mented using an automatic segmentation algorithm [110] and further inspected and corrected manually if needed. The horizontal fissure which separates upper lobe from the middle lobe in the right lung was not included into the analysis. To assess accuracy of a registration algorithm near the major fissures the same analysis was done as for the lung borders. Inner and outer regions were defined in the fixed and the moving lungs, and the final fissure alignment score was defined as the overall percentage of lung voxels inside the outer or inner regions in the fixed image, which were positioned in the wrong region in the moving image.

### 5.2.3 Point Correspondence Scores

Lungs boundaries alignment and fissures alignment scores only assessed registration accuracy in the limited area of lung fields. In order to investigate registration accuracy inside the lung fields, corresponding points or landmarks were annotated in the two images. Analysis of the target registration errors between the corresponding landmarks remains the most widely used quantitative measure of accuracy of an image registration algorithm. For the EMPIRE challenge, landmarks were identified semi-automatically as in [23]. For each image pair 100 landmarks well distributed inside the lung fields were annotated. The maximum, minimum and average Euclidean distance between the corresponding landmarks were computed for each image pair in left, right or both lungs. Additionally, average distance between the landmarks in anterior-posterior direction (AP), in superior-inferior direction (SP), and in left-right (LR) directions was computed for both lungs.

### 5.2.4 Singularity of Deformation Field Scores

Singularity points in the lung fields were defined as points where determinant of the Jacobian of the transform was below or equal to 0. Determinant of the Jacobian characterizes local deformations, if  $\det(J(\mathbf{x})) > 1$  then expansion of the fixed image space is observed in the point  $\mathbf{x}$  which corresponds to the contraction of the moving image space in the transformed point  $\mathbf{y} = T(\mathbf{x})$ . Vice versa,  $\det(J(\mathbf{x})) < 1$  is contraction of the fixed image space at the point  $\mathbf{x}$  or expansion of the moving image space in the point  $\mathbf{y}$ . The percentage of points where  $\det(J(\mathbf{x})) \leq 0$  was defined as the final singularity score of the registration algorithm.

## 5.3 Results

Registration was applied on a set of 20 image pairs where each pair was obtained from the same subject. Two image pairs were sheep chest CT scans, the remaining 18 were human lung CT scans. Dataset included images acquired from different

Table 5.1: Table presents total scores of the evaluation procedure for each case, and an average over the complete dataset. Absolute difference between the lung volumes,  $\Delta TV = V_f - V_m$ , and relative lung volume difference  $100 \cdot 2 \cdot \frac{V_f - V_m}{V_f + V_m}$  are given in the table for reference. Symbol \* marks sheeps lung CT scan image pairs.

ID	$\Delta TV$		Total scores averaged over both lungs							
	[%]	[L]	Fiss. [%]	Rnk	Bound. [%]	Rnk	Sing. [%]	Rnk	Point [mm]	Rnk
1	-61.66	-2.86	0.0487	11	0.2261	24	0	11.5	5.20	22
2	0.32	0.04	0	15	0.0003	26	0	12.5	0.62	24
3	8.20	0.60	0.0040	27	0.0016	24	0	12	0.76	28
4*	-21.61	-0.42	0	16.5	0.0006	8	0	14	1.11	13
5	2.39	0.11	0	16	0	13	0	13.5	0.35	25
6	-2.29	-0.08	0.0043	15	0	16	0	14	0.36	14
7	-43.92	-3.39	0.7549	11	0.2187	22	0	10	5.08	23
8	-21.72	-1.27	0.0812	18	0.0213	21	0	12.5	1.88	24
9	3.70	0.28	0.0002	16	0.0023	26	0	13	0.94	27
10*	-30.12	-0.62	0	15	0.0055	16	0	13	1.56	12
11	-23.49	-1.39	0.2693	21	0.0896	20	0	11.5	2.27	25
12	0.46	0.03	0.0378	31	0	10	0	14.5	1.32	30
13	8.13	0.35	0.1106	21	0.0030	25	0	13	1.26	24
14	-43.93	-3.00	3.0189	12	0.1691	21	0	9.5	5.42	20
15	5.20	0.29	0	7	0.0003	25	0	12.5	0.77	22
16	19.45	0.47	0.4048	26	0.0010	18	0	13.5	1.34	18
17	4.76	0.25	0.0551	19.5	0	6.5	0	14	1.16	23
18	-46.44	-2.91	5.1067	23	0.0954	21	0	10.5	5.14	22
19	-1.10	-0.06	0	12	0	14	0	14.5	0.65	25
20	-45.63	-2.66	9.9041	28	0.1233	24	0.012	26	6.76	22
All	-14.47	-0.81	0.9900	18	0.0479	19	0.0006	13	2.19	22

phases of 4D-CT and 3D scans, images acquired at maximum inspiration and maximum expiration breathholds. Subjects with severe lung disease as well as relatively healthy subjects were included into the study. In-plane spacing varied from  $0.4688 \times 0.4688$  mm to  $0.9766 \times 0.9766$  mm, and slice thickness varied from 0.6 mm to 2.5 mm. Lung masks were provided along with the image pairs by challenge organizers.

Table 5.1 presents total evaluation scores averaged over both left and right lung regions, for reference we included lung volume difference between the fixed and the moving images. For every evaluation score in the Table 5.1, the rank of our registration method is given. The rank indicates the final placement of our mass preserving registration method compare to the other 33 participants. Correlation of the relative lung volume difference with the landmark alignment score was  $-0.87$  ( $p < 10^{-6}$ ); with the lung boundary alignment score was  $-0.85$  ( $p < 10^{-5}$ ); with the fissure alignment score was  $-0.52$  ( $p = 0.02$ ); and with the singularity score =  $0.31$  ( $p = 0.18$ ).

Elaborate results for every case in the study are reported in the Appendix 5.4.



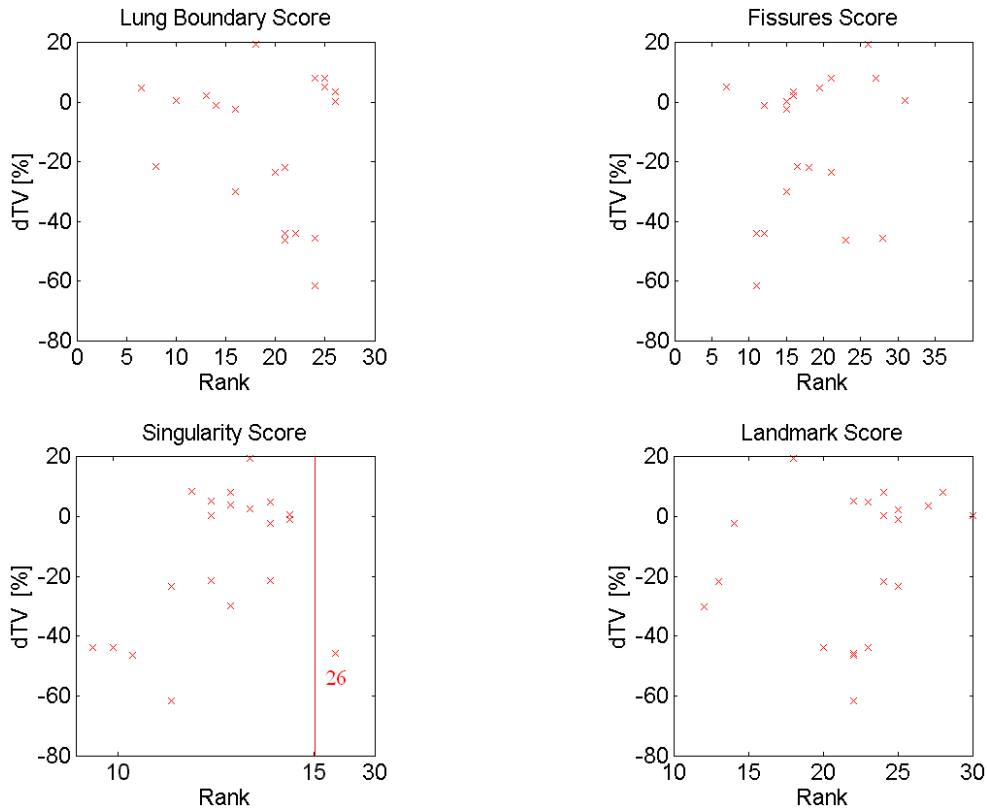


Figure 5.1: Each subplot shows overall rank versus the relative volume difference.

Table 5.2 presents details on the landmark alignment score, the target registration error, computed in only the left or the right lung regions, in the upper or the lower regions of both lungs or over the both right and left lung regions. Additionally, the minimum, maximum and average of target registration error and average distance in anterior-posterior (AR), superior-inferior (SI) and left-right (LR) directions is reported in the Table 5.2. Table 5.3 presents details on the segmentation-based scores computed for only the left or the right lung regions; for only the upper or the lower regions of both lungs or over the both right and left lung regions.

Figure 5.1 displays relationship between the ranking of the mass preserving registration and the relative lung volume difference between the fixed and the moving images.

In order to investigate spatial properties of the mass preserving registration method, we performed Student's t-test between the scores for the right and the left lung regions, between the scores for the top and the bottom regions of both lungs and between the three spatial directions AP, SI and LR. The following scores differ significantly:

- Alignment of the upper part of lung boundaries 0.0033% is significantly

better than the alignment of the lower part of lung boundaries 0.0826%, the corresponding p-value 0.014;

- Landmark alignment in the upper part 1.92 mm is significantly smaller than landmark alignment in the lower part 2.49 mm,  $p = 0.030$ ;
- Landmark alignment in the LR direction 0.75 mm is significantly smaller than both alignment in AP 1.24 mm and SI 1.13 mm directions, with the corresponding p-values 0.0034 and 0.0097 respectively.

## 5.4 Discussion

Data analysis showed clear asymmetry in the fixed and the moving images. Lung CT scan with smaller lung volume in the image pair were usually set as the fixed image in the registration framework. The relative volume difference between the lungs of the fixed and the moving images was on average  $\Delta TV = 100 \cdot \frac{V_f - V_m}{(V_f + V_m)/2} = -14.47\%$ . This potentially leads to a more difficult registration problem than if the image with the bigger lung volume is chosen as the fixed image. In the mass preserving registration, the moving image is being deformed and interpolated after every level of the transform. Shrinkage of the moving image results in the increase of the density of lung parenchyma thus making lung parenchyma less distinguishable from the vessels. In the opposite case, the moving image is expanded and intensity of lung parenchyma decreases potentially leading to a more accurate alignment of vessels.

In 19 out of 20 cases, the proposed method produced invertible deformations. In the remaining case only for negligible percentage of voxels 0.01 % singularities occurred. Since we did not include the regularizer as a part of the cost function, we can conclude that with the multi-level transform strategy and the current setup of the optimization procedure we almost achieved invertibility of the transformation.

Overall mass preserving registration achieved an average landmark alignment score of  $2.19 \pm 2.05$  mm and the median was 1.29 mm. The average ranking for this score 22.15 was larger than average ranking for the remaining scores, ranging from 13.28 to 19.03. One of the reasons for large landmark alignment score could be in a large B-Spline grid, the average size of the B-Spline grid at the final transform level was  $2.4 \times 1.8 \times 2.3$  cm<sup>3</sup>. Although it could be further improved by applying additional levels of B-Spline transform with smaller grid size, it will also lead to the increase of the complexity of the image registration algorithm. In all the 5 cases, where the average landmark alignment score was above 5 mm, optimization procedure was stopped because of the maximum number of iterations 1000 was reached. This could be improved by increasing the number of maximum iterations.

Figure 5.1 shows weak trend between the rank of the mass preserving registration algorithm and the relative lung volume difference for the fissure alignment and singularity scores. For the scan pairs with large lung volume difference, the mass preserving image registration method was generally ranked higher.

The mass preserving registration method was ranked 20th out of 34 participants. Consider the fact that number of degrees of freedom in the transformation function was relatively small, we conclude that our registration algorithm was able to capture lung deformations with a relatively simple deformation model with acceptable spatial accuracy of 2.19 mm.

Table 5.2: Table presents the complete set of evaluation scores based on the corresponding set of landmarks including average TRE in millimeters in only the left or the right lungs; average distance in anterior-posterior (AR), superior-inferior (SI) and left-right (LR) directions; in the lower or the upper parts of both lungs; minimum, maximum and the average TRE in the complete set of landmarks. Symbol \* marks sheep lung CT scans.

ID	Point Correspondence Scores [mm]										
	Left	Right	AP	SI	LR	Upper	Lower	min	max	Average	
1	5.86	4.70	3.45	2.51	1.77	4.97	5.42	0.68	19.69	5.20	
2	0.64	0.59	0.26	0.28	0.27	0.51	0.73	0.00	1.72	0.62	
3	0.85	0.66	0.30	0.26	0.41	0.61	0.91	0.00	3.58	0.76	
4*	0.90	1.32	0.59	0.56	0.38	1.41	0.81	0.00	8.98	1.11	
5	0.33	0.37	0.14	0.15	0.14	0.25	0.46	0.00	1.63	0.35	
6	0.39	0.33	0.15	0.14	0.10	0.32	0.38	0.00	1.62	0.36	
7	4.51	5.72	3.06	2.32	2.07	3.81	6.43	0.00	17.04	5.08	
8	1.57	2.16	1.13	0.91	0.67	1.55	2.16	0.00	9.13	1.88	
9	0.74	1.10	0.42	0.43	0.35	0.71	1.18	0.00	4.26	0.94	
10*	0.86	2.28	1.01	0.67	0.52	2.42	0.73	0.00	14.78	1.56	
11	3.42	1.47	1.25	1.32	0.68	0.97	3.82	0.00	16.65	2.27	
12	1.24	1.39	0.81	0.53	0.52	1.14	1.46	0.00	6.16	1.32	
13	1.10	1.48	0.54	0.65	0.54	1.21	1.31	0.00	9.86	1.26	
14	3.54	7.16	3.53	2.57	1.55	4.40	6.49	0.00	19.00	5.42	
15	0.69	0.84	0.39	0.34	0.29	0.65	0.87	0.00	5.49	0.77	
16	1.13	1.47	0.49	0.78	0.45	0.91	1.74	0.00	5.09	1.34	
17	0.92	1.43	0.52	0.58	0.39	0.87	1.54	0.00	4.50	1.16	
18	3.75	6.43	3.21	2.87	1.46	4.20	6.08	0.00	15.18	5.14	
19	0.62	0.67	0.30	0.27	0.25	0.50	0.83	0.00	2.71	0.65	
20	8.93	4.98	3.16	4.47	2.20	7.00	6.42	0.64	20.34	6.76	
All	2.10	2.33	1.24	1.13	0.75	1.92	2.49	0.07	9.37	2.20	

Table 5.3: Table presents the complete set of segmentation-based evaluation scores computed in only the left or the right lung or in both lungs. Additionally, lung boundary alignment score was computed in only the top or the bottom parts of both lungs. Symbol \* marks sheeps lung CT scan image pairs.

ID	Fissure Alignment Scores [%]			Boundary Alignment Score [%]					
	Left	Right	Total	Left	Right	Upper	Lower	Total	
1	0.17459	0.0179002	0.0485731	0.170507	0.28429	0.00273874	0.386644	0.226142	
2	0	0	0	0.00057818	0	0	0.000552154	0.000299014	
3	0.0152027	0	0.00396923	0.00184373	0.00134262	0.0011553	0.00201998	0.00160423	
4*	0	0	0	0.00151906	0	0.00126241	0	0.000628783	
5	0	0	0	0	0	0	0	0	
6	0	0.00708509	0.00431069	0	0	0	0	0	
7	0.611073	0.920477	0.754927	0.260655	0.172568	0.00333274	0.381276	0.218733	
8	0.0934568	0.0728086	0.0812415	0.0248915	0.0175348	0	0.0383258	0.0213195	
9	0	0.000338741	0.000218947	0.00418127	0.000239068	0.000399101	0.00385775	0.00225434	
10*	0	0	0	0.0126541	0.000396052	0.011021	1.38E-05	0.00549563	
11	0.800645	0.00686595	0.269345	0.164437	0.0150489	2.51E-05	0.15856	0.0896095	
12	0	0.0573747	0.0378424	0	0	0	0	0	
13	0.134571	0.0663076	0.110621	0.00123178	0.00490996	0.000173452	0.00553673	0.00304393	
14	5.29557	1.03882	3.01887	0.128602	0.209147	0.0295364	0.29218	0.169147	
15	0	0	0	0.000501205	0	0	0.000466908	0.000257115	
16	0.148368	0.485892	0.404845	0.00131663	0.000769482	0	0.00184002	0.00104999	
17	0.142005	0	0.0551116	0	0	0	0	0	
18	12.183	0.493686	5.10668	0.112339	0.0779893	0.00570641	0.166464	0.0954141	
19	0	0	0	0	0	0	0	0	
20	14.2453	7.22431	9.90405	0.0939973	0.153227	0.0108393	0.214154	0.123334	
All	1.692189075	0.519593294	0.990030273	0.048962738	0.046873109	0.003309496	0.082594555	0.047916607	



## Chapter 6

---

# Mass Preserving Image Registration For Monitoring Emphysema Progression

---

This chapter is based on the publication "Weight Preserving Image Registration For Monitoring Emphysema Progression", Gorbunova V., Lo P., Ashraf H., Dirksen A., Nielsen M., de Bruijne M., in proceedings of Medical Image Computing and Computer Assisted Intervention Conference in 2008.

---

### 6.1 Introduction

Chronic Obstructive Pulmonary Disease (COPD) is the fourth leading cause of death in the world [5]. COPD encompasses both small airway disease and emphysema which is characterized by the destruction of lung parenchyma. The current gold standard for diagnosing COPD is based on lung function tests (LFT) such as the forced expiratory volume in one second (FEV1) and forced vital capacity (FVC). These methods are well suited for diagnosing COPD but lack the sensitivity and reproducibility to detect mild emphysema or small changes in disease status.

CT analysis allows the quantification of emphysema with a higher accuracy, even in early stages. Emphysematous regions appear as areas with low-attenuation in CT scans of the lungs, suggesting that CT image intensities can be used to quantify the severity of emphysema. Averaged lung density,  $n$ -th percentile density, and relative area with attenuation below, e.g., -910HU (em-

physema index, RA-910HU) have all been successfully applied as emphysema measures. However, current CT emphysema measures have two major drawbacks: measurements are averaged over the complete lung region, which makes it difficult to detect small and localized differences, and they are strongly influenced by variations in the inspiration level [17]. For accurate monitoring of disease development and progression one should be able to analyze regional changes. We propose to use image registration for this purpose. Non-rigid image registration of lung CT scans has previously been used as an aid in determining growth of lung nodules [74], but to our knowledge has not been applied to longitudinal studies of emphysema.

There exist two fundamentally different approaches to analyzing regional changes in longitudinal studies or image sequences using registration. One approach considers an almost perfect registration and subsequently analyzes the deformation field. This approach has for example been applied to lung SPECT and CT scans to analyze breathing motion [53]. The second approach aims at compensating for gross deformation caused by other factors not related to the disease process, and subsequently analyzes the differences in local appearance or intensity between the target and the registered image as a measure of disease progression. The second approach is taken in this chapter: registration is used to correct for expected normal lung deformation and differences in inspiration level between scans, whereas the finer scale disease process of growing and merging emphysema bullae is revealed in the difference images.

In repeated breath-hold scans of the same subject, the difference in total lung volume between scans is often more than a half liter, even if the subjects are instructed to hold their breath at maximum inspiration. This has a large effect on the density of lung tissue in the CT scan and on common density derived measures of emphysema [17]. To correct for differences in inspiration level we used an assumption of total lung mass preservation throughout the respiratory cycle which was discussed previously in [82]. We propose to constrain the image registration to preserve local and global mass of lungs during deformation and adjust voxel intensity values with respect to local volume changes. A composition of affine and multi-level free-form registration was applied to align the baseline scan with the follow up and the obtained difference maps were analyzed for local tissue loss. The main advantages of the proposed method are: (a) it is robust to significant difference in total lung volume between baseline and follow-up scans; (b) it is capable of estimating regional destruction of lung tissue.



## 6.2 Method

### 6.2.1 Mass Preserving Image Registration

First baseline image was registered to the system of the coordinates of the follow up image using the mass preserving image registration presented in Chapter 2. Because experiments in this Chapter were conducted in the beginning of my PhD study, the set-up of the registration framework here differs from the Chapter 2. The essential differences are: regions outside of the lung fields were included in the fixed and the moving image regions; a limited memory algorithm for bound constrain optimization [111] was used to minimize the dissimilarity function; and complete set of image voxels in the image was used in the optimization procedure.

Once the correspondence between the two images was obtained, baseline image was deformed and intensities of the baseline image were adjusted with respect to the local volume change measured from the determinant of Jacobian of the transformation.

### 6.2.2 Measure of disease progression

We first subtracted the registered baseline image from the follow up, thus forming an intensity difference image, where negative areas indicate local loss of lung tissue and thus progression of emphysema. To reduce the effect of noise and interpolation artifacts around vessel boundaries, the resulting difference maps were filtered with a median filter of size  $3 \times 3 \times 3$  and masked with the dilated vessel masks and segmented lung regions from both images.

We assumed only voxels  $\mathbf{x} = (x, y, z)$  with intensity difference within the interval  $(-500; -50)$  are disease-related. The reason for this is to remove artifacts due to interpolation and inaccurate registration and reduce the influence of noise. We compute an average density loss measure  $\mu$  over overlapping lungs volume  $V$ , by summing the disease-related intensity differences, given as:

$$\mu = \frac{1}{V} \sum_{\Omega_D} I_f(\mathbf{x}) - I_b(T(\mathbf{x})), \quad (6.1)$$

where the symbol  $\Omega_D = \{\mathbf{x} | I_f(\mathbf{x}) - I_b(T(\mathbf{x})) \in (-500; -50)\}$  denotes the set of voxels with intensity difference within the  $(-500; -50)$  HU range.

## 6.3 Experiments and results

We evaluated the method on a set of 29 low dose CT image pairs collected from the Danish Lung Cancer Screening Trial. The images are selected such that they have a considerable difference in total lung volume ( $0.6 \pm 0.5L$ ) between baseline and follow up scans. The in-plane resolution was  $0.78 \times 0.78$  mm and the slice

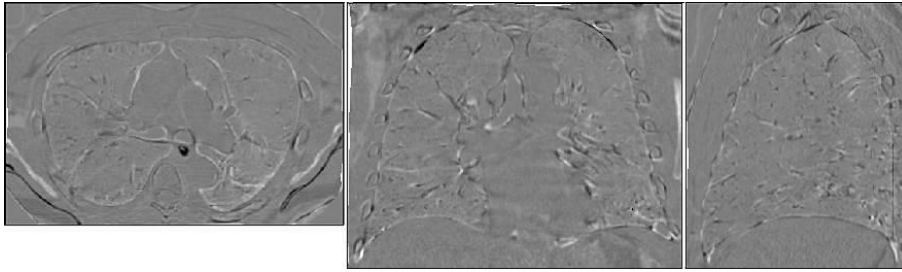


Figure 6.1: A difference image illustrating an example of mass-preserving image registration, showing the deformed baseline image subtracted from the follow up image. From left to right the mid-axial, coronal and sagittal slice is shown.

thickness was 1 mm. Image pairs have a time interval between baseline and follow up of approximately one year. Of these, at baseline 11 subjects had no COPD according to the GOLD guidelines [5], 5 were classified as having mild COPD, and 3 as moderate ( $FEV_1/FVC = 66 \pm 10$ ). At follow up, 5 subjects are healthy, 11 have mild COPD and 3 have moderate COPD. 10 Image pairs were collected with a 3 month interval, of these 9 subjects had no COPD and 1 had mild COPD ( $FEV_1/FVC = 74 \pm 4$ ).

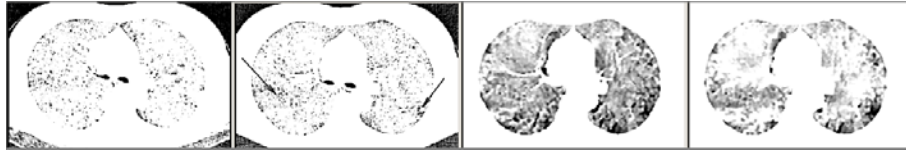
To save computation time, the original CT lung scans were cropped according to the segmented lungs before image registration. A gradient descent algorithm was used for optimizing the parameters of the affine transform. The multi-level B-Spline transform was optimized using the L-BFGS method [36]. The first level was performed on a grid resolution of  $3 \times 3 \times 3$  grid points on the image domain, the second level on a resolution of  $6 \times 6 \times 6$  grid points and the finest level on a  $12 \times 12 \times 12$  or  $2.5 \times 2.5 \times 2.5 \text{ cm}^3$  grid. The first two levels of the B-Spline transform were applied to smoothed and sub-sampled versions of the images whereas the finest level was applied to the original images. The image registration framework was implemented with ITK [69].

Figure 6.1 shows the result of described image registration technique for an arbitrary subject. Differences in subject positioning within the CT scanner and part of the changes in lung volume were corrected via affine registration. The first level of the B-Spline transformation aligned global lung structures such as the lobes and diaphragm. The second level performed on the same resolution as pulmonary segments and adjusted internal lung deformations. Finally, the finest level corrects for deformations in the subsegmental level. Figure 6.1 shows clearly that the majority of internal lung structures is aligned with about 2-3 voxels accuracy; only a few misalignments near the lung and bronchial tree borders remain.

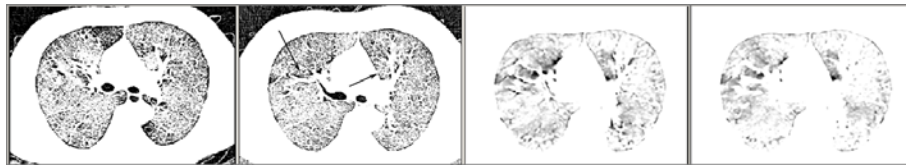
To verify the preservation of mass during the registration procedure, we compute the lung mass for standard and mass-preserving registered images and compare it with corresponding original image characteristics. The mean squared

difference between the lung mass of the original baseline image and the registered image for standard image registration is  $1.18 \cdot 10^{-2}$ kg, two times more than for the proposed mass-preserving registration technique ( $5.09 \cdot 10^{-3}$ kg).

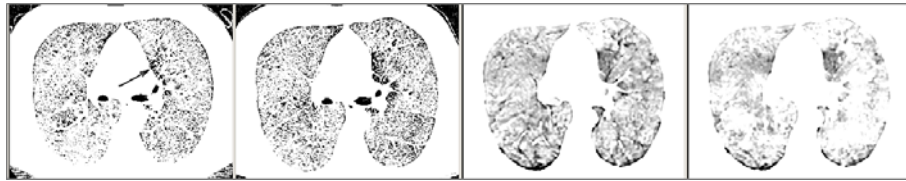
Examples of obtained local disease progression maps for four subjects with various values of differences in total lung volume and LFT are shown in Figure 6.2. The areas outside the lung and the vessel masks were excluded from the difference maps. Representative axial slices were chosen close to the carina point.



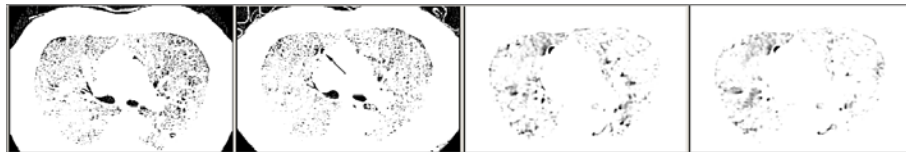
(a) Patient with  $\Delta TLV = 0.64L$ , mean FEV1/FVC = 69 and decrease in FEV1/FVC = -9.3



(b) Patient with  $\Delta TLV = 0.48L$ , mean FEV1/FVC = 68 and decrease in FEV1/FVC = -7.5



(c) Patient with  $\Delta TLV = 1.06L$ , mean FEV1/FVC = 65 and decrease in FEV1/FVC = -11.2



(d) Patient with  $\Delta TLV = 0.39L$ , mean FEV1/FVC = 69 and decrease in FEV1/FVC = -0.3

Figure 6.2: Left most column shows an axial slice of a baseline scan; second column shows the most corresponding slice on the follow up scan with notable regions of emphysema progression indicated by arrows; third column shows the corresponding slice in difference image for the standard image registration technique; most right column shows difference image for mass-preserving image registration. The original scans were both thresholded at -910HU to reveal emphysematous areas; the difference images were median filtered and viewed at intensity window: 0 to -200.

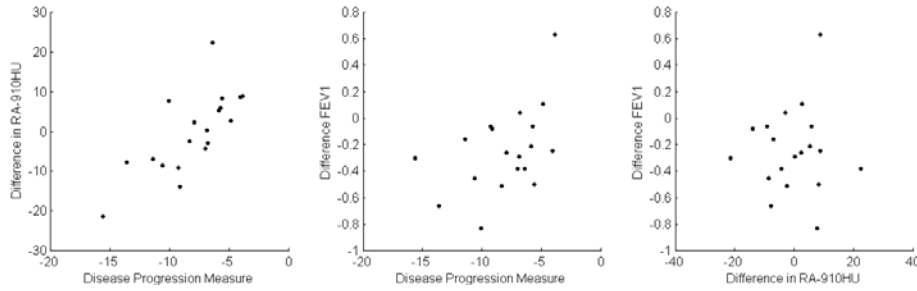


Figure 6.3: Relationship between annual difference in FEV1, difference in RA-910HU, and averaged mass loss in HU computed for the mass-preserving image registration for a group with 1 year time interval.

The resulting measure of disease progression is correlated to changes in RA-910HU and difference in FEV1 between baseline and follow up visits. Scattered plots are shown in Figure 6.3 We expect a positive correlation between our measure of disease progression and annual difference in FEV1 but not perfect, since this measure is known to vary substantially [14]. The correlation coefficient between annual difference in FEV1 and the registration based measure for standard registration  $\rho_{\text{diffFEV1},\mu} = 0.1$  ( $p = 0.69$ ) and for mass-preserving registration  $\rho_{\text{diffFEV1},\mu} = 0.47$  ( $p = 0.04$ ). The correlation coefficient between RA-910HU and registration based measurement for standard case  $\rho_{\text{RA-910},\mu} = 0.82$  ( $p < 0.01$ ) and for mass-preserving registration  $\rho_{\text{RA-910},\mu} = 0.73$  ( $p < 0.01$ ). The correlation coefficient between RA-910HU and annual difference in FEV1  $\rho_{\text{diffFEV1,RA-910}} = 0.04$  ( $p = 0.87$ ).

To estimate influence of the inspiration level for the standard and mass-preserving image registration techniques we computed the correlation coefficients between difference in total lung volume and proposed disease progression measure for subjects scanned with 3 month interval. The correlation coefficient between the difference in total lung volume and the registration based measure for standard registration  $\rho_{\text{diffTV},\mu} = 0.92$  ( $p < 0.01$ ) and for mass-preserving registration  $\rho_{\text{diffTV},\mu} = 0.51$  ( $p = 0.14$ ).

## 6.4 Discussion and Conclusions

The proposed image registration method performed well for cases with considerable total difference in lung volume between baseline and follow up scans, both mass-preserving and standard registration generally align internal lung structures within 2mm.

The proposed mass-preserving image registration maintained the total mass of the lungs better than a standard registration approach. Remaining deviation between the original and registered image mass occurred due to natural limitations of the image registration technique such as the smoothing effect caused by

linear interpolation and B-spline transformation.

The first three subjects in Figure 6.2 had a substantial increase in total lung volume from baseline to follow up, causing RA-910HU as well as standard registration to overestimate the changes in emphysema. The mass-preserving difference maps appear less dark in areas where there is no apparent disease progression in the original images. The darker areas in the mass-preserving difference maps correspond to localized areas of local emphysema progression clearly visible in the original images, while the difference maps based on standard image registration suggest a more diffuse tissue loss in the entire lung region. In the fourth case, where the difference in total lung volume was relatively small, both methods performed similar.

Comparison of the average local tissue loss with RA-910HU revealed a good, but not perfect correlation which indicates that the two measures may carry different information. Although we found low correlations with annual difference in FEV1 in this small sample, the measure based on mass preserving registration does seem to agree better with annual difference in FEV1 than do RA-910 and local progression measured using standard registration. This suggests that the proposed method may be more sensitive to subtle changes in disease status. It should be noted that the annual loss of tissue in most subjects with emphysema is very low, especially among normal smokers and mild COPD subjects, which constituted the majority of our test population. In future work we will investigate the proposed measures in a larger sample and with longer follow-up times.

To conclude, we propose an image registration based method for quantification of COPD disease progression which can estimate local destruction of lungs tissue and is less effected by differences in inspiration level than currently available methods.



## Chapter 7

---

# Early Detection of Emphysema Progression

---

*None of us is as smart as all of us.*

— JAPANESE PROVERB.

This chapter is based on the publication "Early Detection of Emphysema Progression", Gorbunova V., Jasobs S., Lo P., Dirksen A., Nielsen M., Bab-Hadiashar A., de Bruijne M., to appear in proceedings of Medical Image Computing and Computer Assisted Intervention Conference in 2010.

---

### 7.1 Introduction

Emphysema is one of the most common chronic obstructive pulmonary diseases [5]. It is characterized by irreversible destruction of the lung parenchyma and usually caused by smoking [112].

In clinical practice, the severity of emphysema is commonly assessed using different lung function tests. Along with the lung function tests chest CT scans has been used for diagnosis of emphysema and detection of emphysema progression. The standard CT density scores, such as relative area (RA) below certain threshold, e.g. -950 HU or -910 HU, and the n-th percentile density (nPD) of the lungs, were applied to estimate the emphysema progression [17, 16]. CT densitometry

scores have shown to be more sensitive measures of emphysema progression than lung function tests [16].

One of the major drawbacks of the standard CT density scores is their dependency on the inspiratory level [31, 29]. Another important drawback is the lack of sensitivity, since the emphysema progression could only be measured once the intensity of lung tissue decreases below the standard threshold. Texture analysis may resolve this problems. This issue was investigated in a recent study, where a texture-based classification approach was proposed as alternative to the standard emphysema scores [113]. The results showed that the texture-based approach outperforms the RA scores in differentiating diseased from healthy subjects.

Several studies proposed how to estimate disease progression from longitudinal CT scans [31, 29]. Authors proposed a method where CT scans are first registered to a common framework and then emphysema progression is estimated based on the average intensity decrease between the two successive scans.

In this chapter, we propose a more general way of assessing emphysema progression between a pair of images. Firstly, images are registered to a common system of coordinates. Secondly, local image histograms at a given location are obtained and dissimilarity measures between the histograms are computed. Thirdly, a measure of progression at the given location is derived from the dissimilarity measures. Finally, an overall disease progression score between the two images is computed. In this chapter, the proposed method is applied to detect emphysema progression in a longitudinal study of patients with Alpha-1 antitrypsin deficiency [16].

## 7.2 Method

In this section we describe in details the workflow of the algorithm. The first subsection 7.2.1 briefly recalls the image registration method that is applied to establish the spatial correspondence between images. The following subsection 7.2.2 presents how local dissimilarities are constructed. The last subsection 7.2.4 describes how the local disease progression score on subject level is derived from the set of local dissimilarity measures.

### 7.2.1 Registration

The image registration framework presented in Chapter 2 is used to register the follow up images  $I_{2..5}$  to a system of coordinates of the baseline image  $I_1$ . The framework starts with a preprocessing step, where the lung fields are extracted from the CT scans and the background value is set to 0 HU. First, an affine transform is applied to correct for global deformations. Then a series of multi-resolution B-Spline transforms with decreasing grid resolution is applied to



the affinely registered images. Each transform is optimized using the stochastic gradient descent method.

Finally, the moving image is deformed based on the obtained deformation field. To minimize the intensity differences in the fixed and moving images caused by the difference in inspiratory level, the intensities of the deformed image are adjusted with respect to the Jacobian determinant of the deformation field as proposed in Chapter 2.

### 7.2.2 Local Image Features

The registration algorithm results in dense spatial correspondence, but small misregistrations in the order of 1 mm remain. To minimize the impact of the misregistration, we propose to compare points in the different images using a simplified version of locally orderless images (LOI) [114], where the inner, outer and tonal scales were fixed. A local histogram is constructed using a weighted window function centered around a point  $\mathbf{x}_0$ . Given an image  $I(\mathbf{x}_0, \sigma)$  that is observed under the fixed inner scale  $\sigma$ , the LOI at a point  $\mathbf{x}_0$  is defined as follows:

$$h_I(i; \mathbf{x}_0, \alpha) = \frac{1}{(\sqrt{2\pi}\alpha)^3} \int_0^{\mathbf{x}} A(\mathbf{x}, \mathbf{x}_0, \alpha) e^{-(I(x, \sigma) - i)^2} d\mathbf{x}, \quad (7.1)$$

where  $\alpha$  is the outer scale, which corresponds to the size of the window function  $A(\mathbf{x}, \mathbf{x}_0, \alpha) = e^{\frac{(\mathbf{x} - \mathbf{x}_0) \cdot (\mathbf{x} - \mathbf{x}_0)}{2\alpha^2}}$  and  $i$  is an intensity value.

In order to capture different features, in addition to the original image  $I$ , LOIs are also computed from the blurred image and the gradient magnitude. The feature images are all observed under the same scale, which is achieved by blurring the images using a Gaussian kernel with a standard deviation of  $\sigma$ .

### 7.2.3 Dissimilarity Measures

Given the two histograms  $h_1(i; \mathbf{x})$  and  $h_t(i; \mathbf{x})$  obtained in the same anatomical point  $\mathbf{x}$  from the two images  $I_1$  and  $I_t$  respectively, we compute a set of dissimilarity measures  $D(I_1, I_t)(\mathbf{x}) = \{d_i(h_1(i; \mathbf{x}), h_t(i; \mathbf{x}))\}$  between the histograms. Later in text we denote the histograms using shorter notations  $h_1$  and  $h_t$ .

In this paper, we use two classes of dissimilarity measures. First class consists of L1-norm and Kullback-Leibler divergence between the two histograms  $d_1 = \|h_1 - h_t\|_{L_1}$ ,  $d_2 = \|h_1 - h_t\|_{L_2}$ ,  $d_3 = D_{KL}(h_1, h_t)$ . In the second class, the dissimilarity between the local histograms is computed as difference between the individual measures of each of the histograms  $d_i = m_i(h_1) - m_i(h_t)$  [115]: the first four moments, the mode, the energy; and the maximum of difference between the cumulative distribution functions of the histograms  $d_n = \max(\text{cdf}(h_1) - \text{cdf}(h_t))$ .

## 7.2.4 Disease Progression Measure

Since LOIs have a certain region of influence, it is not required to compare each and every point in the images. Therefore, a sparse representation of the image is used for comparison instead, where comparison is only performed on a fixed number of regions,  $N_s$ , sampled randomly within the lung regions.

For every sample  $\mathbf{x}_i$  we compute the set of dissimilarity measures  $D_I = D(I_1, I_t)$  between the images  $I_1$  and  $I_t$ , and the filtered versions of the images  $D_G = D(I_{1,\sigma}, I_{t,\sigma})$ ,  $D_{GM} = D(|\nabla I_{1,\sigma}|, |\nabla I_{t,\sigma}|)$ . The subscripts  $I, G, GM$  denote the original image and response to the Gaussian and Gaussian magnitude filters respectively. Therefore dissimilarity between the two images at the location  $\mathbf{x}_i$  is defined by the dissimilarity vector  $\vec{D}_{1,t} = \{D_I, D_G, D_{GM}\}_{1,t}$ .

The dissimilarity measures from the first class assess the distance between the corresponding local histograms. The dissimilarity measures from the second class assess the change in the histogram characteristics. If two histograms differ, dissimilarity measures from the first class are strictly positive while the dissimilarity measures from the second class result in both positive and negative values. We are interested in local changes regardless of the sign therefore only the magnitude of the dissimilarity measures is considered. Finally, the measure of local changes  $p_{1,t}(\mathbf{x}_i)$  at the sample  $\mathbf{x}_i$  between the images  $I_1$  to  $I_t$  is computed as the L1-norm of the dissimilarity vector, as follow,  $p_{1,t}(\mathbf{x}_i) = \|\vec{D}_{1,t}\|_{L_1}$ .

## 7.3 Experiments

### 7.3.1 Data

We conducted experiments on subjects with Alpha 1-antitrypsin deficiency monitored during a period of 30 months. A total of 27 subjects were included into the experiments. For each subject low-dose CT images were acquired at five time points: at baseline, after 3, after 12, after 21, and after 24 or 30 months. Out of 27 subjects 11 were scanned after 24 months. The scans were acquired using a tube voltage of 140 kVp, exposure 40 mAs, in-plane resolution 0.78 mm and slice thickness 2 mm without overlap.

Lung function tests were acquired along with the CT scans, of which we used the forced expiratory volume in 1 second ( $FEV_1$ ). At baseline all the patients performed lung function tests and average  $FEV_1$  for all the subjects was  $1.54 \pm 0.68$  L, and TLC was  $8.02 \pm 1.57$  L, the ratio  $FEV_1/TLC$  was  $20.27 \pm 10.38$  %. For the last visit there are 2 missing lung function tests, and the average over the remaining 25 subjects is  $FEV_1$   $1.29 \pm 0.71$ L, TLC  $7.45 \pm 2.51$  and ratio  $FEV_1/TLC$   $17.93 \pm 9.04$  %.

### 7.3.2 Measuring Local Emphysema Progression

The four follow up CT scans  $I_2, I_3, I_4, I_5$  were first registered to the baseline image  $I_1$ . The segmented lung fields from the baseline image  $I_1$  were eroded with a cubic structuring element of size of  $3 \times 3 \times 3$  voxels and  $N_s = 2000$  positions were randomly sampled from the eroded lung fields. In our experiments we chose the Gaussian scale of the filters  $\sigma = 1$  voxel. The radius of the aperture function  $A$  was set to  $\alpha = 20$  voxels, and the weights were truncated at  $3\alpha$  radius. For the intensity-based histograms the bin width was set to 1 HU resulting in 1000 bins in total in the intensity range from  $-1000$  to 0 HU. For the histograms of the filtered images, the number of bins was set to 1000 and the bin edges were placed uniformly covering the full range of filter responses.

Within a 3 month period changes are expected to be relatively small, therefore the dissimilarities observed in this period reflects mostly image dissimilarity caused by misregistration and interpolation. From these pairs of images we obtained the mean and the standard deviation of the dissimilarity vector  $\vec{D}_{1,2}$ . Further we normalized all the dissimilarity vectors  $\vec{D}_{1,t=2,3,4,5}$  with respect to the obtained mean and standard deviation and then computed the corresponding progression measures  $p_{1,t=2,3,4,5}$ .

## 7.4 Results

Table 7.1 reports the summary of the conventional emphysema progression measurements, the decline in FEV<sub>1</sub> ( $\Delta\text{FEV}_1$  in L) and increase of relative area below the 950HU ( $\Delta\text{RA950}$  in [%]). The conventional measures were compared with the proposed feature-based disease progression measures. Disease progression measure (PM) on a subject level was computed as the average of dissimilarity measures for all spatial locations. We tested the complete set of dissimilarities (PM (all)); only Kullback-Leibler divergence between the local histograms of the smoothed images as the local dissimilarity measures (PM (KL)); and only local increase in RA950HU (PM (loc $\Delta\text{RA950}$ )). Table 7.1 presents the average disease progression measures for all consecutive follow up visits. A time trend analysis was performed for the disease progression measurements using a linear mixed model with the time between the baseline and a follow up visit as the fixed effect. For the FEV1 we did not conducted time trend analysis because 9 out of 27 subjects had missing FEV1 measurement at least at one of the visits. The t-values are reported in the Table 7.1. Additionally, correlation coefficients between the progression measured at the last visit assessed by either the proposed methods or by the conventional emphysema score or the lung function are presented in the Table 7.2.

Figure 7.1 shows samples locations, indicated with circles, overlaying on the 2D-slices extracted from the baseline and the registered follow up images. Radius

Table 7.1: Summary of the disease progression measures. Left part presents the average of the progression measures over all subjects for the follow up visits and the t-value of the time-trend analysis.

# mnths	Average Progression				Time-trend
	3	12	21	30(24)	t-value
$\Delta\text{FEV}_1$	-0.03	0.01	-0.01	-0.13	NA
$\Delta\text{RA950}$	-1.27	0.08	1.33	1.91	6.37
PM (all)	0.75	0.76	0.89	0.93	3.09
PM (KL)	0.25	0.27	0.30	0.31	7.80
PM (loc $\Delta\text{RA950}$ )	0.0	0.46	0.77	1.03	8.80

Table 7.2: The correlation coefficients between the progression measures obtained from the last visit with the corresponding p-values in brackets.

Average Progression at 30(24) months	Correlation coefficients	
	$\Delta\text{RA950}$	$\Delta\text{FEV}_1$
$\Delta\text{FEV}_1$		
$\Delta\text{RA950}$		-0.18(0.48)
PM (all)	0.51(0.007)	0.11(0.59)
PM (KL)	0.45(0.02)	-0.18(0.39)
PM (loc $\Delta\text{RA950}$ )	0.87(< 0.001)	0.11(0.59)

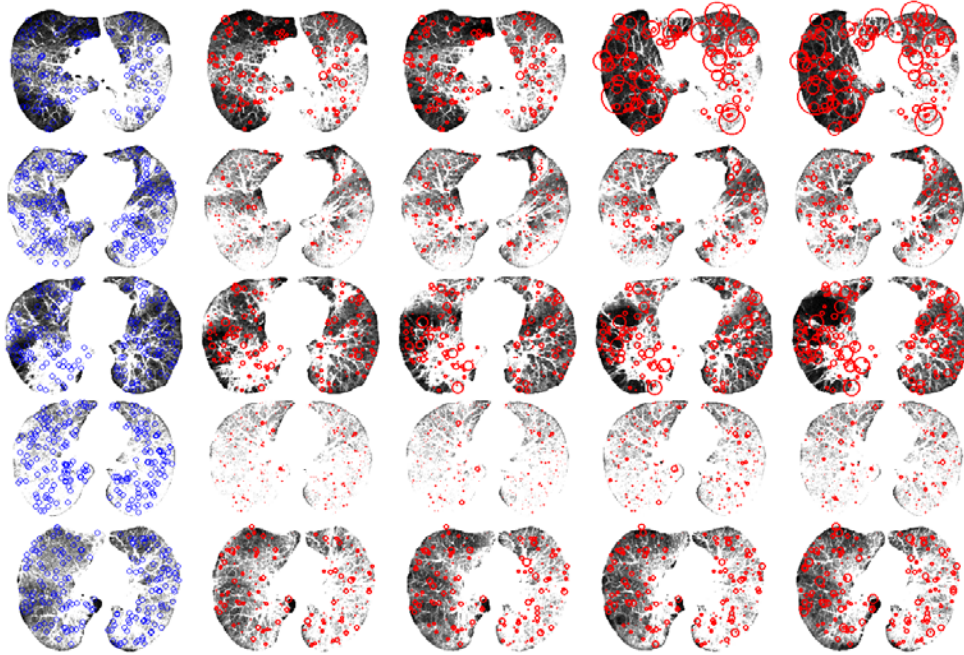
Table 7.3: Comparison of the local dissimilarity measures. Table presents the overall percentage of samples with dissimilarity measure above the threshold  $T$ ; in brackets the relative percentage of sampled which increased or preserved the dissimilarity measure above the threshold in all the successive follow up scans.

# mnths	Overall percentage [%] (confirmed [%])			
	3	12	21	30(24)
PM (all)	5.24(41.61)	5.68(61.48)	9.01(75.87)	10.49
PM (KL)	1.19(38.73)	1.75(56.07)	3.72(78.12)	4.93
PM (loc $\Delta\text{RA950}$ )	2.86(9.07)	4.38(33.94)	8.88(60.54)	11.48

of a circle in the follow up images is proportional to the dissimilarity measure computed from the complete set of dissimilarities. Each row displays different subject.

In order to investigate local consistency of the local disease progression measures, we tested the simple hypothesis that samples with dissimilarity measure above a threshold  $T$  at the previous follow up visit should not decrease the dissimilarity measure in the consecutive visits. The threshold on the dissimilarity measure was selected based on the 25th- and 75th- percentiles,  $p_{25}$  and  $p_{75}$ , of the dissimilarity measures after the 3 months follow up visit,  $T = p_{75} + 1.5(p_{75} - p_{25})$ , which corresponds to  $\sim 2.7$  standard deviations. The total number of samples with dissimilarity above the threshold  $T$  and the relative percentage of those sam-

Figure 7.1: Rows show mean intensity projection over a stack of 9 sequential slices, selected from different volumetric images. The left most column shows slices extracted from the baseline image, the remaining columns show corresponding slices extracted from the registered 3, 12, 21 and 30(24) months follow up visits, respectively from left to right. All the slices are displayed in the intensity range  $[-1000,-900]$ HU. Locations of the random samples (blue and red markers) in the corresponding stack were projected to the image slice. In the follow up images the marker size is proportional to the local dissimilarity measure obtained from the complete set of dissimilarities.



ples that increase or preserve the same dissimilarity measure in all the successive visits is reported in the Table 7.3.

Examples of the samples with disease progression measure above the threshold  $T$  are presented in the Figure 7.2. Plot in Figure 7.2a displays a subject where most of the samples with the large dissimilarity measure after 3 months were confirmed with all the consecutive follow up scans. Plot in Figure 7.2b displays a subject where the samples did not show consistent dissimilarity measure over time.

## 7.5 Discussion

In this chapter we presented a framework for detection of local emphysema progression. The overall disease progression measure showed significant correla-

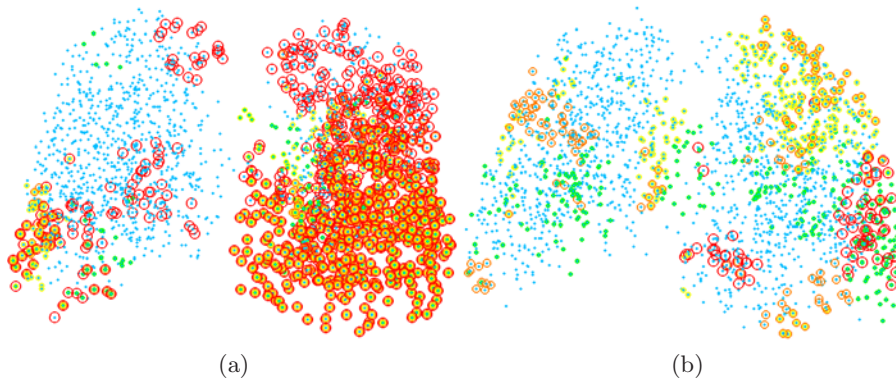


Figure 7.2: All selected random samples marked in blue color. Locations with the significantly large dissimilarity measure obtained from the complete set of features at the 3, 12, 21, 30(24) months follow up visits are indicated in green, yellow, orange and red markers respectively.

tion ( $p < 0.01$ ) with increase in the standard CT score, the relative area below  $-950\text{HU}$ , between the baseline and the last follow up visit. The correlation with the decline in  $\text{FEV}_1$  was not significant for neither the proposed measures nor for the standard CT score. In our dataset the average  $\text{FEV}_1$  at baseline was very low, indicating the severity of emphysema already at the baseline visit. This can explain the lack of sensitivity to disease progression of the  $\text{FEV}_1$  measurement.

We analyzed time trend based on the conventional emphysema measurements and the proposed dissimilarity-based measurements. The time trend was approximately equally significant for the conventional RA950 disease progression measure, local increase in RA950 and the measure derived from the Kullback-Leibler divergence between local histograms of the smoothed images. The time trend was less significant for the measurement obtained from the complete set of dissimilarities. One of the possible explanations could be sensitivity of the particular dissimilarity measure to the change in image appearance not related to the emphysema progression, for example inflammation or change in local topology like collapsing or appearing bullae. Another possible explanation could be in the construction of the overall combined disease progression score from the complete vector of dissimilarities.

The current drawback of the proposed method is the simplification of the complete dissimilarity vector by its norm. The emphysema is usually characterized by the destruction of the lung tissue thus decreasing image intensities, while inflammation should result in increase of image intensities. In the current framework the two phenomena could result in equal dissimilarity measures. The specific dissimilarity measures such as difference in means of the local histograms is capable of differentiating between the two processes, therefore a careful investigation of the dissimilarity measures should be done. Furthermore an automatic

classification approach could be adapted for this problem, where samples from the image pairs with the 3 months follow up scan represent stable group while samples from the image pairs with the 30(24) months follow up scan represents the progressed group.

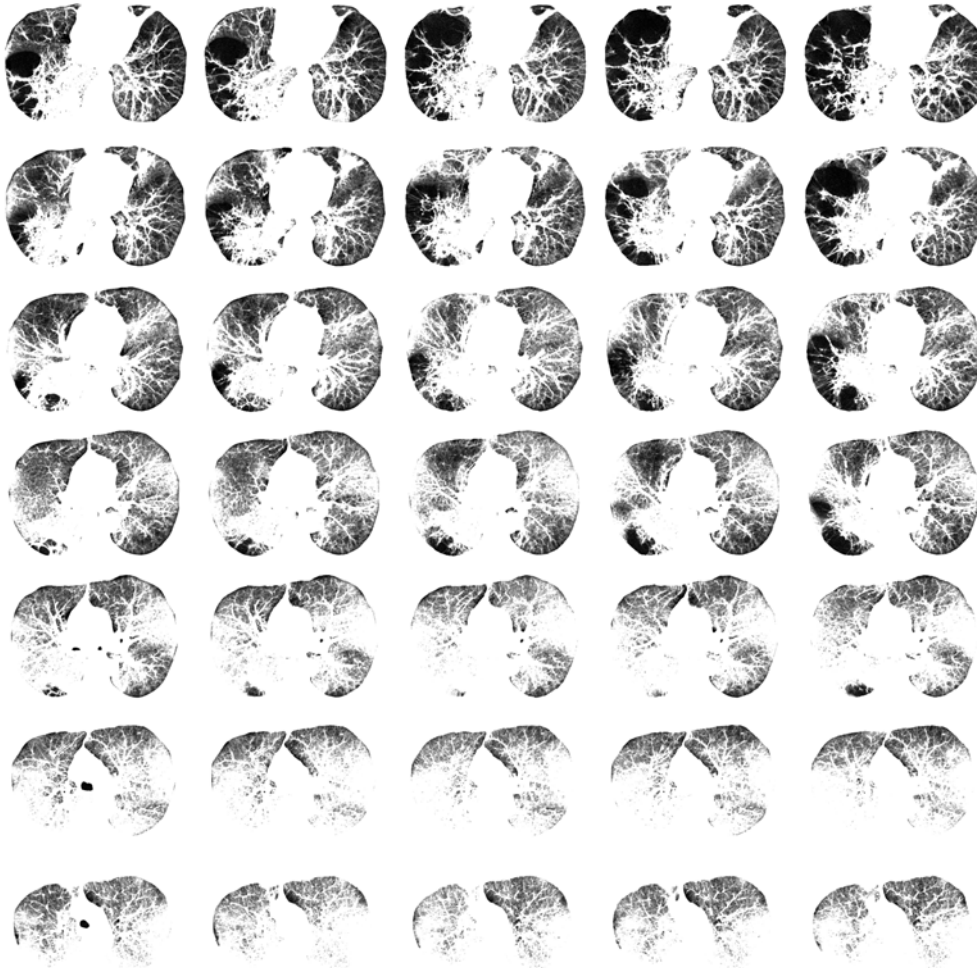
To conclude, we proposed a method for estimating local disease progression. Results suggested that emphysema progression can be detected before the tissue intensity decreases below the standard CT threshold of -950HU.

## 7.6 Appendix

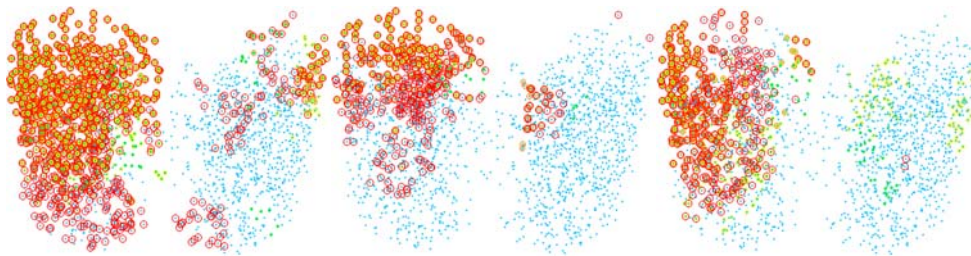
This section presents four interesting cases in our dataset. For each case the figure displays snap shots of the baseline and the deformed follow up images and the table presets lung function test (FEV1), global emphysema index (RA950), and averaged local dissimilarity measures computed from the complete set of features (PM (all)); from Kullback-Leibler divergence of the smoothed image histograms (PM (KL)); and local emphysema index, (PM (loc $\Delta$ RA950)).

Each row in the top figure shows mean intensity projection over a stack of 9 sequential slices, uniformly sampled from the volumetric image. The left most column shows slices extracted from the baseline image, the remaining columns show corresponding slices extracted from the registered 3, 12, 21 and 30(24) months follow up visits, respectively from left to right. All the slices are displayed in the intensity range [-1000,-900]HU. In the bottom part of the figure, three plots show locations of all random samples (blue color) and locations that were marked as outliers based on the progression measure computed from the complete set of features (the left plot); from the Kullback-Leibler divergence of the smoothed image histograms (the middle plot); and from the local area below -950HU (the right plot). Locations marked as outliers in the 3, 12, 21 and 30(24) months follow ups are indicated in green, yellow, orange and red colors respectively.

Case A		3mnths	12mnths	21mnths	30(24)mnths	
RA950		44.15	42.60	40.96	45.13	46.22
FEV1		1.41	1.50	1.57	1.44	1.36
PM (all)		0.96	1.10	1.13	1.13	1.47
PM (KL)		0.70	0.78	0.93	0.93	1.16
PM (loc $\Delta$ RA950)		-0.18	-0.62	0.45	0.45	0.91



(a)



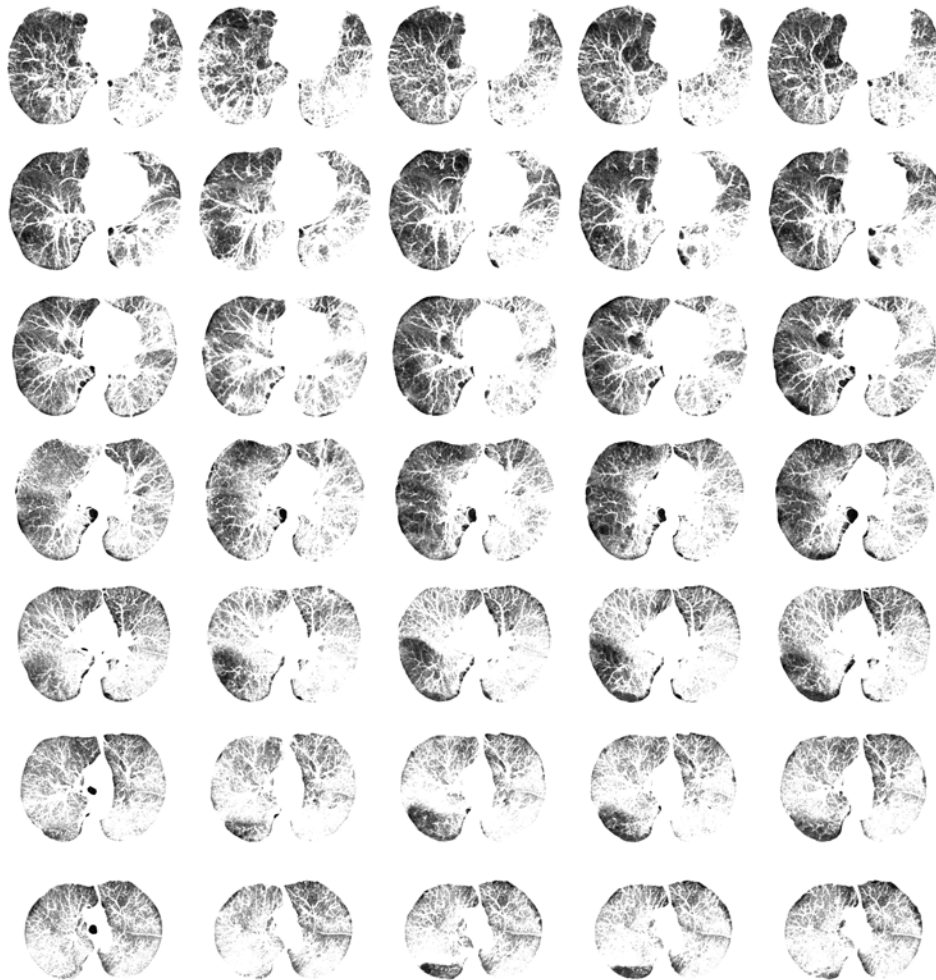
(b)

(c)

(d)



Case B		3mnts	12mnts	21mnts	30(24)mnts
RA950	40.52	34.24	36.80	37.90	43.69
FEV1	1.51	1.43	1.38	1.36	1.13
PM (all)		0.99	0.97	0.95	0.77
PM (KL)		0.67	0.75	0.82	0.89
PM (loc $\Delta$ RA950)		-1.18	-0.38	-0.27	0.43



(a)

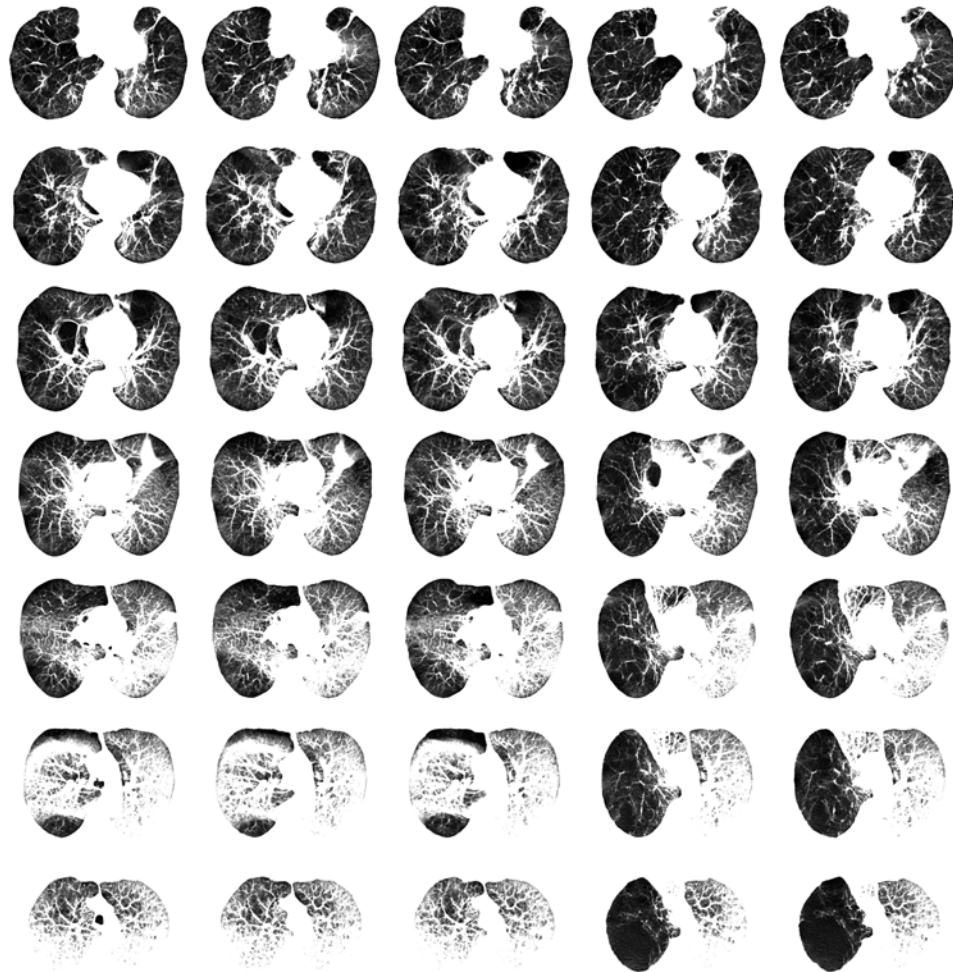


(b)

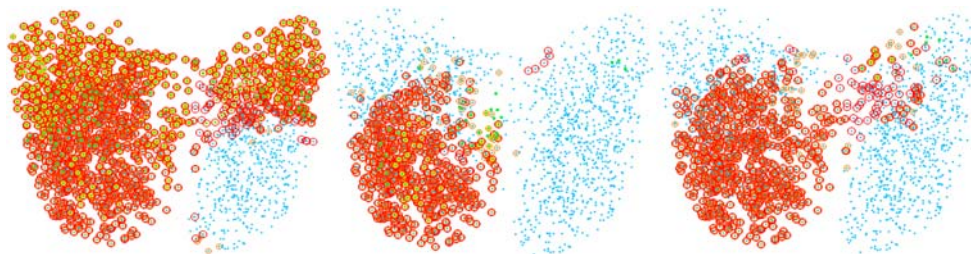
(c)

(d)

Case C		3mnths	12mnths	21mnths	30(24)mnths
RA950	62.00	59.82	61.57	70.50	69.94
FEV1	1.08	1.03	1.06	NA	NA
PM (all)		1.08	1.09	3.47	3.49
PM (KL)		0.84	0.92	1.60	1.64
PM (loc $\Delta$ RA950)		-0.04	0.40	2.73	2.95



(a)

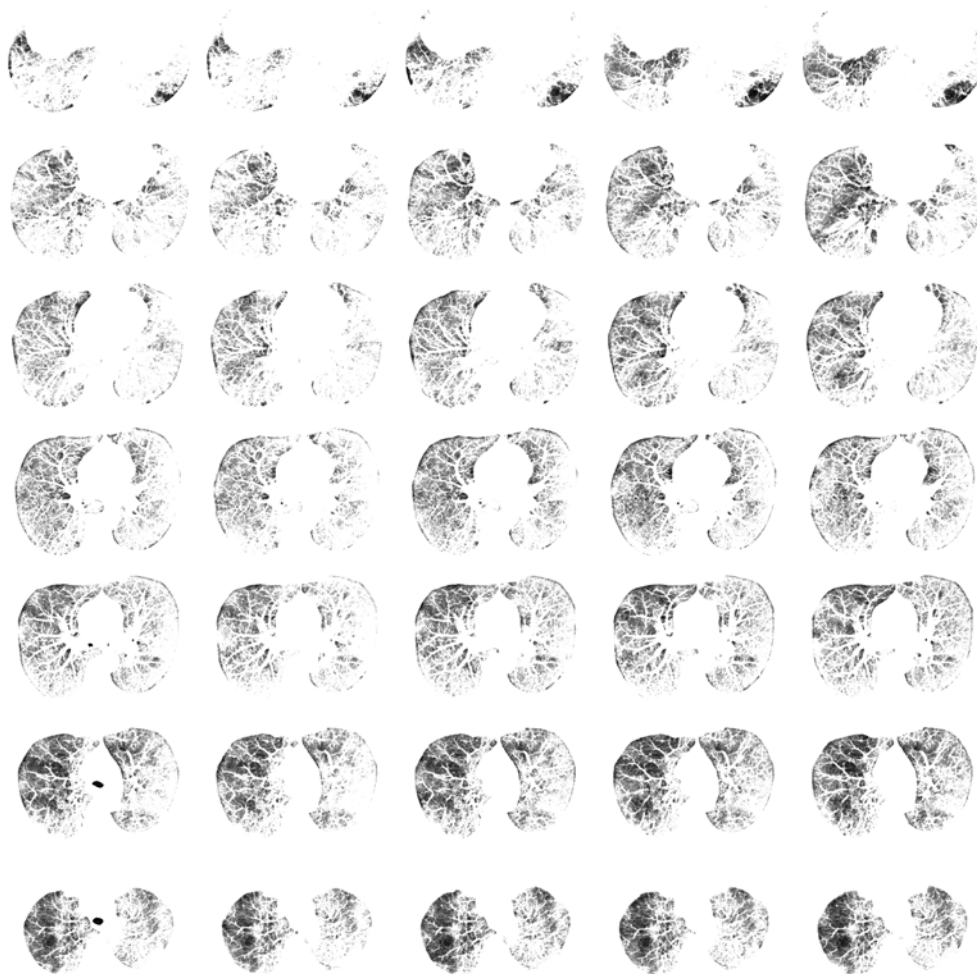


(b)

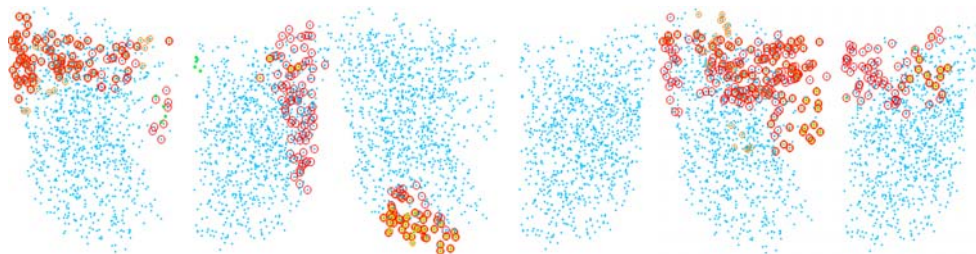
(c)

(d)

Case D		3mnts	12mnts	21mnts	30(24)mnts
RA950	28.33	24.46	30.30	30.92	31.29
FEV1	2.64	2.64	2.57	2.48	2.40
PM (all)		0.78	0.68	0.79	0.86
PM (KL)		0.46	0.60	0.61	0.66
PM (loc $\Delta$ RA950)		-0.73	1.04	1.16	1.42



(a)



(b)

(c)

(d)



## Chapter 8

---

# Summary and Discussion

---

*Science is always wrong. It never solves a problem without creating ten more.*

— GEORGE BERNARD SHAW

In this thesis, the problem of image registration for monitoring disease progression was investigated. Provided the point correspondence between the two longitudinal CT lung scans, the changes between the scans is revealed in the difference image. Image registration is a powerful tool and capable of establishing point correspondence with an accuracy of just 1 voxel. For monitoring disease progression such an accurate registration could be unfavourable, because then the deformed image will appear exactly the same as the fixed image and the difference between the two will be completely eliminated. An example illustrating the performance of the registration method was presented in the Chapter 1, where bulla expanded over the time and bullas borders was not matched. The change in bulla size was apparent in the difference image.

We started with a conventional image registration method, where multi-level B-Spline transform function and sum of squared differences dissimilarity function were used. The size of the B-Spline grids were conditioned upon the scale of lung lobes, segments and sub-segments. Human lungs contains 5 lobes and 18 lung segments. With an average lung volume of 5 liters, the linear scale of a lung lobe is approximately 10 cm and the linear scale of a lung segment is approximately 6.5 cm. We wanted to establish an accurate correspondence but not to overfit the images and eliminate the difference between the two images, thus size of the smallest B-Spline grid was about 2.5 cm. Whereas size of the smallest B-Spline

grid in our registration algorithm was generally larger than the size used in other B-Spline-based registration algorithms, the accuracy of the proposed registration method was comparable with the existing registration algorithms. Authors in [38, 50, 109] reported the size of the smallest B-Spline grid of approximately 8 voxels; K. Murphy et al. [78] reported 10 mm; Z. Wu et al. [48] reported the size of 50 mm.

Registration of lung CT scans is a complex problem, because lung appearance significantly depends on the inspiration level. Although subjects in this study were scanned at the maximum inspiration level, the variation in lung volume between the longitudinal scans was up to one liter leading to the complex and non-homogeneous deformations of lungs. Additional inspiration resulted in lower intensities of lung parenchyma in CT scans. This could be confused with the emphysema progression since emphysema is a destruction of lung tissue and also results in intensity decrease of lung parenchyma. The change in inspiration affects all the conventional densitometric measurements, e.g., relative area below 950HU, 15th percentile density and average lung density thus making it unreliable measures of emphysema progression. We proposed a novel solution - the mass preserving model of lungs, where lung density is inversely proportional to the local volume change in lungs. This model allows to compensate the regional change in intensity related to the regional change in the inspiration level. In Chapter 2 we investigated the mass preserving model and showed that incorporation mass preserving model directly into the image registration improves registration accuracy. Recently, the mass preserving model of lungs was also studied by other research groups and also showed better registration accuracy and more feasible deformations of lungs [38, 116, 56, 107]. The recent study [107] showed correlation of 0.9 between the lung ventilation estimated from the Xe-CT images and estimated from the mass preserving image registration. The mass preserving model was successfully applied in pilot experiments on monitoring emphysema progression presented in the Chapter 6 and in [31].

After spending numerous hours looking at the registration results, I was convinced that intensity-based registration could not register peripheral area accurately. Therefore we developed a feature-based algorithm dedicated to match vessels centerlines in Chapter 3. The algorithm was based on the existing current-based registration where no point correspondence was required. Question of how to combine information from the current-based registration in Chapter 3 and the intensity-based registration in Chapter 2 was addressed in Chapter 4. We proposed a novel registration method, where intensity-based registration was constrained with the deformations of the vessel centerlines obtained from the current-based registration. The important result was that by incorporating information from the feature-based registration into the intensity-based registration we were able to improve the accuracy of the registration using the same transformation

model. The recent study [107] showed that incorporating dissimilarity between vesselness filter responses along with the dissimilarity between the original images significantly improves registration accuracy. The downside of the proposed approach was its computational complexity. Therefore we returned to the image registration method from Chapter 2 in the following experiments.

Finally, we revisited the emphysema progression problem and this time we developed a framework which compensates for small mis-registrations. Alignment of longitudinal images was a first step towards analysis of regional emphysema progression. Although image registration provides point-to-point correspondence with accuracy of few millimeters, the direct point-to-point comparison of lung CT images has critical drawbacks. First, intensity of lung CT image only partially related to the true density of the tissue, because of the noise and partial volume effect. Secondly, different regions in lungs are registered with different accuracy, therefore in regions with lower registration accuracy direct point-to-point comparison is affected more by mis-registrations. Instead of the direct point-to-point comparison of image intensities, we proposed to adapt the concept of locally orderless images. Local image histograms at the corresponding locations in the baseline and deformed follow up images were compared by means of several dissimilarity measures. Along with the original images, we computed local histograms from the filtered versions of the images, e.g., gaussian blur and gradient magnitude filters. Dissimilarity measures included both distance measure between histograms and differences in individual measurements, e.g., moments of histograms. This framework is both robust to noise presented in the images and to small mis-registrations. Experiments showed promising results however more detailed investigation should be performed.

To conclude, four main contributions were made in this thesis:

- mass preserving registration was proposed and justified on a large amount of data;
- current-based registration framework was adapted for registering lung CT scans;
- combined feature-based and intensity-based registration method was proposed and validated via manually annotated landmarks;
- framework for monitoring emphysema progression was developed and tested on patients with Alpha-1 Antitrypsin Deficiency.

## 8.1 Discussion

The proposed mass preserving model is a simple model, where density of lung tissue is assumed to be inverse proportionally to the volume. With the mass

preserving model, intensities are linearly transformed with the fixed point at the intensity of air, -1000HU. Generally, if we observe uniform expansion of lungs, we believe that for lung parenchyma mass preservation is correct, but for expanding vessel the mass preservation is not applicable. If a vessel expands/contracts intensity or density should remain constant. This leads to a second fixed point in the intensity adjustment model at 0 HU. Since there is no linear intensity adjustment model with two fixed points, e.g., at the value -1000HU and 0HU, the intensity adjustment should be applied locally only for voxels from lung parenchyma.

If an image registration algorithm provides feasible deformations of lungs caused by additional inspiration, the mass preserving model will then compensate lung tissue density change imposed by the deformations. The physiologically correct and plausible deformations are critical issues for the mass preserving lung model. Recent study by Kabus S. et al. [24], compared deformation fields of several registration algorithms. Even with comparable registration accuracy, different algorithms resulted in significantly different deformation fields. Therefore a thorough inspection of the deformation field is needed before applying mass preserving intensity correction.

Another question that should be investigated is the range of lung volume changes where mass preservation holds. For example, during tidal breathing the range of possible lung volumes is significantly smaller than variations in lung volume from maximum expiration to maximum inspiration. In those extreme cases preservation of lung mass may not hold. Another case when inflammation is observed only in one of the scans, the mass preserving model of lungs does not hold. In those cases a more advanced model of lungs should be developed.

An interesting research topic addressed in this thesis was the problem of monitoring disease progression. With the proposed local image comparison framework several questions could be further investigated, e.g., how the emphysema progression in a region affects the surrounding regions and how we could predict disease development.

An interesting question that could be investigated in the future, is local analysis of deformation fields. Assuming that registration provides physiologically correct deformations of lungs, one could investigate if there is a difference in the deformations of healthy and diseased tissues. Since emphysema is characterized by decrease of lung tissue elasticity this phenomena may be reflected in the deformation fields.

Several research questions emerged along the past three years were not investigated in the thesis. With the rapidly increasing number of longitudinal lung CT studies and many research groups working on the topic, those questions definitely will be solved in foreseeable future.



---

# List Of Publications

---

## Papers in peer-reviewed conferences

- Gorbunova V., Lo P., Ashraf H., Dirksen A., Nielsen M., de Bruijne M., "Weight Preserving Image Registration for Monitoring Disease Progression in Lung CT" in *Medical Image Computing and Computer Assisted Intervention Conference*, 2008.
- Gorbunova V., Lo P., Loeve M., Tiddens H., Sporning J., Nielsen M., de Bruijne M., "Mass Preserving Registration for Lung CT" in *SPIE Medical Imaging*, 2009.
- Gorbunova V., Durrleman S., Lo P., Pennec X., de Bruijne M., "Lung CT Registration Combining Intensity, Curves and Surfaces" in *IEEE International Symposium on Biomedical Imaging*, 2010.
- Gorbunova V., Jacobs S.A.M., Lo P., Dirksen A., Nielsen M., Bab-Hadiashar A., de Bruijne M., "Early Detection of Emphysema Progression" to appear in *Medical Image Computing and Computer Assisted Intervention Conference*, 2010.

## Papers in peer-reviewed workshops

- Gorbunova V., Durrleman S., Lo P., Pennec X., de Bruijne M., "Curve- and Surface-based registration of lung CT images via currents" in *Second International Workshop on Pulmonary Image Analysis*, 2009.
- Gorbunova V., Sporning J., Lo P., Dirksen A., de Bruijne M., "Mass Preserving Registration for lung CT: EMPIRE10 Challenge Results" to appear in *Grand Challenges in Medical Image Analysis Workshop*, 2010.



---

# Bibliography

---

- [1] Wilhelm Conrad Röntgen. Über eine neue art von strahlen. *Aus den Sitzungberichten der Würzburger Physik.-medic. Gesellschaft*, 1895. [cited at p. 3]
- [2] R Green. Fleischner Lecture. Imaging the respiratory system in the first few years after discovery of the X-ray: contributions of Francis H. Williams, M.D. *American Journal of Roentgenology*, 159:1–7, 1992. [cited at p. 4]
- [3] A Vallebona. Radiography with great enlargement (micro-radiography) and a technical method for the radiographic dissociation of the shadow. *Radiology*, 17:340–341, 1931. [cited at p. 4]
- [4] G N Hounsfield. Computerized transverse axial scanning (tomography): Part1. description of system. *British Journal of Radiology*, 46:1016–1022, 1973. [cited at p. 4]
- [5] K.F. Rabe et al. Global strategy for the diagnosis, management, and prevention of chronic obstructive pulmonary disease gold executive summary. *American Journal of Respiratory and Critical Care Medicine*, 176:532–555, 2007. [cited at p. 7, 24, 73, 76, 81]
- [6] World health statistics. Technical report, 2008. [cited at p. 7]
- [7] A Dirksen, F Rasmussen, and N Keiding. Choice of measurement and sample size for detection of changes in lung function in obstructive pulmonary disease. *European Respiratory Review*, 5:432–435, 1991. [cited at p. 7]
- [8] Asger Dirksen, NH Holstein-Rathlou, F Madsen, LT Skovgaard, CS Ulrik, T Heckscher, and A Kok-Jensen. Long-range correlations of serial FEV<sub>1</sub> measurements in emphysematous patients and normal subjects. *The American Physiological Society*, 85:259–265, 1998. [cited at p. 7]

- [9] JW Gurney, KK Jones, RA Robbins, GL Gossman, KJ Nelson, D Daughton, JR Spurzem, and SI Rennard. Regional distribution of emphysema: correlation of high-resolution ct with pulmonary function tests in unselected smokers. *Radiology*, 183:182–185, 1992. [cited at p. 7]
- [10] JS Klein, G Gamsu, WR Webb, JA Golden, and NL Muller. High-resolution ct diagnosis of emphysema in symptomatic patients with normal chest radiographs and isolated low diffusing capacity. *Radiology*, 182:817–821, 1992. [cited at p. 7]
- [11] Naidich D.P Webb R.W., Muller N. L. *High-Resolution CT of the Lung*. Lippincott Williams and Wilkins, 2001. [cited at p. 7]
- [12] M. Els Bakker, Hein Putter, Jan Stolk, Saher B Shaker, Eeva Piitulainen, Erich W Russi, and Berend C Stoel. Assessment of regional progression of pulmonary emphysema with CT densitometry. *CHEST*, 134(5):931–937, Nov 2008. [cited at p. 7, 8]
- [13] E. A. Hoffman, J. M. Reinhardt, M. Sonka, B. A. Simon, J. Guo, O. Saba, D. Chon, S. Samrah, H. Shikata, J. Tschirren, K. Palagyi, K. C. Beck, and G. McLennan. Characterization of the Interstitial Lung Diseases via Density-Based and Texture-Based Analysis of Computed Tomography Images of Lung Structure and Function. *Academic Radiology*, 10(10):1104–1118, 2003. [cited at p. 7]
- [14] J Stolk et al. Progression parameters for emphysema: a clinical investigation. *Respiratory Medicine*, 101(9):1924–30, 2007. [cited at p. 7, 78]
- [15] J Zaporozhan et al. Paired inspiratory/expiratory volumetric thin-slice CT scan for emphysema analysis: Comparison of different quantitative evaluations and pulmonary function test. *CHEST*, 128:3212–3220, 2005. [cited at p. 7]
- [16] A. Dirksen, E. Piitulainen, D.G. Parr, C. Deng, M. Wencker, and S.B. Shakerand R.A. Stockley. Exploring the role of CT densitometry: a randomised study of augmented therapy in  $\alpha_1$ -antitrypsin deficiency. *European Respiratory Journal*, 33:1345–1353, 2009. [cited at p. 7, 8, 16, 81, 82]
- [17] H.A. Gietema, A.M. Schilham, B. van Ginneken, R.J. van Klaveren, J.W.J. Lammers, and M. Prokop. Monitoring of smoking-induced emphysema with CT in a lung cancer screening setting: Detection of real increase in extent of emphysema. *Radiology*, 244, 3:890–897, 2007. [cited at p. 7, 74, 81]
- [18] David G Parr, Martin Sevenoaks, Chunqin Deng, Berend C Stoel, and Robert A Stockley. Detection of emphysema progression in alpha 1-

- antitrypsin deficiency using CT densitometry; methodological advances. *Respiratory Research*, 9:21, 2008. [cited at p. 7]
- [19] E.M. van Rikxoort, M. Prokop, B. de Hoop, M.A. Viergever, J.P.W. Pluim, and B. van Ginneken. Automatic segmentation of the pulmonary lobes from fissures, airways, and lung borders: evaluation of robustness against missing data. *Proc. Medical Image Computing and Computer Assisted Intervention (MICCAI)*, 5761:263–271, 2009. [cited at p. 8]
- [20] Li Zhang, Eric A Hoffman, and Joseph M Reinhardt. Atlas-driven lung lobe segmentation in volumetric X-ray CT images. *IEEE Transactions on Medical Imaging*, 25(1):1–16, 2006. [cited at p. 8, 18]
- [21] Jan-Martin Kuhnigk, Volker Dicken, Stephan Zidowitz, Lars Bornemann, Bernd Kuemmerlen, Stefan Krass, Heinz-Otto Peitgen, Silja Yuval, Hans-Holger Jend, Wigbert S. Rau, and Tobias Achenbach. New Tools for Computer Assistance in Thoracic CT. Part 1. Functional Analysis of Lungs, Lung Lobes, and Bronchopulmonary Segments. *Radiographics*, 25:525–536, 2005. [cited at p. 8]
- [22] E.M. van Rikxoort, B. de Hoop, S. van de Vorst, M. Prokop, and B. van Ginneken. Automatic segmentation of pulmonary segments from volumetric chest CT scans. *IEEE Transactions on Medical Imaging*, 28(4):621–630, 2009. [cited at p. 8]
- [23] K. Murphy, B. van Ginneken, J.P.W. Pluim, S. Klein, and M. Staring. Semi-automatic reference standard construction for quantitative evaluation of lung CT registration. In Dimitris Metaxas, Leon Axel, Gábor Székely, and Gabor Fichtinger, editors, *Proc. Medical Image Computing and Computer Assisted Intervention (MICCAI)*, volume 5242 of *Lecture Notes in Computer Science*, pages 1006–1013, 2008. [cited at p. 8, 13, 14, 20, 33, 65]
- [24] Sven Kabus, Tobias Klinder, Keelin Murphy, Bram van Ginneken, Cristian Lorenz, and Josien P. W. Pluim. Evaluation of 4D-CT lung registration. In Guang-Zhong Yang, David J. Hawkes, Daniel Rueckert, J. Alison Noble, and Chris J. Taylor 0002, editors, *Proc. Medical Image Computing and Computer Assisted Intervention (MICCAI)*, volume 5761 of *Lecture Notes in Computer Science*, pages 747–754. Springer, 2009. [cited at p. 8, 48, 98]
- [25] Margrit Betke, Harrison Hong, Deborah Thomas, Chekema Prince, and Jane P Ko. Landmark detection in the chest and registration of lung surfaces with an application to nodule registration. *Medical Image Analysis*, 7(3):265–281, 2003. [cited at p. 9, 13, 33, 38, 48]

- [26] Helen Hong, Jeongjin Lee, and Yeny Yim. Automatic lung nodule matching on sequential CT images. *Computers in Biology and Medicine*, 38(5):623–634, 2008. [cited at p. 9, 18]
- [27] Yuanjie Zheng, K. Steiner, T. Bauer, Jingyi Yu, Dinggang Shen, and C. Kambhamettu. Lung nodule growth analysis from 3D CT data with a coupled segmentation and registration framework. In *MMBIA Workshop at IEEE 11th International Conference on Computer Vision*, pages 1–8, Oct 2007. [cited at p. 9, 18]
- [28] Y. Arzhaeva, M. Prokop, K. Murphy, E.M. van Rikxoort, P.A. de Jong, H.A. Gietema, M.A. Viergever, and B. van Ginneken. Automated estimation of progression of interstitial lung disease in CT images. *Medical Physics*, 37(1):63–73, 2010. [cited at p. 9, 48]
- [29] Vladlena Gorbunova, Pechin Lo, Haseem Ashraf, Asger Dirksen, Mads Nielsen, and Marleen de Bruijne. Weight preserving image registration for monitoring disease progression in lung CT. In Dimitris Metaxas, Leon Axel, Gábor Székely, and Gabor Fichtinger, editors, *Proc. Medical Image Computing and Computer Assisted Intervention (MICCAI)*, volume 5242 of *Lecture Notes in Computer Science*, pages 863–870, 2008. [cited at p. 10, 14, 18, 19, 31, 42, 48, 82]
- [30] Vladlena Gorbunova, Sanders S.A.M. Jacobs, Lo Pechin, Asger Dirksen, Mads Nielsen, Alireza Bab-Hadiashar, and Marleen de Bruijne. Early detection of emphysema progresison. In *Proc. Medical Image Computing and Computer Assisted Intervention (MICCAI)*, Lecture Notes in Computer Science, 2010. [cited at p. 10]
- [31] Marius Staring, M.E. Bakker, D.P. Shamonin, J. Stolk, J.H.C. Reiber, and B.C. Stoel. Towards local estimation of emphysema progression using image registration. In J.P.W. Pluim and B.M. Dawant, editors, *SPIE (Medical Imaging)*, volume 7259 of *Proceedings of SPIE*, Feb 2009. [cited at p. 10, 18, 31, 82, 96]
- [32] Jan Modersitzki. *Numerical Methods for Image Registration*. Oxford University Press, 2004. [cited at p. 10, 11]
- [33] Milan Sonka and J. Michael Fitzpatrick. *Handbook of Medical Imaging*, volume 20. 2001. [cited at p. 10]
- [34] Vlad Boldea, David Sarrut, and S. C. Lung. Lung Deformation Estimation with Non-Rigid Registration for Radiotherapy Treatment. In *Proc. Medical Image Computing and Computer Assisted Intervention (MICCAI)*, volume

- 2878 of *Lecture Notes in Computer Science*, pages 770–777. Springer Verlag, R.E. Ellis and T.M. Peters, 2003. MICCAI 2003. [cited at p. 11]
- [35] K. Ding, J.E. Bayouth, J.M. Buatti, G.E. Christensen, and J.M. Reinhardt. 4D CT-based measurement of changes in pulmonary function following a course of radiation therapy. *Medical Physics*, 37(3):1261–72, 2010. [cited at p. 11, 18]
- [36] D Mattes, D Haynor, H Vesselle, T Lewellen, and W Eubank. PET-CT image registration in the chest using free-form deformations. *IEEE Transactions on Medical Imaging*, 22:120–128, 2003. [cited at p. 11, 14, 19, 48, 76]
- [37] Torbjorn Vik, Sven Kabus, Jens von Berg, Konstantin Ens, Sebastian Dries, Tobias Klinder, and Cristian Lorenz. Validation and comparison of registration methods for free-breathing 4D lung-CT. In J. M. Reinhardt and J. P. W. Pluim, editors, *SPIE (Medical Imaging)*, volume 6914, 2008. [cited at p. 11, 14, 32, 38, 48]
- [38] Youbing Yin, Eric A. Hoffman, and Ching-Long Lin. Mass preserving non-rigid registration of CT lung images using cubic B-spline. *Medical Physics*, 36(9):4213–4222, 2009. [cited at p. 11, 14, 19, 32, 96]
- [39] Richard Castillo, Edward Castillo, Rudy Guerra, Valen E Johnson, Travis McPhail, Amit K Garg, and Thomas Guerrero. A framework for evaluation of deformable image registration spatial accuracy using large landmark point sets. *Physics in Medicine and Biology*, 54(7):1849–1870, 2009. [cited at p. 11, 13, 16, 26, 27, 32, 41, 42, 48, 49, 53, 56]
- [40] Baojun Li, Gary E. Christensen, Eric A. Hoffman, Geoffrey McLennan, and Joseph M. Reinhardt. Pulmonary CT image registration and warping for tracking tissue deformation during the respiratory cycle through 3D consistent image registration. *Medical Physics*, 35(12):5575–5583, 2008. [cited at p. 11]
- [41] Deshan Yang, Wei Lu, Daniel A. Low, Joseph O. Deasy, Andrew J. Hope, and Issam El Naqa. 4D-CT motion estimation using deformable image registration and 5D respiratory motion modeling. *Medical Physics*, 35(10):4577–4590, 2008. [cited at p. 11]
- [42] Thomas Guerrero, Kevin Sanders, Edward Castillo, Yin Zhang, Luc Bidaut, Tinsu Pan, and Ritsuko Komaki. Dynamic ventilation imaging from four-dimensional computed tomography. *Physics in Medicine and Biology*, 51(4):777–791, Feb 2006. [cited at p. 11, 18]
- [43] J B A Maintz and M Z Viergever. A survey of medical image registration. *Medical Image Analysis*, 2:1–37, 1998. [cited at p. 13]

- [44] K. Rohr, H. S. Stiehl, R. Sprenkel, T. M. Buzug, J. Weese, and M. H. Kuhn. Landmark-based elastic registration using approximating thin-plate splines. *IEEE Transactions on Medical Imaging*, 20(6):526–534, 2001. [cited at p. 14, 38, 48]
- [45] Sven Kabus, Jens von Berg, Tokihiro Yamamoto, Roland Opfer, and Paul J. Keall. Lung ventilation estimation based on 4D-CT imaging. In M. Brown, M. de Bruijne, B. van Ginneken, A. Kiraly, J.M. Kuhnigk, C. Lorenz, K. Mori, and J. Reinhardt, editors, *First International Workshop on Pulmonary Image Analysis*, pages 73–83, 2008. [cited at p. 14, 18]
- [46] Vladlena Gorbunova, Stanley Durrleman, Pechin Lo, Xavier Pennec, and M de Bruijne. Curve- and surface-based registration of lung CT images via currents. In *Second International Workshop on Pulmonary Image Analysis*, 2009. [cited at p. 14, 48, 50]
- [47] M. Hub, M. L. Kessler, and C. P. Karger. A stochastic approach to estimate the uncertainty involved in b-spline image registration. *IEEE Transactions on Medical Imaging*, 28:1708 – 1716, 2009. [cited at p. 14, 21, 58]
- [48] Ziji Wu, Eike Rietzel, Vlad Boldea, David Sarrut, and Gregory C Sharp. Evaluation of deformable registration of patient lung 4DCT with sub-anatomical region segmentations. *Medical Physics*, 35(2):775–781, Feb 2008. [cited at p. 14, 18, 20, 32, 48, 96]
- [49] Vlad Boldea, Gregory C Sharp, Steve B Jiang, and David Sarrut. 4D-CT lung motion estimation with deformable registration: quantification of motion nonlinearity and hysteresis. *Medical Physics*, 35(3):1008–1018, Mar 2008. [cited at p. 14, 18]
- [50] Marius Staring, Stefan Klein, and Josien P.W. Pluim. A rigidity penalty term for nonrigid registration. *Medical Physics*, 34(11):4098 – 4108, Nov 2007. [cited at p. 14, 18, 96]
- [51] Stefan Klein, Marius Staring, and Josien P W Pluim. Evaluation of optimization methods for nonrigid medical image registration using mutual information and B-splines. *IEEE Transactions on Image Processing*, 16(12):2879–2890, Dec 2007. [cited at p. 14, 21, 23, 55]
- [52] Joseph M Reinhardt, Kai Ding, Kunlin Cao, Gary E Christensen, Eric A Hoffman, and Shalmali V Bodas. Registration-based estimates of local lung tissue expansion compared to xenon CT measures of specific ventilation. *Medical Image Analysis*, 12(6):752–763, Dec 2008. [cited at p. 14, 18, 19, 48]
- [53] Gary E. Christensen, Joo Hyun Song, Wei Lu, Issam El Naqa, and Daniel A. Low. Tracking lung tissue motion and expansion/compression with inverse



- consistent image registration and spirometry. *Medical Physics*, 34(6):2155–2164, 2007. [cited at p. 14, 18, 47, 48, 74]
- [54] Hiroaki Arakawa, Pierre Alain Gevenois, Yoshiaki Saito, Hisao Shida, Viviane De Maertelaer, Hiroshi Morikubo, and Mutsuhisa Fujioka. Silicosis: expiratory thin-section CT assessment of airway obstruction. *Radiology*, 236(3):1059–1066, Sep 2005. [cited at p. 14]
- [55] Thomas Guerrero, Geoffrey Zhang, William Segars, Tzeng-Chi Huang, Stephen Bilton, Geoffrey Ibbott, Lei Dong, Kenneth Forster, and Kang Ping Lin. Elastic image mapping for 4-D dose estimation in thoracic radiotherapy. *Radiation Protection Dosimetry*, 115:497–502, 2005. [cited at p. 14, 18]
- [56] Edward Castillo, Richard Castillo, Yin Zhang, and Thomas Guerrero. Compressible image registration for thoracic computed tomography images. *Journal of Medical and Biological Engineering*, 29:236–247, 2009. [cited at p. 14, 19, 32, 59, 96]
- [57] J.W. Suh, D. Scheinost, X. Qian, A.J. Sinusas, C.K. Breuer, and X. Papademetris. Serial nonrigid vascular registration using weighted normalized mutual information. In *IEEE International Symposium on Biomedical Imaging*, 2010. [cited at p. 14]
- [58] Tianming Liu, Dinggang Shen, and Christos Davatzikos. Deformable registration of cortical structures via hybrid volumetric and surface warping. *NeuroImage*, 22(4):1790 – 1801, 2004. [cited at p. 14, 49]
- [59] Han Jingfeng, Hornegger Joachim, Kuwert Torsten, Bautz Werner, and Romer Wolfgang. Feature constrained non-rigid image registration. In *18th Symposium on Simulationstechnique*, 2005. [cited at p. 14, 49]
- [60] Vladlena Gorbunova, Stanley Durrleman, Pechin Lo, Xavier Pennec, and Marleen de Bruijne. Lung CT registration combining intensity, curves and surfaces. In *IEEE International Symposium on Biomedical Imaging*, pages 340–343, 2010. [cited at p. 14, 48, 49]
- [61] D. Rueckert, L. I. Sonoda, C. Hayes, D. L. G. Hill, M. O. Leach, and D. J. Hawkes. Nonrigid registration using free-form deformations: Application to breast MR images. *IEEE Transactions on Medical Imaging*, 18:712–722, 1999. [cited at p. 14, 19, 48, 50]
- [62] G. Christensen, R. D. Rabitt, and M. I. Miller. Deformable templates using large deformation kinematics. *IEEE Transactions on Medical Imaging*, 5:1435–1447, 1996. [cited at p. 14, 48]

- [63] Morten Bro-Nielsen. *Medical Image Registration and Surgery Simulation*. PhD thesis, Technical University of Denmark, Department of Mathematical Modelling, 1996. [cited at p. 14]
- [64] C Briot. *Optimal Registration of Deformed Images*. PhD thesis, University of Pennsylvania, Philadelphia, 1981. [cited at p. 14]
- [65] Ruzena Bajcsy and Stanislav Kovacic. Multiresolution elastic matching. *Computer Vision, Graphics, and Image Processing*, 46(1):1–21, 1989. [cited at p. 14]
- [66] Berthold K. P. Horn and Brian G. Schunk. Determining optical flow. *Artificial Intelligence*, 17:185–203, 1981. [cited at p. 14]
- [67] Jesper Pedersen, Haseem Ashraf, Asger Dirksen, Karen Bach, Hanne Hansen, Phillip Toennesen, Hanne Thorsen, John Brodersen, Birgit Skov, Martin Døssing, Jann Mortensen, Klaus Richter, Paul Clementsen, and Niels Seersholm. The Danish randomized lung cancer CT screening trial - overall design and results of the prevalence round. *Journal of Thoracic Oncology*, 4:608–614, Apr 2009. [cited at p. 16, 26]
- [68] PA de Jong, Y Nakano, MH Lequin, R Woods, RD Pare, and Hawm Tiddens. Progressive damage on high-resolution computed tomography despite stable lung function in CF. *European Respiratory Journal*, 23:93–97, 2004. [cited at p. 16, 27]
- [69] ITK. *Insight Segmentation and Registration Toolkit*, <http://www.itk.org/>. [cited at p. 16, 76]
- [70] David Tschumperle. *CImg C++ Template Image Processing Toolkit*, <http://cimg.sourceforge.net/>. [cited at p. 16]
- [71] Stefan Klein and Marius Staring. *Elastix Toolkit*, <http://elastix.isi.uu.nl/index.php>. [cited at p. 16]
- [72] S. Klein, M. Staring, K. Murphy, M. A. Viergever, and J. P.W. Pluim. elastix: a toolbox for intensity-based medical image registration. *IEEE Transactions on Medical Imaging*, 29(1):196–205, 2010. [cited at p. 16]
- [73] Qianqian Fang. *A Matlab/Octave-based mesh generator*. <http://iso2mesh.sourceforge.net/cgi-bin/index.cgi>. [cited at p. 16, 39, 42, 54]
- [74] I. Sluimer, A. Schilham, M. Prokop, and B. van Ginneken. Computer analysis of computed tomography scans of the lung: A survey. *IEEE Transactions on Medical Imaging*, 25:385–405, 2006. [cited at p. 17, 74]

- [75] I.C. Sluimer, M. Prokop, and B. van Ginneken. Towards automated segmentation of the pathological lung in CT. *IEEE Transactions on Medical Imaging*, 24:1025–1038, 2005. [cited at p. 18]
- [76] Pan Li, Urban Malsch, and Rolf Bendl. Combination of intensity-based image registration with 3D simulation in radiation therapy. *Physics in Medicine and Biology*, 53:4621–4637, 2008. [cited at p. 18, 38, 48, 49]
- [77] Hidenori Ue, Hideaki Haneishi, Hideyuki Iwanaga, and Kazuyoshi Suga. Respiratory lung motion analysis using a nonlinear motion correction technique for respiratory-gated lung perfusion SPECT images. *Annals of Nuclear Medicine*, 21:175–183, 2007. [cited at p. 18]
- [78] Keelin Murphy, Bram van Ginneken, Eva M. van Rixkoort, B J de Hoop, M Prokop, P Lo, Marleen de Bruijne, and J P W Pluim. Obstructive pulmonary function: Patient classification using 3D registration of inspiration and expiration CT images. In *Second International Workshop on Pulmonary Image Analysis*, 2009. [cited at p. 18, 96]
- [79] D. L. Hill, P. G. Batchelor, M. Holden, and D. J. Hawkes. Medical image registration. *Physics in Medicine and Biology*, 46(3):R1–45, Mar 2001. [cited at p. 18]
- [80] A Pevsner, B Davis, S Joshi, A Hertanto, J Mechalakos, E Yorke, K Rosenzweig, S Nehmeh, YE Erdi, JL Humm, S Larson, CC Ling, and GS Mageras. Evaluation of an automated deformable image matching method for quantifying lung motion in respiration-correlated CT images. *Medical Physics*, 33:369–376, 2006. [cited at p. 18, 32]
- [81] David Sarrut, Vlad Boldea, Serge Miguët, and C Ginestet. Simulation of 4D-CT Images from Deformable Registration between Inhale and Exhale Breath-hold CT Scans. *Medical Physics*, 33(3):605–617, March 2006. [cited at p. 18, 19, 48]
- [82] S B Shaker, A Dirksen, L C Laursen, L T Skovgaard, and N H Holstein-Rathlou. Volume adjustment of lung density by computed tomography scans in patients with emphysema. *Acta Radiologica*, 4, 2004. [cited at p. 18, 74]
- [83] Brett Simon. Non-invasive imaging of regional lung function using X-ray computed tomography. *Journal of Clinical Monitoring and Computing*, 16:433–442, 2000. [cited at p. 18]
- [84] Lei Zhu, Yan Yang, Steven Haker, and Allen Tannenbaum. An image morphing technique based on optimal mass preserving mapping. *IEEE Transactions on Image Processing*, 16:1481–1495, 2007. [cited at p. 19]

- [85] Youbing Yin, Eric Hoffman, and Ching-Long Lin. Local tissue-weight-based nonrigid registration of lung images with application to regional ventilation. In J.P.W. Pluim and B.M. Dawant, editors, *SPIE (Medical Imaging)*, volume 7262 of *Proc. SPIE*, 2009. [cited at p. 19]
- [86] Vladlena Gorbunova, Pechin Lo, Martine Loeve, Harm Tiddens, Jon Sporring, Mads Nielsen, and Marleen de Bruijne. Mass preserving registration for lung CT. In J.P.W. Pluim and B.M. Dawant, editors, *SPIE (Medical Imaging)*, volume 7259 of *Proc. SPIE*, Feb 2009. [cited at p. 19]
- [87] Pechin Lo, J Sporring, H Ashraf, J.J.H Pedersen, and M de Bruijne. Vessel-guided airway segmentation based on voxel classification. In *First International Workshop on Pulmonary Image Analysis*, 2008. [cited at p. 20, 22, 23, 39, 40, 42, 54]
- [88] Daniel Rueckert, Paul Aljabar, Rolf A. Heckemann, Joseph V. Hajnal, and Alexander Hammers. Diffeomorphic registration using b-splines. In R. Larsen, M. Nielsen, and J. Sporring, editors, *Proc. Medical Image Computing and Computer Assisted Intervention (MICCAI)*, volume 2, pages 702–709, 2006. [cited at p. 20]
- [89] T Wang and A Basu. A note on a fully parallel 3D thinning algorithm and its applications. *Pattern Recognition Letters*, 28(4):501–506, 2007. [cited at p. 22, 40, 54]
- [90] H. J. Johnson and G. E. Christensen. Consistent landmark and intensity-based image registration. *IEEE Transactions on Medical Imaging*, 21:450–461, 2002. [cited at p. 38, 49]
- [91] Fred L. Bookstein. *Morphological tools for landmark data; geometry and biology*. Cambridge University press, 1991. [cited at p. 38]
- [92] S. C. Joshi and M. I Miller. Landmark matching via large deformation diffeomorphisms. *IEEE Transactions on Medical Imaging*, 9:1357–1370, 2000. [cited at p. 38, 41]
- [93] Marc Vaillant and Joan Glaunes. Surface matching via currents. *Information Processing in Medical Imaging, 19th International Conference*, 3565:381–392, 2005. [cited at p. 38, 39, 41, 48]
- [94] Joan Glaunès, Anqi Qiu, Michael I. Miller, and Laurent Younes. Large deformation diffeomorphic metric curve mapping. *International Journal of Computer Vision*, 80(3):317–336, 2008. [cited at p. 38, 39, 41, 48, 50]
- [95] Stanley Durrleman, Xavier Pennec, Alain Trounev, and Nicholas Ayache. Measuring brain variability via sulcal lines registration: a diffeomorphic

- approach. In *Proc. Medical Image Computing and Computer Assisted Intervention (MICCAI)*, volume 4791 of *LNCS*, pages 675–682, 2007. [cited at p. 38]
- [96] Stanley Durrleman, Xavier Pennec, Alain Trounev, and Nicholas Ayache. Sparse approximation of currents for statistics on curves and surfaces. In *Proc. Medical Image Computing and Computer Assisted Intervention (MICCAI)*, volume 5242 of *LNCS*, pages 390–398, 2008. [cited at p. 38]
- [97] Stanley Durrleman, Xavier Pennec, Alain Trounev, Paul Thompson, and Nicholas Ayache. Inferring brain variability from diffeomorphic deformations of currents: an integrative approach. *Medical Image Analysis*, 12(5):626–637, 2008. [cited at p. 38, 39, 41, 48, 50]
- [98] Stanley Durrleman and et al. Sparse approximation of currents for statistics on curves and surfaces. In *Proc. Medical Image Computing and Computer Assisted Intervention (MICCAI)*, volume 5242 of *LNCS*, pages 390–398, 2008. [cited at p. 38]
- [99] Mutsumi Tashiro, Shinichi Minohara, Tatsuaki Kanai, Ken Yusa, Hideyuki Sakurai, and Takashi Nakano. Three-dimensional velocity mapping of lung motion using vessel bifurcation pattern matching. *Medical Physics*, 33(6):1747–1757, Jun 2006. [cited at p. 48]
- [100] Pierre Hellier and Christian Barillot. Coupling dense and landmark-based approaches for non rigid registration. *IEEE Transactions on Medical Imaging*, 22:217–227, 2000. [cited at p. 48, 49]
- [101] Dinggang Shen and Christos Davatzikos. Hammer: Hierarchical attribute matching mechanism for elastic registration. *IEEE Transactions on Medical Imaging*, 21:1421–1439, 2002. [cited at p. 49]
- [102] Stephen R. Aylward, Julien Jomier, Sue Weeks, and Elizabeth Bullitt. Registration and analysis of vascular images. *International Journal of Computer Vision*, 55:123–138, 2004. [cited at p. 49]
- [103] Charles V. Stewart, Ying-Lin Lee, and Chia-Ling Tsai. An uncertainty-driven hybrid of intensity-based and feature-based registration with application to retinal and lung ct images. In Christian Barillot, David R. Haynor, and Pierre Hellier, editors, *Proc. Medical Image Computing and Computer Assisted Intervention (MICCAI)*, volume 3216 of *Lecture Notes in Computer Science*. Springer, 2004. [cited at p. 49]
- [104] K. Rohr, P. Cathier, and S. Wrz. Elastic registration of electrophoresis images using intensity information and point landmarks. *Pattern Recognition*, 37(5):1035 – 1048, 2004. [cited at p. 49]

- [105] Pascal Cachier, Jean-Francois Mangin, Xavier Pennec, Denis Rivière, Dimitri Papadopoulos-Orfanos, Jean Régis, and Nicholas Ayache. Multisubject Non-rigid Registration of Brain MRI Using Intensity and Geometric Features. In Wiro J. Niessen and Max A. Viergever, editors, *Proc. Medical Image Computing and Computer Assisted Intervention (MICCAI)*, volume 2208 of *Lecture Notes in Computer Science*, pages 734–742, 2001. [cited at p. 49]
- [106] D. Louis Collins, Georges Le Goualher, and Alan C. Evans. Non-linear cerebral registration with sulcal constraints. In *Proc. Medical Image Computing and Computer Assisted Intervention (MICCAI)*, pages 974–984, London, UK, 1998. Springer-Verlag. [cited at p. 49]
- [107] Kunlin Cao, Kai Ding, Gary E. Christensen, Madhavan L. Raghavan, Ryan E. Amelon, and Joseph M. Reinhardt. Unifying Vascular Information in Intensity-Based Nonrigid Lung CT Registration. In B. Fischer, B.M. Dawant, and C. Lorenz, editors, *Biomedical Image Registration: 4th International Workshop, LNCS*, pages 1–12, 2010. [cited at p. 49, 96, 97]
- [108] Pechin Lo, Jon Sparring, Haseem Ashraf, Jesper J.H. Pedersen, and Marleen de Bruijne. Vessel-guided airway tree segmentation: A voxel classification approach. *Medical Image Analysis*, 14(4):527 – 538, 2010. [cited at p. 54]
- [109] E.M. van Rikxoort, B. de Hoop, M.A. Viergever, M. Prokop, and B. van Ginneken. Automatic lung segmentation from thoracic computed tomography scans using a hybrid approach with error detection. *Medical Physics*, 36(7):2934–2947, 2009. [cited at p. 64, 96]
- [110] E.M. van Rikxoort, B. van Ginneken, M. Klik, and M. Prokop. Supervised enhancement filters: application to fissure detection in chest CT scans. *IEEE Transactions on Medical Imaging*, 27(1):1–10, 2008. [cited at p. 65]
- [111] Richard H. Byrd, Peihuang Lu, Jorge Nocedal, and Ciyou Zhu. A limited memory algorithm for bound constrained optimization. *SIAM Journal on Scientific Computing*, 16:1190–1208, 1994. [cited at p. 75]
- [112] GL Snider, J Kleinerman, WM Thurlbeck, and ZH Bengali. The definition of emphysema: report of a National Heart, Lung, and Blood Institute, division of lung diseases workshop. *American Review of Respiratory Disease*, 132:182–185, 1985. [cited at p. 81]
- [113] Lauge Sørensen, Pechin Lo, Haseem Ashraf, Jon Sparring, Mads Nielsen, and Marleen de Bruijne. Learning COPD sensitive filters in pulmonary CT. In *Proc. Medical Image Computing and Computer Assisted Intervention (MICCAI)*, pages 699–706, 2009. [cited at p. 82]

- [114] Jan J. Koenderink and Andrea J. Van Doorn. The structure of locally orderless images. *International Journal of Computer Vision*, 31(2-3):159–168, 1999. [cited at p. 83]
- [115] Bram van Ginneken and Bart M. ter Haar Romeny. Multi-scale texture classification from generalized locally orderless images. *Pattern Recognition*, 36(4):899–911, 2003. [cited at p. 83]
- [116] Kunlin Cao, Gary E. Christensen, Kai Ding, and Joseph M. Reinhardt. Intensity-and-Landmark-Driven, Inverse Consistent, B-Spline Registration and Analysis for Lung Imagery. In *Second International Workshop on Pulmonary Image Analysis*, pages 137–148, 2009. [cited at p. 96]